NANOSCALE GROWTH TWINS IN SPUTTERED COPPER FILMS

A Dissertation

by

OSMAN ANDEROGLU

Submitted to the Office of Graduate Studies of
Texas A&M University
in partial fulfillment of the requirements for the degree of

DOCTOR OF PHILOSOPHY

May 2010

Major Subject: Materials Science and Engineering

NANOSCALE GROWTH TWINS IN SPUTTERED COPPER FILMS

A Dissertation

by

OSMAN ANDEROGLU

Submitted to the Office of Graduate Studies of
Texas A&M University
in partial fulfillment of the requirements for the degree of

DOCTOR OF PHILOSOPHY

Approved by:

Chair of Committee,   Xinghang Zhang
Committee Members,   Ibrahim Karaman
                                       Haiyan Wang
                                       K. Ted Hartwig
Chair of Materials Science
and Engineering Faculty, Tahir Cagin

May 2010

Major Subject: Materials Science and Engineering

ABSTRACT

Nanoscale Growth Twins in Sputtered Copper Films. (May 2010)

Osman Anderoglu, B.S., Bogazici University;

M.S., Texas A&M University

Chair of Advisory Committee: Dr. Xinghang Zhang

The focus of this research is the development of high strength, high conductivity copper films. Pure copper is soft and traditional strengthening mechanisms cause substantial decrease in conductivity. To address the challenge, epitaxial nanotwinned copper films are synthesized on HF etched Si (110) substrates. These films show high hardness (~ 2.8 GPa) due to high density of coherent twin boundaries (CTBs) which effectively block the motion of dislocations similar to grain boundaries (GBs). Resistivity of CTBs is calculated to be an order of magnitude lower than that of GBs. Hence, conductivity of nanotwinned copper is still comparable to that of pure copper. In addition, it is shown that average twin spacing can be controlled by adjusting deposition rate. Analytical studies together with experimental evidence show that nanotwins can improve the strength-to-resistivity ratio significantly in copper.

In general, nanocrystalline metals suffer from low ductility. To study plastic deformation via rolling, thick polycrystalline nanotwinned copper foils are sputtered on SiO_2 and then peeled off the substrate. Despite the high strength, room temperature rolling experiments show that nanotwinned copper films exhibit stable plastic flow with

no shear localization or fracture even at thickness reduction of over 50%. Post-deformation studies of microstructure reveals that the plastic deformation is facilitated by the migration of CTBs normal to the twin boundary plane due to the glide of twinning dislocations in the twin plane. X-ray pole figure measurements show insignificant out of plane rotation as a result of 50% rolling thickness reduction.

Thermal stability of nanocrystalline metals is also a concern. Free standing nanotwinned polycrystalline copper films show remarkable thermal stability after annealing at 800 °C. The driving force for twin growth is much lower than that for grain coarsening because the energy stored in CTBs is an order of magnitude lower than that of GBs. As a result, the average twin spacing stays below 20 nm after annealing. Such high thermal stability of nanotwins leads to the retention of hardness of 2.2 GPa. Low energy twin boundary may provide a unique way to achieve both high strength and high temperature thermal stability in certain metallic materials.

ACKNOWLEDGEMENTS

My appreciation goes to my advisor, Dr. Xinghang Zhang, for his guidance, advice, support and encouragement during the past four years. He has a great personality and is one of the best scientists I have ever met. It has always been a pleasure to work with him. It is an honor to be one of his first PhD students. I am also grateful to Dr. Amit Misra for his support and guidance during my internship at Los Alamos National Laboratory. He is a brilliant scholar and wonderful mentor. I am looking forward to working with him as a postdoctoral research associate upon graduation. I would like to thank Professors Ibrahim Karaman, K. Ted Hartwig, Haiyan Wang, and Tahir Cagin for serving on my committee, offering me valuable advices on my research and on my future career.

I am very grateful to Dr. Richard G. Hoagland, Dr. Dave Embury, and Dr. John P. Hirth for useful discussions; Dr. Jian Wang, Dr. Michael J. Demkowicz, Dr. Nathan Mara, Dr. Greg Swadener, Dr. Filip Ronning, Dr. Michael F. Hundley, and Dr. Rob Dickerson for their collaboration, guidance, support and help at Los Alamos.

I sincerely thank Jan Gerston for always being friendly, helpful and supportive. My thanks also go to my friends, colleagues, department faculty and staff for making my time at Texas A&M University a great experience.

Finally, I would like to dedicate all of my work to my parents, my wife and my daughter. Without their love, faith and sacrifice, I would never have accomplished this work.

TABLE OF CONTENTS

LIST OF TABLES

LIST OF FIGURES

FIGURE   Page

FIGURE   Page

CHAPTER I

INTRODUCTION

Copper (Cu) is one of the oldest metals known to humanity together with Iron (Fe) and Gold (Au). It is not known when copper was first discovered, but earliest estimate is 9000 BC. It was mined on Cyprus and named after this small island located in the south of Turkey as Cyprium "metal of Cyprus" in the Roman era [1]. Bronze Age (2500 BC to 600 BC) named after an alloy of copper with mostly tin (today also with Aluminum and Silicon), alone is perhaps enough to explain copper's important role in civilization. On the divine side, there are verses in the Bible and Quran that refer to copper as well. Today, copper finds its way in almost every part of our daily lives; some being visible, some manufactured small enough to be beyond the resolution of human eye. Major uses of this precious metal can be divided into four categories [2]:

1- Building and construction: Wiring, plumbing, heating and architectural.

2- Infrastructure: Power-generating utilities, telecommunication.

3- Domestic and industrial equipment: Electronics, coinage.

4- Transport: Motor vehicles: Automobile, aircraft, railroad, marine.

In addition, copper is biostatic (bacteria will not grow on it) and used in biomedical applications. Figure 1 shows subdivision of the copper stock per capita in the U.S. for major categories of usage [2]. Furthermore copper is essential to plants and animals and is carried mostly in the bloodstream. On the production side, Chile is the top

---

This thesis follows the format of Journal of Applied Physics.

mine producer of copper with one-third world share followed by the USA, Indonesia and

Peru.
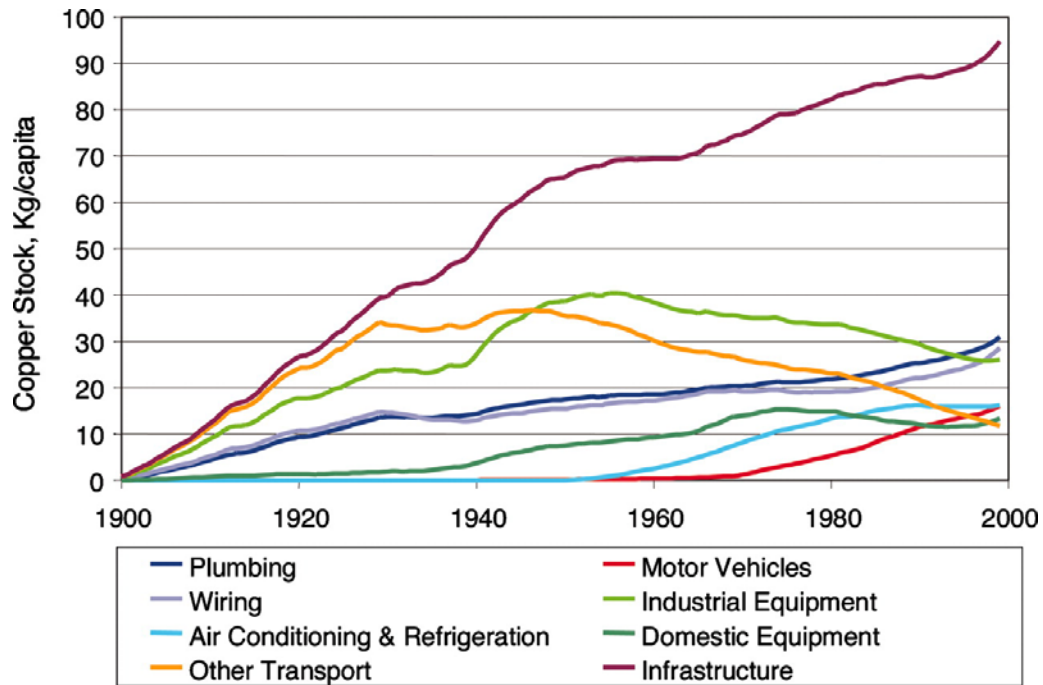
Fig. 1 Copper stock per capita for major categories of use in US [2].

What makes copper so important and widely used in diverse applications? The

rest of the report deals with some of its properties in detail but in short it is malleable,

ductile, and a good conductor of heat and electricity. Silver is the only other metal in

periodic table that has better electrical conductivity than copper. Among the four classes

mentioned above, application of copper in electronics is one of the motivations of the

current study. In microelectronics, copper thin films are replaced aluminum early 90s

and are used as electrical conductors. Figure 2 shows Scanning electron microscope

(SEM) image of IBM's six-level Copper interconnects technology in an integrated

circuit chip. A state-of-the-art microprocessor contains hundreds of millions of thin-film transistors that are interconnected by numerous interconnects. Failure of an interconnect could result in the failure of the entire chip's function. That chip could be in our cell phone or computer. Failure of one's computer or phone may not sound very important, however, that very same chip could be part of an ABS break system or a vital part of an airplane. In this case failure of the system can cause catastrophic consequences. Of course the chips are designed in a way to avoid catastrophic failures or extra safety measurements are taken, but the examples are enough to remind one the importance of copper in our daily life.

On the other hand, the increase in the use of copper brings some concerns. The amount of copper produced up to 1900 is only 2.5% of the copper produced in past millennia [2]. Now the important question is "Do we have unlimited source of copper?" Of course not, based on the current growth trend in the world population and the per-capita average of copper use for North America, the total world source would not be enough before year 2100 [2]. Employing better design, more efficient recycling and replacement with more abundant metals are some of the measures that can be taken. Design considerations together with the miniaturization of devices are two of the motivations of the topic that will be discussed in the next section.
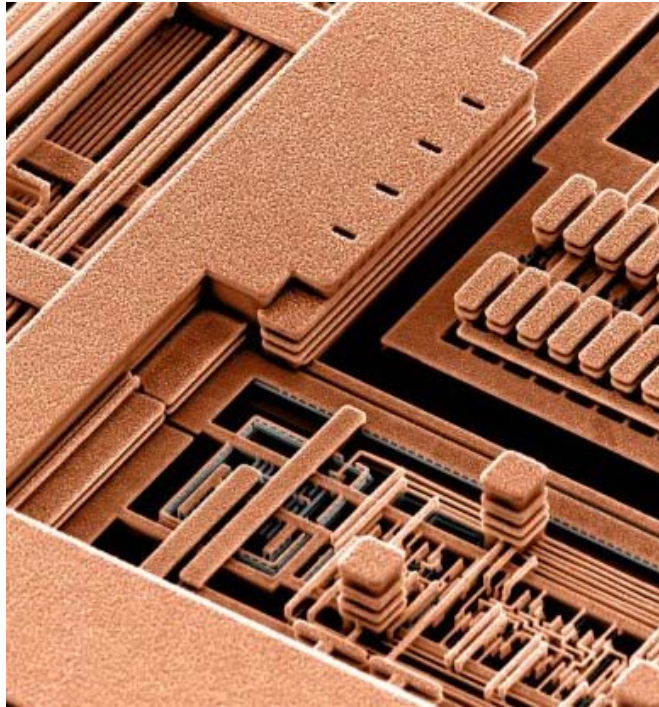
Fig. 2 SEM micrograph of six level copper interconnect in the CMOS 7S technology [3].

I.1. Thin film deposition techniques

Motivated by the need for small-scale devices, cost benefits, and properties achievable, thin film science has grown world-wide into a major research area in recent years. Thin films can simply be defined as layer of material with one dimension much smaller than the other two. One of the major applications of thin films is in microelectronics. However, there are growing applications in other areas like optical and magnetic devices (magnetic multilayers for data storage in hard discs), electrochemistry, protective and decorative coatings (wear resistant coatings for tools) and catalysis.

Sophisticated solid-state devices with continuously improved quality require a rapid evolution of thin film deposition technology. The Moore's law (a famous law in

semiconductor industry) predicts that the number of transistors in an integrated circuit doubles every two year since the invention of integrated circuit in 1958. This number is on the order of billions today. The number is self-explanatory of the precision, complexity and difficulty involved in the deposition techniques. The semiconductor industry is exclusively dependent on thin solid films of a variety of materials deposited from the gas, vapor, liquid, or solid phase, such dependence emphasizes the significance of deposition technology [4]. It is not the scope of this thesis to discuss all of the methods in detail. Interested readers are referred to literature [4, 5].

We now briefly introduce several of the most commonly used techniques for thin metal films, including physical vapor deposition (PVD), electrodeposition, and chemical vapor deposition (CVD). Furthermore, magnetron sputtering (a PVD technique) will be discussed in more details as it is the main technique that is used in this work.

I.1.1. Physical vapor deposition (PVD)

Sputtering and evaporation are the two most commonly used PVD techniques [5, 6]. Evaporation is a process in which the vapor is created by evaporating the source material using thermal energy. Target can be heated by several methods. Evaporated atoms travel a distance in a vacuum chamber before they condense on a substrate surface immersed in the vapor to form the solid film. Depending on the thermal energy source used, evaporation can be divided into several types, including thermal evaporation, electron-beam (e-beam) evaporation, and molecular beam epitaxy (MBE) [6]. During evaporation, atoms of the evaporated material arrive at substrate surface with low kinetic energy. The microstructure of the deposited film is affected by various parameters

including substrate temperature and orientation (higher substrate temperature provides additional kinetic energy for the target atoms), base pressure, power, deposition rate, etc. Different from evaporation, during sputtering the vapor of the source materials is formed through ionic impingement of a target.

Sputtering is an important PVD technique, when a solid surface is bombarded with energetic particles such as accelerated ions, surface atoms of the solid are scattered backward due to collisions between the surface atoms and the energetic particles. This phenomenon is called as back sputtering or just sputtering. Cathode sputtering is used for the deposition of thin films. Several sputtering systems are proposed for thin film deposition including dc diode, rf diode, magnetron, and ion beam sputtering. During sputter deposition, an evacuated chamber is filled with a sputtering gas (it is also possible to use a chimney around the gun so that one would avoid filling the entire chamber with gas), typically argon (Ar). Ar is chosen not only because it is inert but also because the necessary momentum transfer can be provided. The gas is ionized by imposing a direct-current (DC) or radio-frequency (RF) voltage, which forms a plasma in the chamber. An imposed electrical field accelerates the Ar_+ ions toward the target at high speed. The target atoms are dislodged when the energetic ions bombard the target surface. These atoms then travel through the gas phase and condense onto the substrate, forming the solid film.

Sputtering is a versatile technique that can be applied to many crystalline and amorphous materials. It offers better control in maintaining stoichiometry and more uniform film thickness. Alloy thin films with highly precise compositions and

multilayered films with individual layer thickness as thin as 1 nm can be fabricated through sputtering. The sputter technique also has some disadvantages. For instance, because the target atoms usually have a high kinetic energy when they arrive at the growth surface, the probability of defect nucleation (e.g. threading dislocations, stacking faults) and damage in sputtered films is generally higher than in evaporated films. The high energy target atoms also cause the substrate temperature to rise. Moreover, the sputtering gas may cause contamination by introducing impurity atoms in the films. However, it should also be mentioned that heating effect can be avoided through proper cooling and high vacuum can reduce the contamination. Metal films sputtered at room temperature are typically polycrystalline in nature, consisting of fine grains. Similar to evaporation, the microstructure is of course affected by many parameters such as substrate temperature, deposition rate, sputter power density, and working gas pressure etc. The technique used to produce copper films in this work is magnetron sputtering which will be discussed in greater detail in Chapter II "Experimental methods".

I.1.2. Electrodeposition

Electrodeposition (also called electroplating) is a process in which a metal is coated on a conductive surface through electrochemical reactions that are facilitated by an applied electrical potential. In this process, the surface to be coated is immersed into a solution of metal salts. The surface needs to be conductive and forms the cathode of the electrical circuit. With an electrical current passing through the solution, the positive ions of the source metal are attracted to the cathode surface, where they are reduced,

resulting in a coating of the source metal on that surface. A simple schematic is shown in Figure 3.

Electroplating is a simple and economical way to deposit uniform coatings. It has been used in many applications in the industry. Some examples are copper conductor lines in printed circuit boards, chromium coatings on steel parts in automobiles, zinc coatings on galvanized steel, and decorative gold and silver coatings on jewelry and various consumer products. Electrodeposition is also introduced for growing copper films in integrated circuits and has the advantages of simplicity, safety, low cost, low deposition temperature, low resistivity (due to larger grain size), and high gap filling capacity in a dual-damascene process. Since a high-conductivity surface is required for the electrodeposition, a seed Cu layer is usually sputter deposited immediately prior to the plating process [7].

There are also some limitations for electrodeposition. For example, it generally cannot be applied to deposit alloys and nonmetallic materials. Due to the exposure of the film growth surface to the solution, impurities may be introduced.

I.1.3. Chemical vapor deposition (CVD)

CVD is a chemical process used to produce high-purity, high-performance thin films and often used in the semiconductor industry. CVD is a chemical process used to produce high-purity, high-performance thin films and often used in the semiconductor industry. In a typical CVD process, substrate is exposed to one or more volatile precursors, which react and/or decompose on the substrate surface to produce the desired
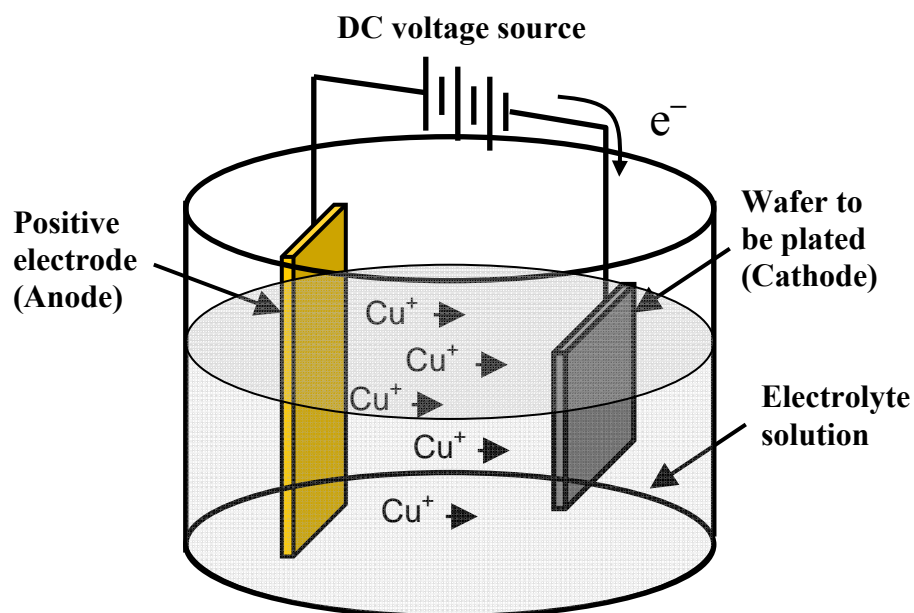
Fig. 3 Schematic description of electrodeposition. In the solution, copper is oxidized at the anode to Cu^{2+} by losing two electrons. At the cathode, the Cu^{2+} is reduced to metallic copper by gaining two electrons. The result is the effective transfer of copper from the anode source to a plate covering the cathode.

deposit. There are several types of CVD processes. These processes can be classified according to operating pressure, physical characteristics of vapor, plasma methods and other methods including atomic layer CVD (ALCVD), metalorganic CVD (MOCVD), rapid thermal CVD (RTCVD), etc. Hybrid physical-chemical vapor deposition (HPCVD) that involves both chemical decomposition of precursor gas and vaporization of solid a source can also be categorized in this group.

Deposition rate is limited by two factors in CVD. If the reaction rate exceeds the gas delivery rate than this is called mass-transport limited deposition (at high temperature). In this case film growth rate is insensitive to temperature and controlled by gas delivery. If the reaction rate is less than gas delivery rate, than this is a reaction limited deposition (low temperature or high vacuum). In this case, temperature controls the deposition rate and film uniformity.

Table 1 shows a comparison of different deposition techniques. The techniques show quite a bit difference from one to other. That gives researchers an opportunity to choose the most suitable technique for the required outcome. The last column shows the cost of the different techniques. This suggests that there is a trade-off between the outcome and the cost. For instance, defect free films with excellent surface can be deposited using MBE. However the cost limits the use of this technique. In addition, compared to other techniques MBE very slow and is used for very thin films. In contrast, electro plating can grow several inches thick film within minutes. However, obtaining a uniform thickness with electroplating is challenging.

Table 1. Comparison of several parameters involved in typical thin film deposition techniques.

Process	Material	Uniformity	Impurity	Grain size (nm)	Density	Deposition rate (Å/sec)	Substrate temp (°C)	Cost
Thermal Evaporation	low melting point materials, e.g. metals	poor	high	10~100	poor	1~20	50~100	very low
E-beam Evaporation	metals, ceramics, etc.	poor	low	10~100	poor	10~1000	50~100	high
Sputtering	mostly metals, dielectrics	very good	low	10~100	good	metal: 100 dielectric: 10	100	high
PECVD	mainly dielectrics	good	very low	10~100	good	10~100	200~300	very high
LPCVD	mainly dielectrics	very good	very low	1~10	excellent	10~100	600~1200	very high
MBE	Metals, dielectrics	excellent	very low	-	excellent	0.1-1	50~100	very high
Electroplating	Metals	good	low	~1000	excellent	>10000	-	very low

I.2. Fabrication of copper thin films

Microstructure of copper thin films, including grain size and its distribution, density, crystallographic texture and epitaxy, depends on kinetic parameters such as surface, interface, grain boundary, and bulk diffusivity. These kinetic parameters can be altered by controlling deposition processes such as deposition method, substrate, film thickness, and annealing. The microstructure of copper thin films deposited by PVD methods depend mainly on the deposition temperature, rate, vacuum and substrate/seed layers. Similar controls exist for films formed by CVD and plating processes [8].

In physical vapor deposition, atoms in vapor phase come in contact with the substrate and form chemical bonds. These atoms are called adatoms. Some adatoms can go back to vapor phase (evaporation) if they have enough energy to break the bonds formed on the surface (in addition to its own kinetic energy, substrate temperature can also help break the bonds). For film growth, condensation of atoms must exceed evaporation of adatoms from the substrate. If the temperature of the substrate is low or diffusion barrier is high, then adatoms cannot diffuse on the surface to a thermodynamically stable site. This results in an amorphous or very fine grained polycrystalline structure. For growth of crystalline structure, energy of adatoms must be larger than the diffusion barrier so that they can travel to equilibrium sites in the lattice [6]. When the adatoms are mobile enough on the surface and they condense on the equilibrium sites, more adatoms follow. Adatoms bond to substrate and each other. The energy difference of these two kinds of bonds affects the growth mode. When the adatoms are more strongly bound to each other than to the substrate, then small clusters

are nucleated directly on the substrate surface and then grow into islands of the condensed phase which is known as Volmer-Weber (VW) or island growth mode. Many metals on insulators, including many metals on alkali halides, graphite and other layer compounds such as mica grow by island mode [9].

If the atoms are more strongly bound to the substrate than to each other, the first atoms to condense form a complete monolayer on the surface, which becomes covered with a somewhat less tightly bound second layer. This growth mode is known as Frank-van der Merwe (FM) or layer mode and is observed in the case of adsorbed gases, such as several rare gases on graphite and on several metals, in some metal-metal systems, and in semiconductor growth on semiconductors [9].
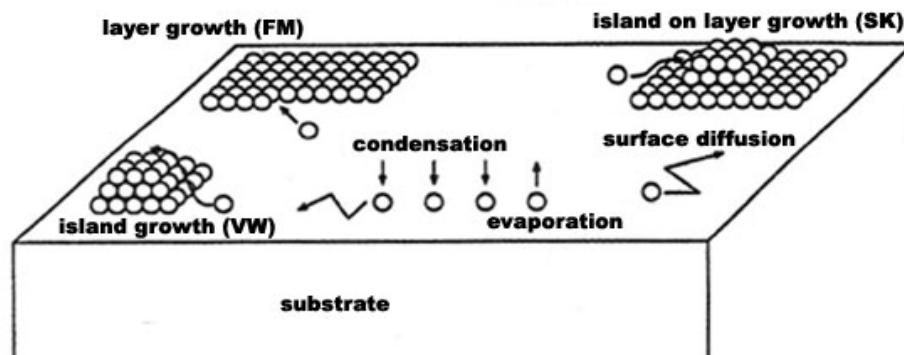
Fig. 4 Schematic showing film growth on a substrate [6].

The third growth mode, island on layer or Stranski-Krastanov (SK) is an intermediate case. After forming the first monolayer, subsequent layer growth in layer mode is unfavorable and islands are formed. This transition occurs at a critical layer

thickness which is highly dependent on the chemical and physical properties, such as surface energies and lattice parameters, of the substrate and film. For example, because of the lattice parameter, symmetry, or molecular orientation, the intermediate layer may not be able to be continued into the bulk crystal of the deposited material. This results in a high free energy of the deposited intermediate layer interface which favors subsequent island formation. There are now many examples of its occurrence in metal-metal, metal-semiconductor, gas-metal and gas-layer compound systems [9]. Figure 4 displays schematic of all three film growth modes.

I.2.1. Polycrystalline copper thin films

During film formation as discussed above, nuclei form on the substrate surface isolated from each other. The important factors that are controlling the structure of the film are deposition rate and ratio of substrate temperature to the melting point of the deposited material. Deposition rate directly affects the number of nuclei forming on the surface. The higher the deposition rate, the higher the number of nuclei on the substrate surface. On the other hand substrate temperature affects the random diffusion of adatoms on the surface. Adatoms will diffuse more at higher substrate temperatures because of extra energy provided from the surface. This will increase the number of encounters of the adatoms during diffusion. It is important to realize that for instance at room temperature between two materials (e.g. Cu and Al) the one with lower melting temperature (Al) will diffuse more than the one with higher melting temperature (Cu) if every other variable is kept the same.
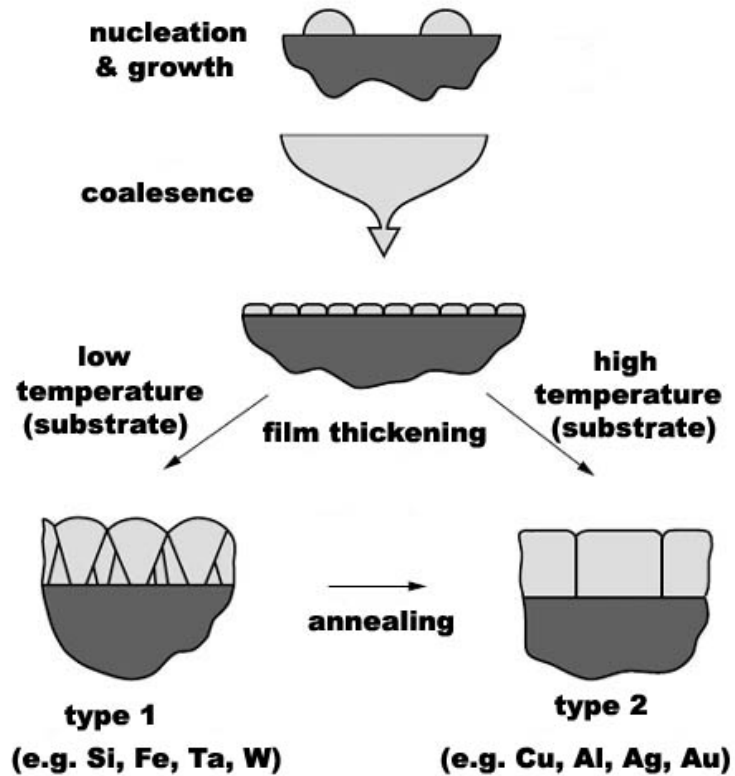
Fig. 5 Schematic showing stages of polycrystalline film formation on a substrate. Film growth and grain structure depends on surface mobility, deposition rate, and substrate temperature relative to melting temperature of deposited film [10].

At high deposition rates and moderate substrate temperatures, island growth (VW) mechanism dominates the film growth. Islands of atoms agglomerate into clusters, and the clusters grow until they impinge on each other to form continuous film on the substrate. When the crystalline clusters encounter each other they form grain boundary if they do not have sufficient mobility to align themselves or if there is not enough thermodynamic driving force to eliminate grain boundary [6]. This is the case for growth of metal films on semiconductor substrates, such as copper on silicon. This nucleation,

growth, impingement, and coalescence processes are schematically illustrated in Figures 5 and 6 [6, 10].
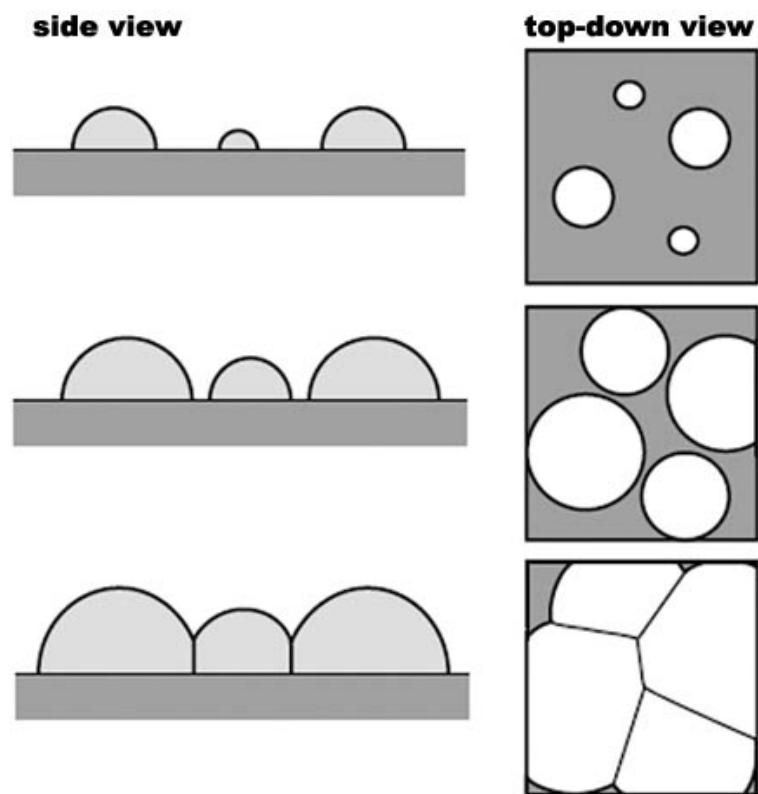
Fig. 6 Coalescence of island form continuous film on the substrate [10].

As more atoms arrive at the substrate, film thickness increases on top of the nuclei formed and therefore columnar grain structures develop. The size of the columnar grains is usually as big as the thickness of the film. This grain size along out-of-plane direction is usually larger compared to in-plane size. On the other hand, if the grain boundaries are mobile, grain structure evolves during film growth. This results in more equiaxed grain size where in-plane grain size is similar to thickness of the film.
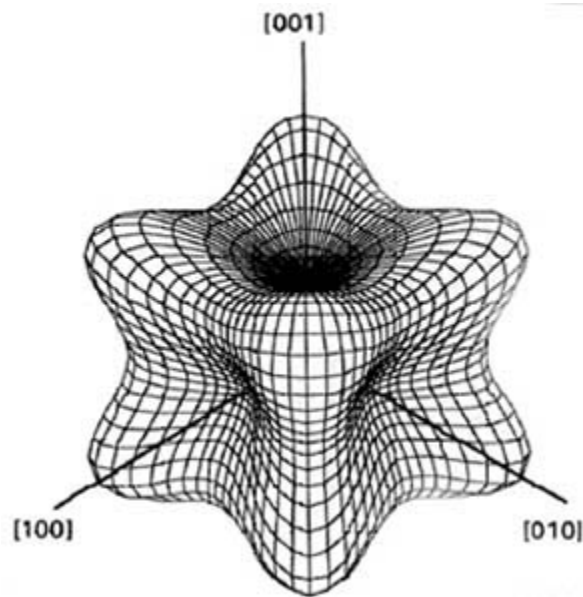
Fig. 7 Crystallographic orientation dependence of elastic modulus of copper [11].

Grains in polycrystalline films are usually not randomly distributed, but have some preferred crystallographic orientation, also called texture. (111) out-of-plane (perpendicular to substrate) fiber texture is quite common in copper thin films deposited on amorphous substrates. The grains are usually randomly oriented in the plane. The texture of thin films is affected by all the processes that affect grain size, and is also strongly affected by processing techniques and conditions. The grain orientation distribution evolves and can be controlled during film formation and subsequent processing. Since copper is highly anisotropic, variations are observed in properties. Figure 7 shows crystallographic orientation dependence of copper [11]. Elastic modulus of copper in <111> direction is ~ 3 times that of the one in <100> direction. Likewise, oxide and silicide formation are faster along (100) planes. From thermodynamics point

of view, it is the surface energy minimization that favors the (111) fiber texture formation in copper (fcc metals in general). The free surface energy density of the film, as well as the energy density of the interface between the film and the substrate are minimized when the grains are oriented in (111) direction [6]. On the other hand (100) texture is favored because of strain energy minimization [10].

Since copper is extensively used in microelectronics there is extensive research on polycrystalline copper films. Tracy and Knorr deposited polycrystalline copper films using a variety of deposition techniques, including sputtering, ionized beam deposition (IBD), evaporation, CVD and electro plating and different substrates analyzed about 35 different films, and reported the microstructure, texture, grain size, and distribution [12, 13]. They observed (111) and (200) texture, and random orientations in Cu, however (111) is the most common direction. In some cases they also observed bimodal grain distribution. Copper is also grown on buffer layer to increase adhesion, or to prevent interdiffusion. There is also literature work on copper film grown on different buffer layers including TiN, Ti, W, Ta, TaN [12-14]. Although electrodepositon results in large, randomly oriented grains, using buffer layers (Ti) it is possible to grow certain textures [14]. For the sake of longevity and simplicity of the table, the literature on microstructure of copper films is briefly summarized in Table 2. A wide variety of deposition conditions, substrate, temperature, and film thicknesses are provided in the table. In spite of a wide variety of deposition conditions and lack of some details in the deposition, some trends can still be identified for PVD films and are summarized in Figure 8 and 9.

Table 2. Effect of deposition conditions on the formation of texture in copper films [12, 13, 15].

Dep. technique	Dep. rate (nm/sec)	Substrate	Texture	Grain size (μm)	Thick (μm)	T (ºC)
Evaporat.						
Mag. sputt	1.5	SiO_2	random	0.4	0.5	
Mag. sputt	7	SiO_2	(111)		0.5	
Mag sputt	7	Ta	(111)	0.3	0.5	
Mag sputt	7	TaN	random	0.3	0.5	
IBD			(111)		2	
IBD			random		0.3	
IBD					0.3	
IBD					0.3	
IBD					0.3	
CVD			(111)		2	
Electrop.			random	>1	4	
Mag. sputt	0.5-10	SiO_2	(111)	0.04-0.12	1.5	RT
Mag sputt		SiO2	(111)		150	RT
Mag sputt	1	SiO2	(111)	0.04	30	RT
E-beam	10	SiO2	(111)		1.5	
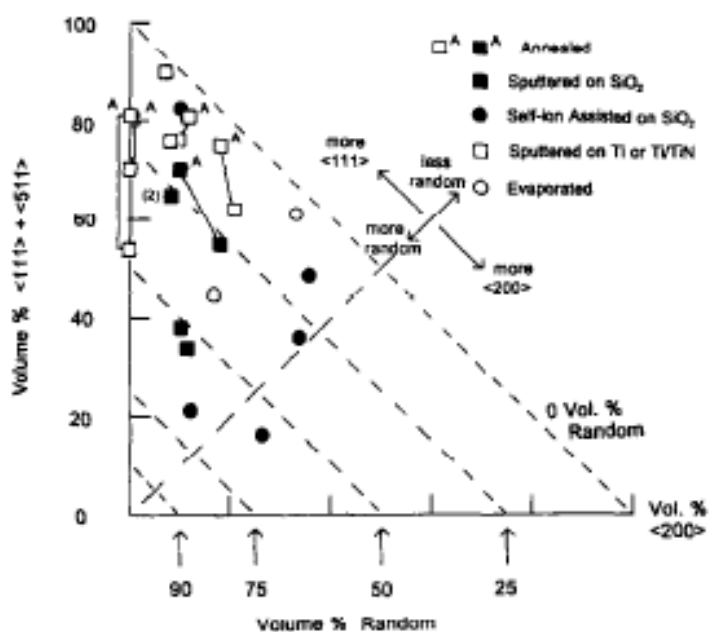
Fig. 8 Distribution of texture components in copper films deposited by various techniques [12].
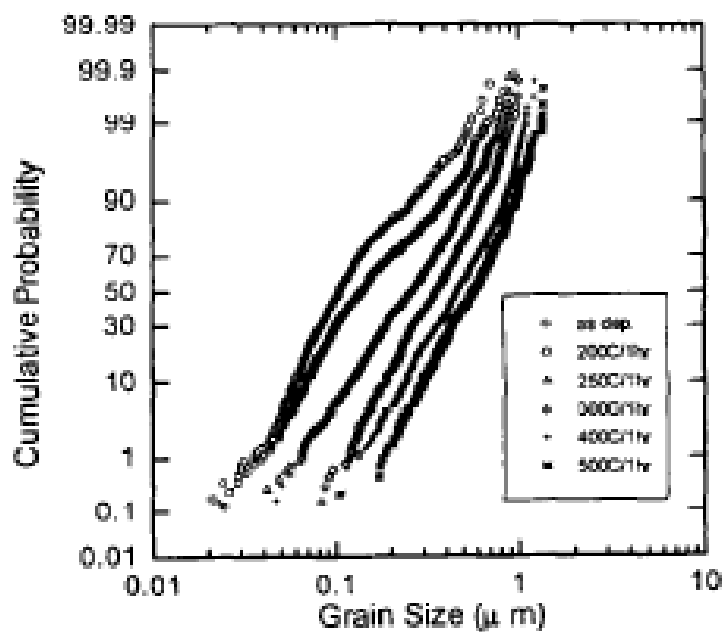
Fig. 9 Cumulative probability plot of grain size for 1 h isochronal anneals of 0.5 um copper sputtered on SiO$_2$ [12].

I.2.2. Epitaxial copper films

Epitaxy is the growth of films on a crystalline substrate where atoms of the deposited film align themselves to mimic the arrangements of the substrate atoms. Figure 10 shows a schematic and cross-sectional TEM image of epitaxial copper. If the depositing film and substrate are the same material then it is called homoepitaxy. One of the first steps in transistor fabrication in microelectronics is epitaxial growth of Si film, by CVD, on Si substrate. Heteroepitaxy is the case if the deposited film and substrate are different materials. Optoelectronic devices such as light-emitting diodes (LEDs) and lasers utilizing compound semiconductors, are based on heteroepitaxial film structures. Epitaxy of copper on silicon is also an example of this type. Some of the applications of epitaxial film growth can be listed as:

- preparation of semiconductor thin layers with dopant concentrations beyond equilibrium,

- growth of buffer layers on single crystalline substrates for improving heteroepitaxy and for preventing interdiffusion,

- low-temperature epitaxy for high performance electronic and optoelectronic devices,

- growth of silicide layers for electrical contacts and Schottky barriers in Si-based devices.

The epitaxial growth process depends on the coherency of the substrate-film interface. If the interface is incoherent, then film is free to adopt any in-plane lattice constant that minimizes its energy. However, if the interface is coherent then film is

restricted, and minimizes its energy by mimicking in-plane lattice constant of the substrate. The resulting elastic strain energy increases overall strain energy. As will be discussed later, epitaxy of copper film on silicon substrate is an example of this kind of interface. In addition to lattice constant mismatch, crystallographic orientation of the substrate and surface reconstruction are important parameters in determining the epitaxial growth of the film [5, 6].
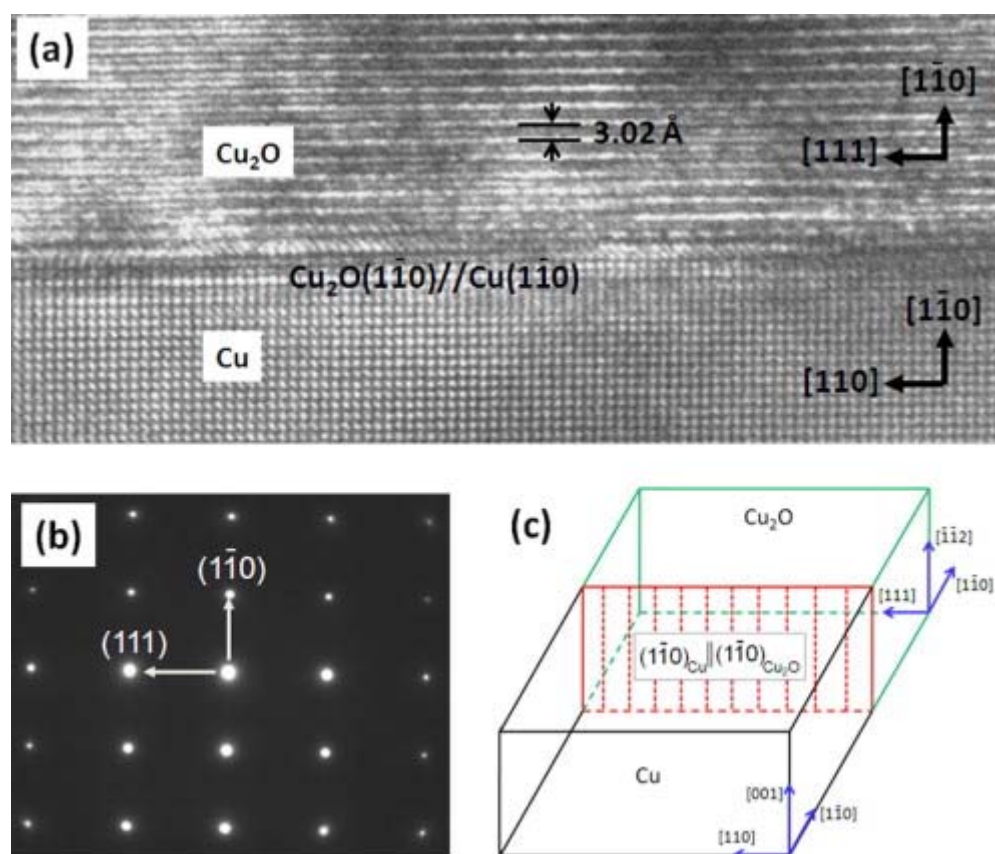
Fig. 10 (a) HRTEM image showing an edge-on Cu_2O–Cu interface, where the orientation relationship of the Cu_2O and Cu lattices is not cube-on-cube. **(b)** SAD pattern from the Cu_2O region in (a); **(c)** Schematic 3D representation of the interface geometry [16].

An important concept that characterizes epitaxy is fractional mismatch at the substrate-film interface, f, which is defined as:

$$f = 2 \times \frac{(a_S - a_F)}{(a_S - a_F)} \tag{1}$$

where a_S and a_F are lattice parameters of substrate and film respectively. A positive value of f implies that the initial layers of the epitaxial film will be stretched in tension while the substrate is compressed. Likewise, a negative f means film compression and tension in substrate [5]. If f is smaller than a few percent (<10%), epitaxial growth is possible. The coherency, strain and defects at the interface are results of this fractional mismatch. Lattice mismatch between substrate and film also determines the growth mode. If the mismatch is below 0.5%, then the growth mode is planar. For larger lattice mismatch the deposited film forms islands on the substrate however remains epitaxial [6].

Epitaxial growth is especially important in microelectronic applications. Elimination of grain boundaries improves electrical conductivity of copper thin films. Epitaxial growth of copper films on silicon substrate will be discussed in detail in Chapter V. Owing to its importance in microelectronics there is extensive research on production of epitaxial copper films. The information is tabulated in Table 3.

It is known that copper can be grown epitaxially on certain substrates such as silicon that are important in semiconductor industry. However, copper-silicon binary phase diagram in Figure 11 shows that the system forms intermetallics when the temperature is increased. Since the electrical conductivity will be reduced by the

formation of intermetallics, a buffer layer which will prevent the inter-diffusion is needed. Table 3 also lists some literature information on the buffer layers used for epitaxial film growth.
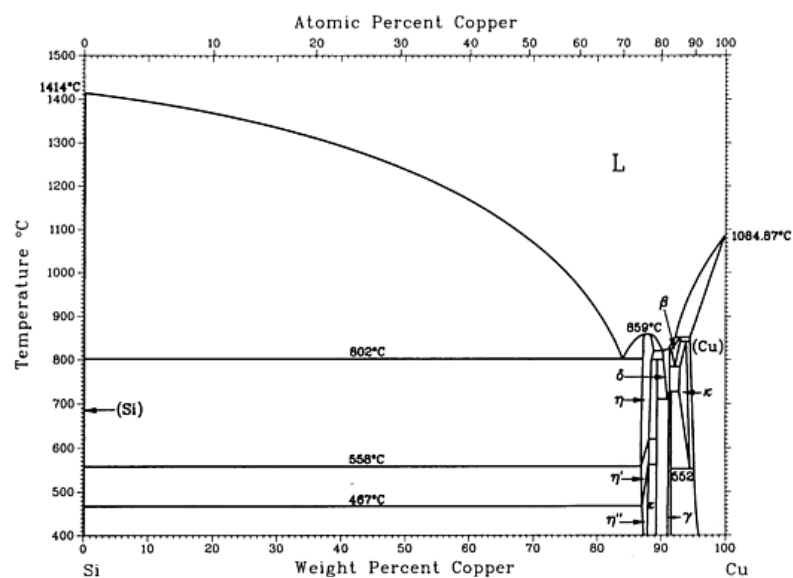
Fig. 11 Copper-silicon binary phase diagram [17].

Table 3. Epitaxial copper growth using various techniques and substrates [18-22].

Deposition technique	Deposition rate (Å/sec)	T (C)	Substrate	Etching/ Cleaning	Vacuum (Torr)	Orientation
Evaporation		425	Mica		2 × E-6	(100)
Evaporation	7	300	NaCl		2 × E-7	(100)
Evaporation	2-20	200-630	c-Sapphire		5 × E-6	(111)
Magnetron Sputt	4-9	RT	Si(110) (111)	10% HF	1 × E-7	(111)
Magnetron Sputt	5-50	RT	Si(100)	10% HF	1 × E-7	(100)
Magnetron Sputt	5-50	RT	Si(110)	50% HF	1 × E-7	(111)

I.3. Mechanical properties

Copper is among one of the most studied metals due to its numerous applications. In the literature there is extensive research and reports on the mechanical behavior of copper. In this section there is brief information on nanocrystalline copper in bulk form and copper thin films.

I.3.1. Mechanical properties of nanocrystalline and ultrafine grained bulk copper

Nanocrystalline (nc) and ultrafine grained (ufg) materials are structurally characterized by a large volume fraction of grain boundaries. Generally, nanocrystalline represents the class of materials with grain sizes less than 100 nm. Beyond this regime ufg term is used up to a few hundreds of nanometers. Existence of abundant grain boundaries significantly alters their mechanical, electrical and chemical properties compared to conventional coarse-grained polycrystalline materials.
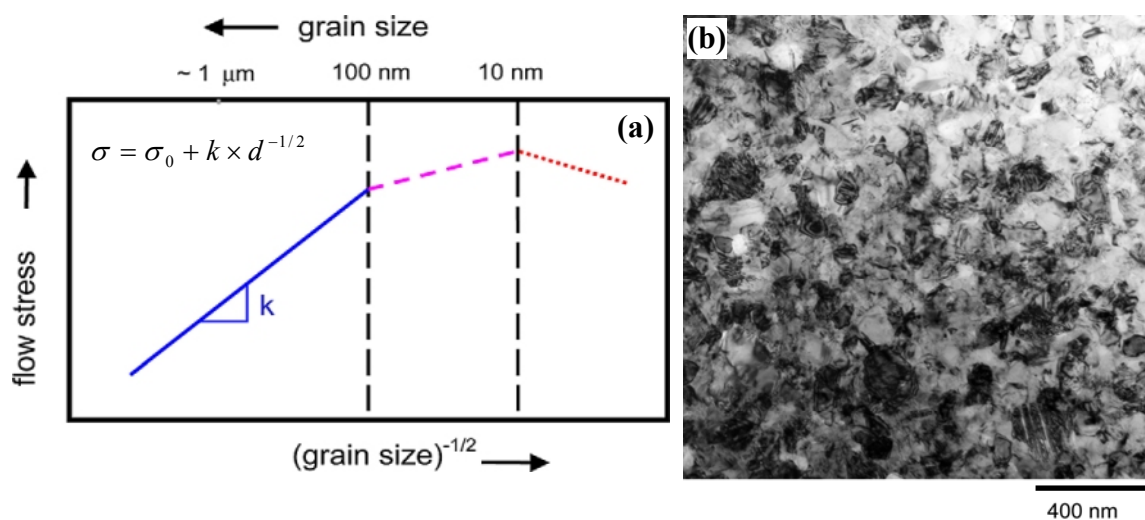
Fig. 12 (a) Grain size dependence of flow stress in metals **(b)** TEM image of ECAP processed nc copper shows an average grain size <100nm [23, 24].

There are several methods to synthesize nc and ufg materials. Inert gas condensation, severe plastic deformation, electroplating, mechanical alloying, ball milling, crystallization from amorphous phase, etc are widely used methods of nc and ufg material production. Grain refinement results in increased strength/hardness and improved toughness. On the other hand nc and ufc metals suffers from reduced ductility and in some cases porosity. There are several studies dealing with improving the ductility [25]. Figure 12 shows effect of grain size on the flow strength of a typical metal. In metals, plasticity is controlled by the motion of dislocations. Grain boundaries are obstacles to motion of dislocations. Grain refinement increases the density of grain boundaries. When the grain size is large, many dislocations can be accumulated in a grain which causes pile ups at the grain boundaries. Decreasing grain size decreases the amount of possible pile up at the boundary. Therefore, magnitude of applied stress necessary to move a dislocation across a grain boundary increases as the number of dislocations in a pile up decreases. Yield strength (σ) is proportional to amount of stress needed to move a dislocation across the grain boundary. Hence, there is an inverse relationship between grain size and yield strength, a mechanism known as Hall-Petch [26]:

$$\sigma = \sigma_0 + k \times d^{-1/2} \tag{2}$$

where σ_0 is lattice friction, k is a constant, and d is average grain size.
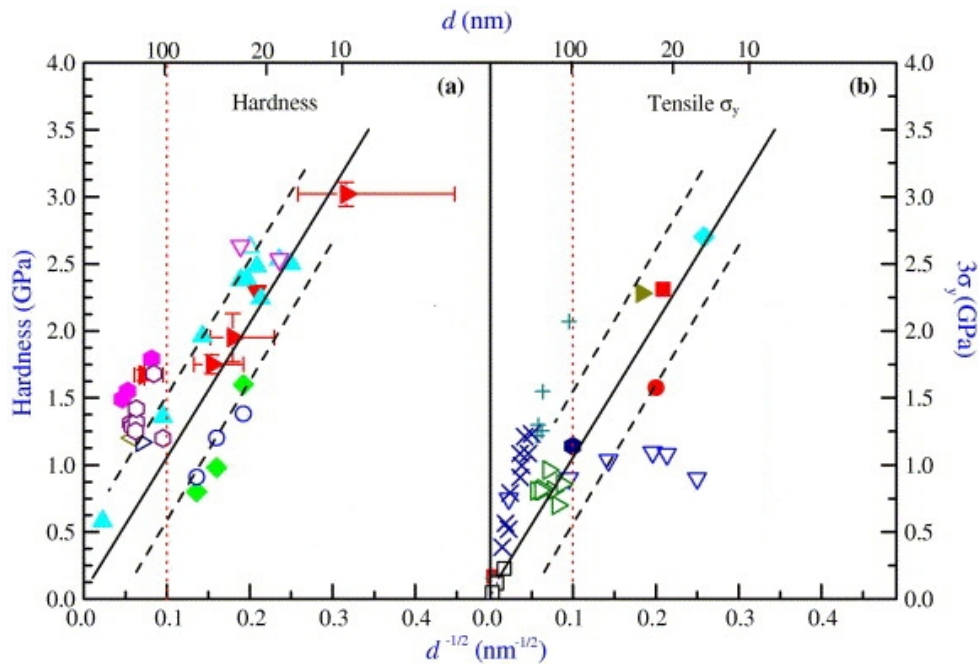
Fig. 13 (a) Dependence of hardness on grain size for various Cu samples. Literature data on hardness (solid symbols) and yield strength (open symbols-multiplied by 3) are also included. **(b)** Variation of tensile yield strength with grain size for various Cu samples. The straight lines represent the H–P relation extrapolated from the coarse grained Cu [27].

Figure 13 shows several experimental data on copper. Some data shows deviation from Hall-Petch type of behavior as the grain size approaches critical values whereas some data shows saturation. As the average grain size is refined from the ufg regime into the nc regime, strengthening slows down and finally breaks down as shown in Figures 12 (a), and 14 (b). The reason is dislocation pile is no longer possible because of the size of the grains. At this scale, plasticity is no longer controlled by dislocation motion, but is controlled by other mechanisms such as grain boundary sliding. Molecular dynamic simulations on nc copper showed that the critical grain size is around 10 nm, below which nc copper becomes softer [28, 29]. Interested readers are

encouraged to refer to literature for further reading on ufg and nc copper and other materials [23, 30, 31].
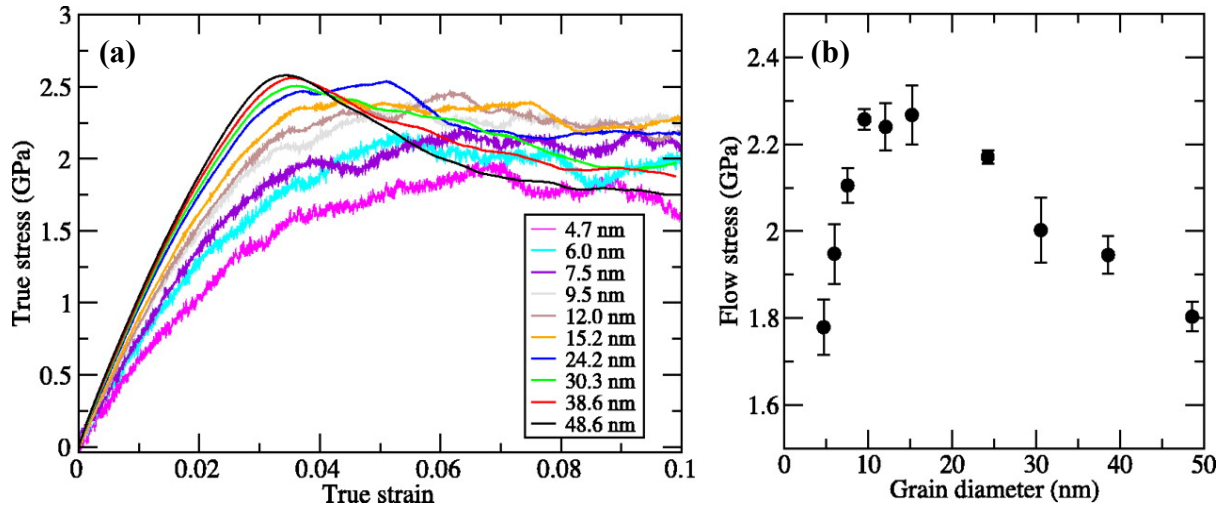
Fig. 14 (a) Stress-strain curves of copper with different grain sizes. (**b**) A maximum in the flow stress is seen for grain sizes of 10 to 15 nm, caused by a shift from grain boundary–mediated to dislocation-mediated plasticity [28].

I.3.2. Mechanical properties of copper thin films

The mechanical properties of thin films are different from bulk materials because of large interface, microstructure, and the constraints caused by the substrate. In addition, due to size constraints and presence of a substrate, traditional bulk testing methods are generally not applicable to thin films. Instead, new methods such as nanoindentation, microcompression, bulge testing, and substrate curvature measurement are developed to test thin film material properties. For instance, although uncertainties exist, it is possible to measure properties such as elastic modulus, yield strength, strain

hardening and internal stresses as well as deformation mechanisms in thin films using

nanoindentation [32].
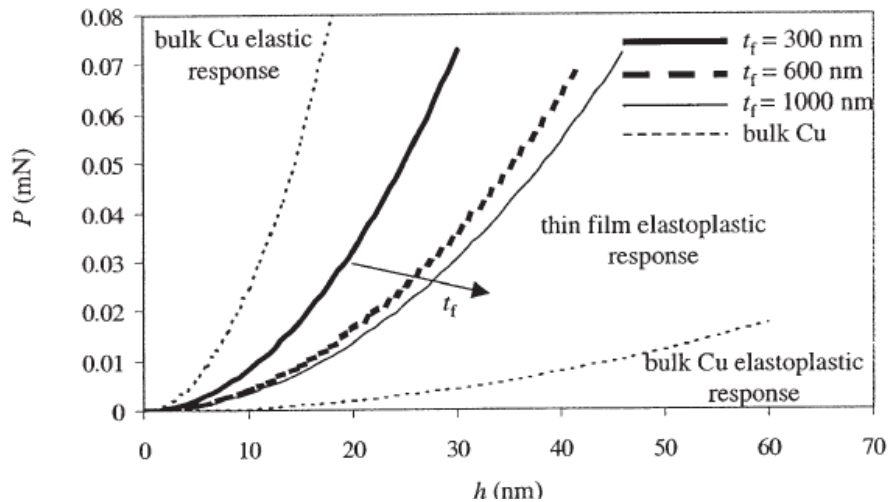
Fig. 15 Relative variations in the resistance to indentation, which signifies the resistance to elastoplastic deformation, as a function of film thickness for the Cu films [32].

Nanoindentation experiments on polycrystalline copper thin films with 300, 600

and 1000 nm in thickness, on silicon substrates showed that the overall elastoplastic

response of the film to nanoindentation is sensitive to the film thickness in that the

resistance to nano-indentation systematically decreases with increasing film thickness

(Figure 15). This is consistent with curvature measurements on film–substrate systems

which reveal that the 'average' yield strength of the thin film increases with decreasing

film thickness [32].
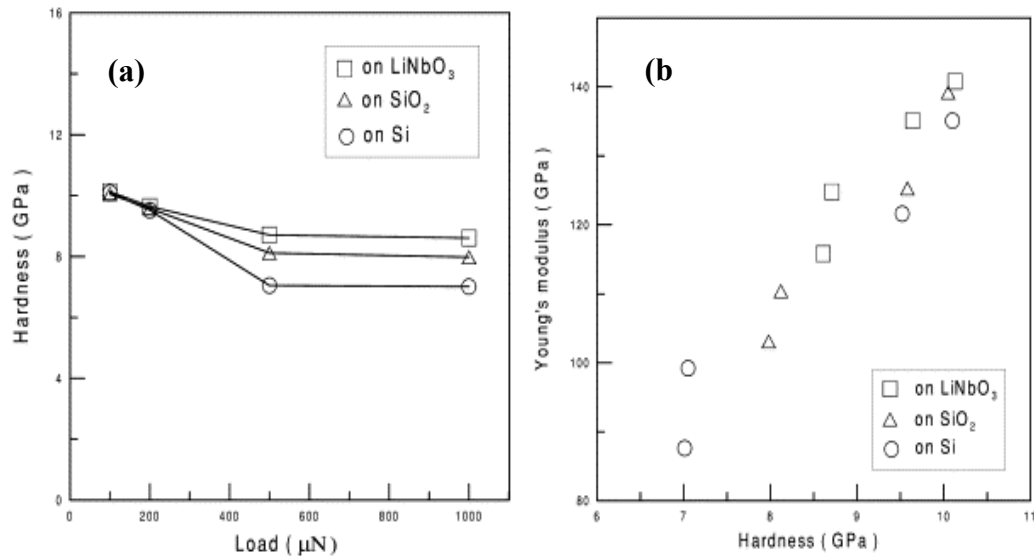
Fig. 16 (a) Hardness of Cu films on different substrates. **(b)** Relationship between hardness and Young's modulus of Cu films on different substrates [33].

In section I.2.1 the crystallographic orientation dependence of some material properties is discussed briefly. Vinci et al. studied the stress in (111) and (100) textured Cu thin films with several thicknesses. Stresses at room temperature are orientation dependent, with the (111) grains supporting a higher stress, as predicted by the dislocation glide models. However, although the (111) grains showed thickness dependence, the room temperature flow stress of the (100) grains appeared to be invariant with film thickness which is not well understood [34]. Fang and Chang used nanoindentation technique to measure the hardness and Young's modulus of copper thin films with substrates of Si, SiO_2 and $LiNbO_3$. They reported that the hardness values of ion beam sputtered copper films on different substrates at first decrease with increasing

load and then reach a plateau. The hardness of the film on Si is the lowest and that on LiNbO$_3$ is the highest (Fig 16a) and the Young's modulus of copper films increases with increasing hardness; the modulus of Cu film on LiNbO$_3$ is the highest and that of the film on Si is the lowest under the same hardness (Fig 16b) [33]. Read et al. carried microtension test on 2.6 micron electrodeposited copper films. They found somewhat lower modulus values which was attributed to grain boundaries which was proposed by Huang and Spaepen [35]. It was proposed that anelastic deformation at grain boundaries may occur in thin film specimens with very small grains, and this extra deformation, insignificant in bulk materials and not present in the single crystals, reduces the Young's modulus observed in microtensile tests [36, 37]. Keller et al. studied the tensile deformation and fracture behavior of freestanding electron beam evaporated Cu thin films using microtensile and in-situ straining tests. The Cu films exhibited very low ductility (1% <), which was attributed to both fine grain size, which limits glide distances, and limited film thickness, which limits glide distances and inhibits the operation of dislocation sources. In addition copper films showed both transgranular and intergranular crack growth under tensile loading, which was described by a thickness-limited toughness formulation [38]. Keller et al. studied the effects of film thickness, grain size, and passivation on the yield strength of sputtered Cu thin films on Si substrate. They reported that the yield strength of Cu films is well described by the dimensional constraint model proposed by Nix [39] combined with classical Hall-Petch grain-size strengthening [40]. Spolenak et al. studied electroplated Cu films and found that the yield stress at room temperature increases with decreasing film thickness [41].
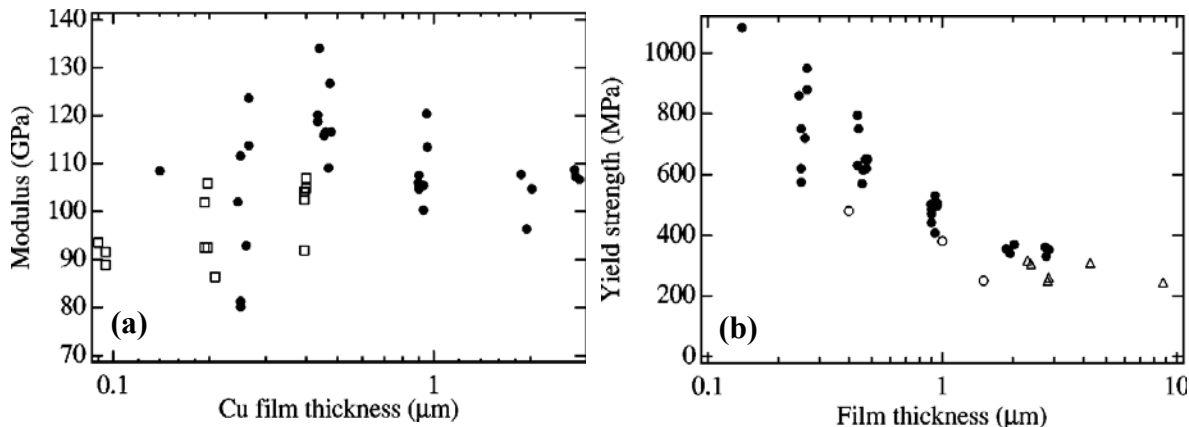
Fig. 17 (a) Young's modulus of Cu films with different film thicknesses on Kapton substrates (□: Cu on 7.6 μm Kapton; ●: Cu on 12.7 μm Kapton.) **(b)** Thickness dependence of yield strength of the Cu films (●: Cu on 12.7 μm Kapton; Δ: free standing, as deposited Cu; o: literature data) [42].

Yu and Spaepen measured the stress–strain curves of electron beam evaporated Cu thin films on Kapton substrates using a micro-tensile tester. They reported that the Young modulus is independent of film thickness (Figure 17a) and is about 20% below the value calculated from single-crystal elastic constants and that the yield stress depends strongly on the film thickness (Figure 17b). A substantial part of the yield stress was attributed to effect of the film thickness, by strain gradient plasticity theory [42].

Xiang et al. investigated the mechanical properties of electroplated free standing copper films and influence of thickness and microstructure using plane-strain bulge test (Figure 18b). Stiffness showed small dependence on thickness which is the result of the elastic anisotropy of Cu and the changes in the crystallographic texture of the films (Figure 18a). They reported that experimental moduli agree well with results obtained from single crystal elastic constants. Yield stress variations with film thickness and heat treatment were attributed to corresponding changes in the grain size. They also found

that film thickness and crystallographic texture have a negligible effect on strengthening of freestanding Cu thin films [43].
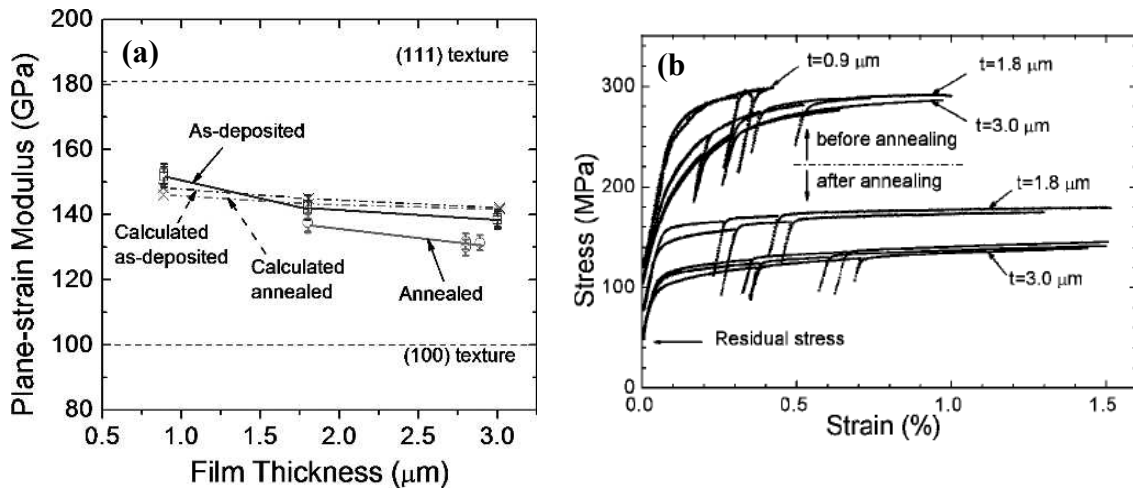
Fig. 18 (a) The variation of stiffness with film thickness and heat treatment. **(b)** The plane-strain stress-strain curves of freestanding electroplated Cu films [43].

I.4. Electrical properties of copper

As mentioned earlier, copper has the second highest electrical conductivity in periodic table and is the metal of choice in electrical power transmission and as well as interconnects in chips. Despite its good conductivity, copper is relatively soft in its pure form. High conductivity copper and copper alloys are focus of extensive research for decades. For convenience conductivity (σ) of metals is discussed in terms of resistivity (ρ) which is reciprocal of conductivity. Resistivity of metals can be represented by Mathiessen's rule [26]:

$$\rho = \rho_T + \rho_i + \rho_d + \rho_b \qquad (3)$$

where ρ_T, ρ_i, ρ_d, and ρ_b represent thermal, impurity, dislocation, and grain/twin/interface boundary contributions to overall resistivity. Temperature increase causes increase in the thermal vibrations (phonons) and lattice irregularities. These vibrations and irregularities act as electron scattering sources, and above ~70 K, resistivity increases linearly with temperature:

$$\rho_T = \rho_0 + At \tag{4}$$

where T is temperature in K, ρ_0 is intrinsic resistivity of particular metal and a is a constant. For lower temperatures, a power law equation is fitted to experimental data (Chapter V). Impurities in the form of solid solution also scatter electrons, therefore increase resistivity. Impurity contribution to resistivity is given by:

$$\rho_i = Ac_i(1-c_i) \tag{5}$$

where A is a constant independent of composition and a function of host and impurity metal, c_i is atomic percent impurity concentration [26].

In case of thin films, there are additional sources of electron scattering. Surface, substrate, and surface roughness which are negligible in bulk form. Similar to its effect on mechanical properties, thickness of the thin film also affects its resistivity, known as "size effect" [44, 45]. This effect becomes important when the thickness of the thin film comparable to (2–3 times) the room temperature mean free path of electrons, which for Cu is 39 nm. Interactions between the electrons and the surfaces of the films result in a net slowing down of the electron motion and an effective increase in the resistivity. The
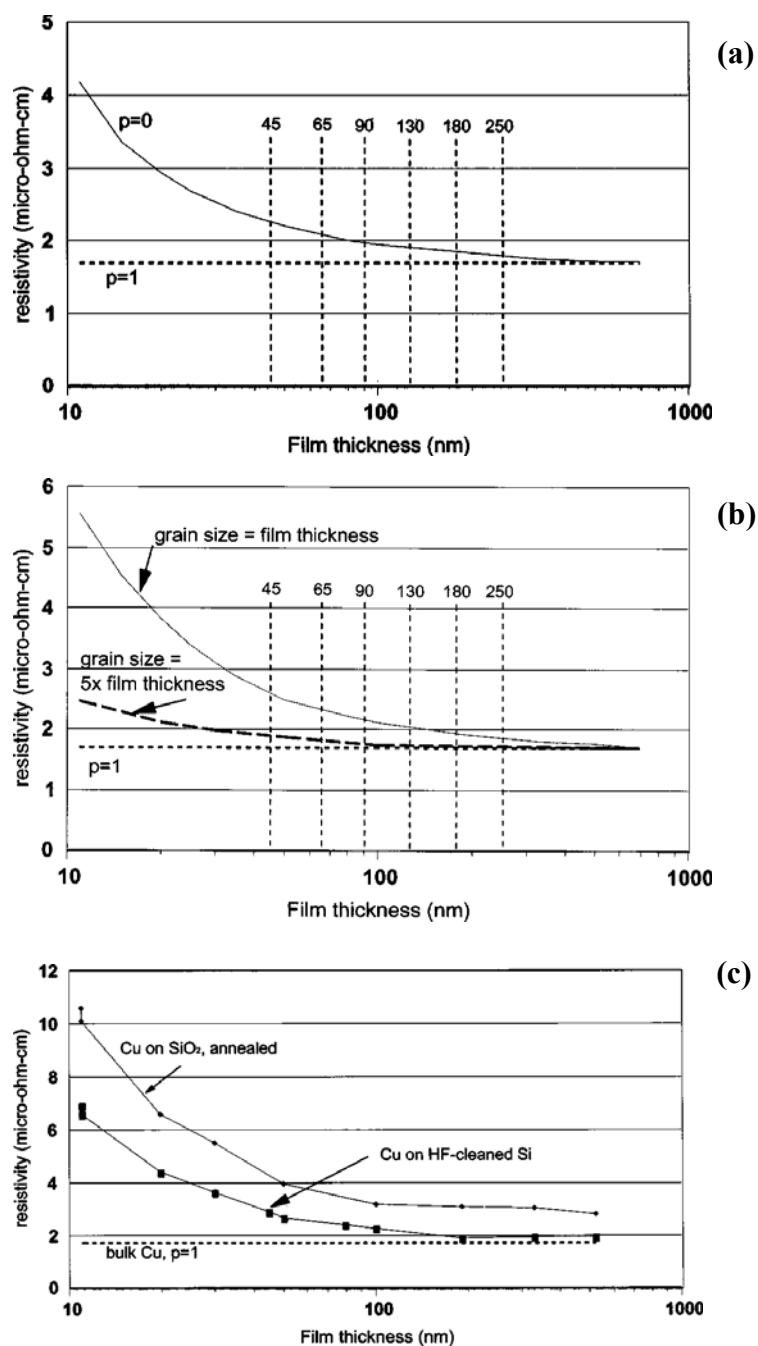
Fig. 19 Resistivity of copper film as a function of **(a)** film thickness; *p* is the scattering parameter, varies from 1 for fully elastic to 0 for fully diffuse **(b)** grain boundary and film thickness combined **(c)** substrate which changes microstructure. [46].

size related phenomena also include significant contributions from grain/twin boundary scattering and surface roughness, which in addition to impurities, result in additional electron scattering and reduced conductivity [46]. Mayadas and Shatkes [47] developed a model (MS model) describing the resistivity of polycrystalline metal films taking into account both contributions from external surfaces and grain boundaries. MS model is discussed in Chapter V.

Rossnagel and Kuan reported an extensive study on the effect of film thickness, grain size, and surface roughness on resistivity of sputtered copper thin films [46]. They found that the resistivity of Cu is sensitive to a range of effects in the thickness range near the electron mean-free-path, including electron–surface scattering, grain boundary scattering, and surface roughness. The results are summarized in Figure 19. Ke et al. studied an atomistic first-principles calculation of resistivity induced by atomically rough surfaces of thin Cu films. They showed that resistivity increases significantly due to surface roughness scattering and it is quite sensitive to both the amount and the nature of roughness [48].

In addition there are several studies on resistivity of copper alloys. The motivation for alloying is to increase the strength and maintaining the resistivity at reasonable values. Figure 20 presents hardness as function of conductivity of several copper alloys, and pure copper with different microstructures nanocrystalline, epitaxial, and nanotwinned [49]. Alloying usually increases the hardness/strength at the expense of conductivity. However, introduction of nanotwins causes slight decrease in conductivity

but provides an order of magnitude increase in strength. It is the motivation of this study to discuss mechanical, electrical, and thermal properties of nanotwins in copper films.
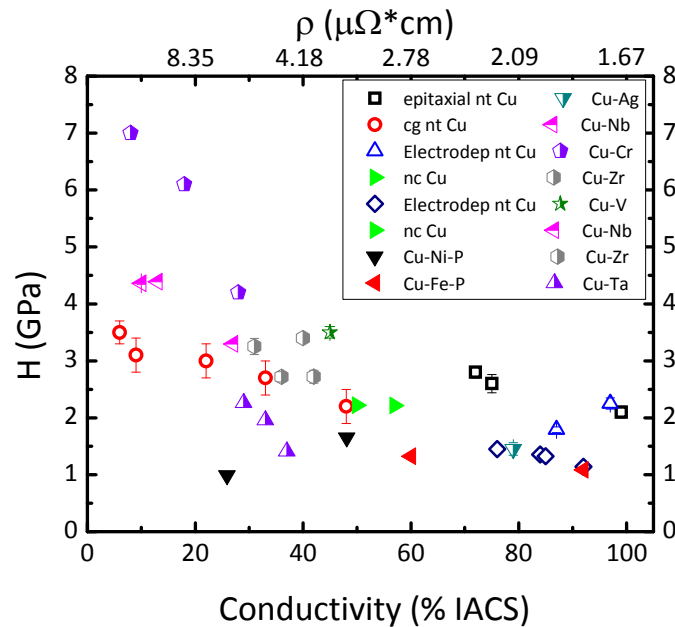
Fig. 20 Hardness as a function of conductivity in pure Cu and Cu alloys. In general, alloying and grain refinement increases hardness while decreasing the conductivity. Exception to this trend is seen in nanotwinned Cu [49].

I.5. Twinning

Twinning occurs when two separate crystals share some of the same crystal lattice points in a symmetrical manner. In some cases such as during the growth of a crystal, or if the crystal is subjected to stress or temperature/pressure conditions different from those under which it originally formed, two crystals are formed in a symmetrical fashion. These symmetrical intergrowths of crystals are called twinned crystals. What happens is that lattice points in one crystal are shared as lattice points in another crystal

adding apparent symmetry to the crystal pairs. Twinning, because it adds symmetry, never occurs in relation to the existing symmetry of the crystal [19].

Twins can be obtained as a result of different processing techniques. These are:

- Deformation (mechanical) twins

- Transformation twins (annealing is the most common)

- Growth twins

They are named after the processing technique. Among these three this thesis focuses on "Growth Twinning". The other techniques will be discussed briefly. One can refer to literature to get detailed information on the other techniques.

The history of work on research on twins goes back to as early as late 18th century. Romé de l'Isle was the first to describe twins in his account of the mineral staurolite-twins in 1783. Haüy made angular measurements on staurolite twins by contact goniometry, and observed that any face of one individual has a face of the other individual parallel to it in 1801. A nice historical review up to 1954 can be found in R.W. Cahn's review article [50]. All this work was limited to a study of stress-strain curves, X-ray diffraction and optical metallography. Several problems couldn't be solved by this work. For instance, the optical metallography revealed bands that were thought to be twinned regions but substructures in these bands, which could have been the individual twin lamellae, were not readily identifiable. The X-ray diffraction techniques could not detect the presence of small amounts of twin. Problem of twin nucleation could not be approached experimentally. These are all due to low resolution of techniques used. In 1963, however, J. N. Veneables used transmission electron

microscopy (TEM) and diffraction techniques for the first time [51]. Today, most of the crystal structure characterization involves the use of TEM, HRTEM etc. In this context Veneables work was outstanding and shed light on many problems.

I.5.1. Formation of twin boundaries

The most prominent lattice defects generated during boundary migration (e.g., during grain growth) are coherent twin boundaries (CBTs). There are several models that explain the formation of CTBs. *The dissociation model* proposes that twins are formed by dissociating a grain boundary into a twin boundary and a new grain boundary. The *stimulation model* proposes that a twin boundary is created if a growing recrystallized grain meets a dislocation-bearing fragment which lies in a twinned orientation to it. The *coalescence model* proposes twin boundaries to be formed if the orientation relationship between the impinging grains corresponds exactly to a twin orientation. The *growth-accident hypothesis* of twin-boundary formations follows the concept that twins are formed and terminated by errors of the stacking of the <111> planes which happen in a random way [52]. Studies by optical microscopy, photoemission microscopy, transmission electron microscopy, X-ray topography, grain-boundary migration experiments in bicrystals and polycrystals have been reported [52]. The results of these studies are inconsistent with the dissociation, the stimulation and the coalescence hypotheses. The observations so far available seem consistent only with the growth-accident hypothesis. In fact, in situ observations of twin formation in A1 by X-ray

topography agree with the evolution, shape and growth direction predicted by the growth-accident theory [52].

I.5.2. Annealing (transformation) twins

The basic definition can be given as types of twins that occur when a preexisting crystal undergoes a transformation due to a change in temperature/pressure. This commonly occurs in materials that have different crystal structures and different symmetry at different temperatures. Annealing twins were seen in gold as early as 1893 [53]. The mechanism that causes formation of annealing twins is not completely understood. Studies suggest that there are two main mechanisms responsible for twin formation which are growth accidents [54, 55] and nucleation of twins by stacking faults or fault packets [56, 57]. Several experimental and theoretical works suggest that the important factors affecting the frequency of formation of annealing twins are [54, 58-61]

- temperature and time of annealing;

- grain size, grain boundary velocity and energy;

- twin boundary or stacking fault energy;

- crystallographic texture;

- degree of prior deformation;

- presence of inclusions

A large grain boundary velocity favors the formation of annealing twins because growth accidents that are responsible for annealing twin formation are then more frequent. Naturally, low stacking fault energy also favors annealing twins since growth accidents are easier to create which is also the case for growth twins. The latter will be discussed in the next section. In fact, there is a simple equation which relates the twin density ρ to the grain size d and a constant b related to the inverse of the stacking fault energy:

$$\rho = \frac{b}{d} \times \log\left(\frac{d}{d_0}\right) \tag{6}$$

where d_0 is the grain size at which ρ is zero. Interested readers can refer to literature for further details on the formation mechanisms of annealing twins [54-57, 59, 61, 62]. Figure 21a and Figure 21b show annealing twins in austenitic stainless steel and brass respectively [63].
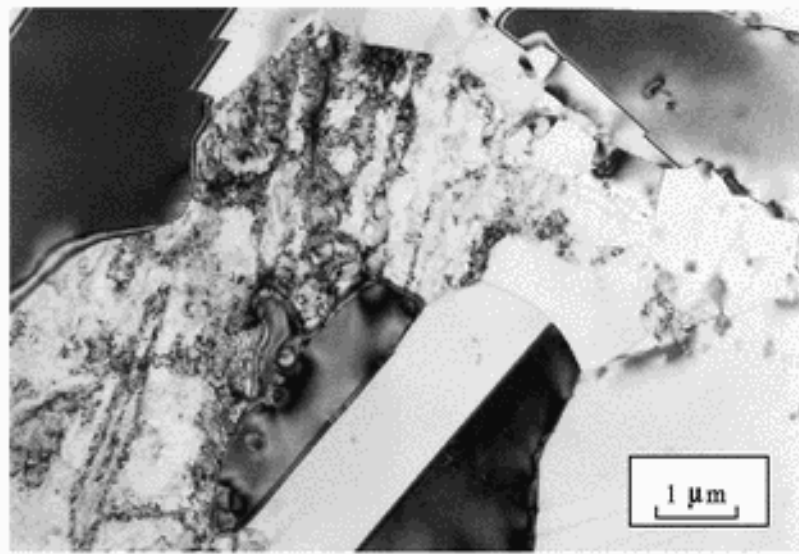
Fig. 21a TEM image of annealing twins in austenitic stainless [63].
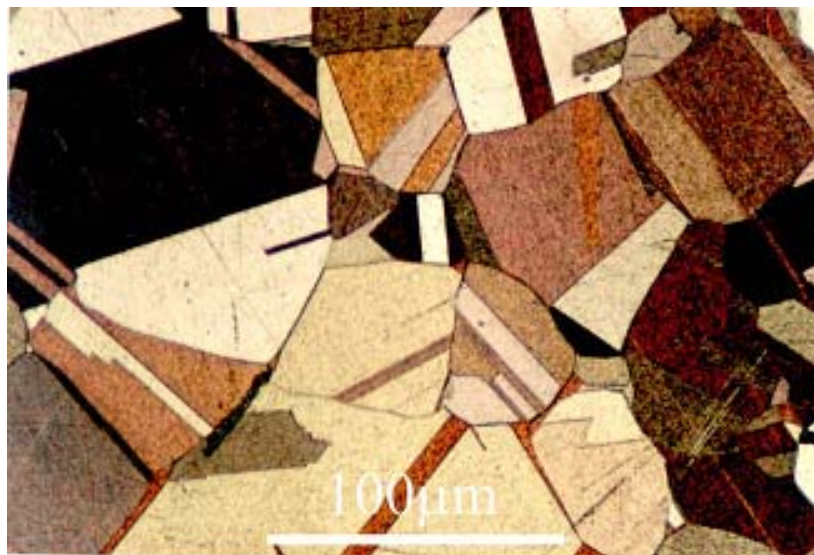
Fig. 21b Annealing twins in brass [63].

I.5.3. Deformation twins

At temperatures below those at which individual atoms move by diffusion, slip and twinning are the major deformation modes that enable a solid to change shape under the action of an applied stress. In principal, deformation twins (also called mechanical twins) form by a homogeneous simple shear of the parent lattice. This implies a highly coordinated individual atom displacements, in contrast to the apparently chaotic processes of generation and growth of slip bands during glide deformation [64]. Figure 22 shows a schematic of the twin formation under applied stress. Note the movements of individual atoms to form a twin, a mirror image of the parent crystal.

Plastic deformation of crystalline materials has long been known to occur by the movement of line defects called dislocations. A perfect dislocation moves one part of the crystal by a complete lattice vector with respect to the other, such that it leaves a perfect lattice. A partial dislocation, however, moves one part by less than a complete lattice vector, leaving a faulted layer in the crystal. If this occurs on consecutive planes, it results in the formation of a twin, which has a lattice that is a mirror of the host lattice.

The formation of deformation twins is divided into nucleation and growth stages. Twin nuclei may form under the action of applied stress (Figure 22) in a near-perfect region of a crystal (homogeneous nucleation) or, alternatively, may form only when a suitable defect configuration is present (heterogeneous nucleation). Theoretical calculations and experimental evidence do not support the concept of homogeneous nucleation of twins. In general deformation twinning occurs in metals that have BCC and HCP crystal structures (limit number of slip systems), at low temperatures, and at high

rates of loading (shock loading), conditions under which the slip process is restricted; that is, there are few operable slip systems [64]. Recent experimental work [65] and MD simulations [66] also show the presence of deformation twins in Al (Figure 23a and Figure 23b) which has high stacking fault energy (136 mJ/m^2) compared to some other low SF energy FCC metals such as Cu. The amount of bulk plastic deformation from twinning is normally small relative to that resulting from slip. However, the real importance of twinning lies with the accompanying crystallographic reorientations; twinning may place new slip systems in orientations that are favorable relative to the stress axis such that the slip process can now take place. It should also be noted that although twins are similar in the sense of symmetry, annealing twins should be distinguished from mechanical twins. In the latter case, the twin orientation is generated by a large deformation of a single grain. There is a lot of strain energy associated with the formation of a mechanical twin, whose shape is determined strictly by the need to minimize strain energy. This contrasts with annealing twins where the shape is determined by the need to minimize interfacial energy. Mechanical twins tend to be lenticular, i.e., lens shaped with sharp edges, since this reduces the long range elastic strains [64].
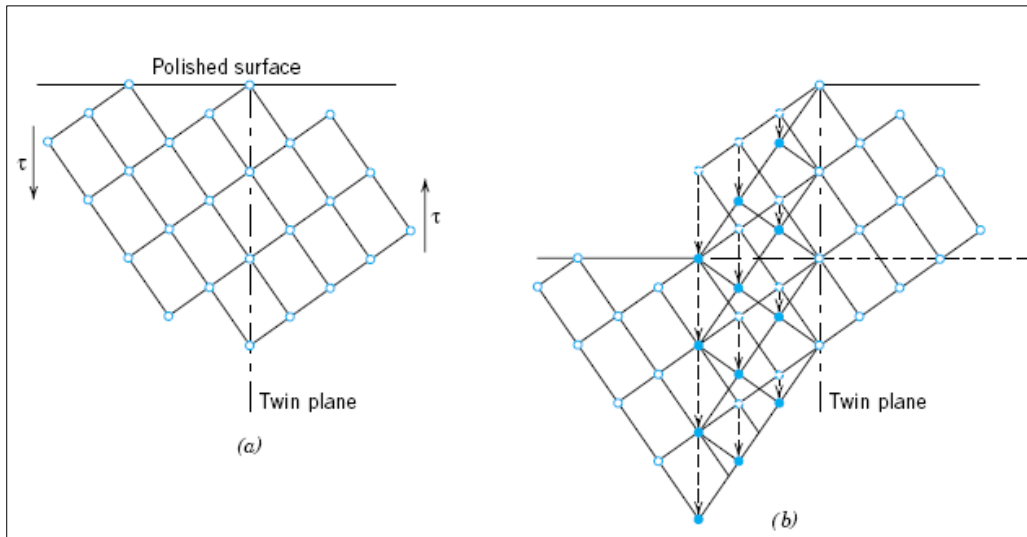
Fig. 22 (a) Schematic diagram showing how twinning results from an applied shear stress. **(b)** Open circles represent atoms that did not change position; dashed and solid circles represent original and final atom positions, respectively [26].
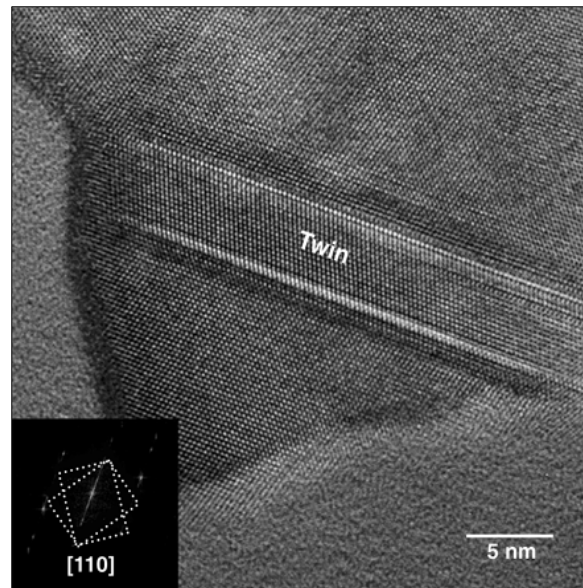
Fig. 23a TEM micrograph of deformation twins around an indent in nanocrystalline Al. The inset shows the indent with the fourfold geometry [65].
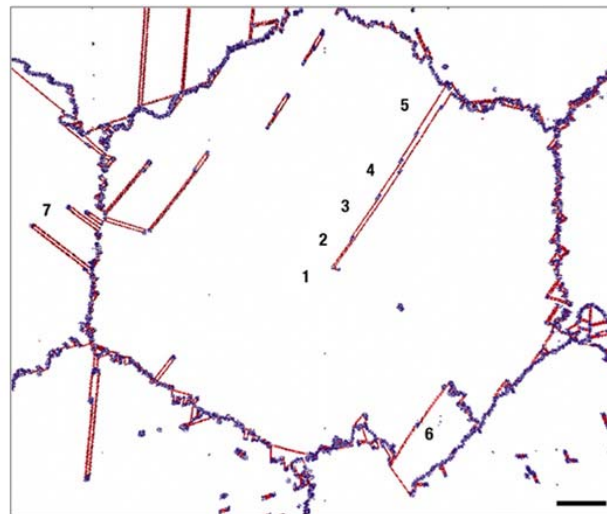
1. ABCABCABCABCABCABC
2. ABCABABCABCABCABCABC
3. ABCABACABCABCABCABC
4. ABCABACBCABCABCABC
5. ABCABACBCBCABCABC

Fig. 23b Results of molecular dynamic simulations on Al. The stacking sequences for regions 1–5 shows twins [66].

I.5.4. Growth twins

This is the type of twins that are present in current work. Most crystals grow by adding layers of atoms, one layer at a time (layer by layer growth). For instance, (111) textured Cu will grow in a way that can be described simply as: If the first layer of atoms (or plane) on the substrate is called **A** and the next layer which is in a different position than **A** is called **B** and the following layer is **C** that is also different than both **A** and **B** will be followed by another **A** and so forth, this sequence will repeat it self such that a structure will be built in the following stacking sequence: **ABCABCABCABC…** But, if an error during growth can cause a fault in this stacking. This fault is called stacking fault (SF). A SF can be intrinsic or extrinsic. The former assumes a missing layer, whereas the latter assumes introduction of an extra layer. Twinning is a special case of SF which has lower energy and higher symmetry than a SF. During the growth if a layer of atoms becomes misplaced and assumes the wrong positioning in a way to form the following sequence a twin forms: **ABCABCABCACBACBACBA**

In the above sequence, the first blue **C** layer next to the middle red **A** layer is wrong because there should be a **B** layer next. The rest of the sequence is then repeated as if nothing happened and the crystal grows outward in both directions until finished growing. Directly through the middle **A** layer, a mirror plane is produced and the right side of the crystal will be a mirror image of the left side just as a left hand is the mirror image of the right hand. The mirror is easier to see if the **A** is replaced by a vertical line | which represents a mirror plane as in: **ABCABCABC | CBACBACBA.** Note that twinning changes stacking sequence of FCC to HCP locally as shown in Figure 24.
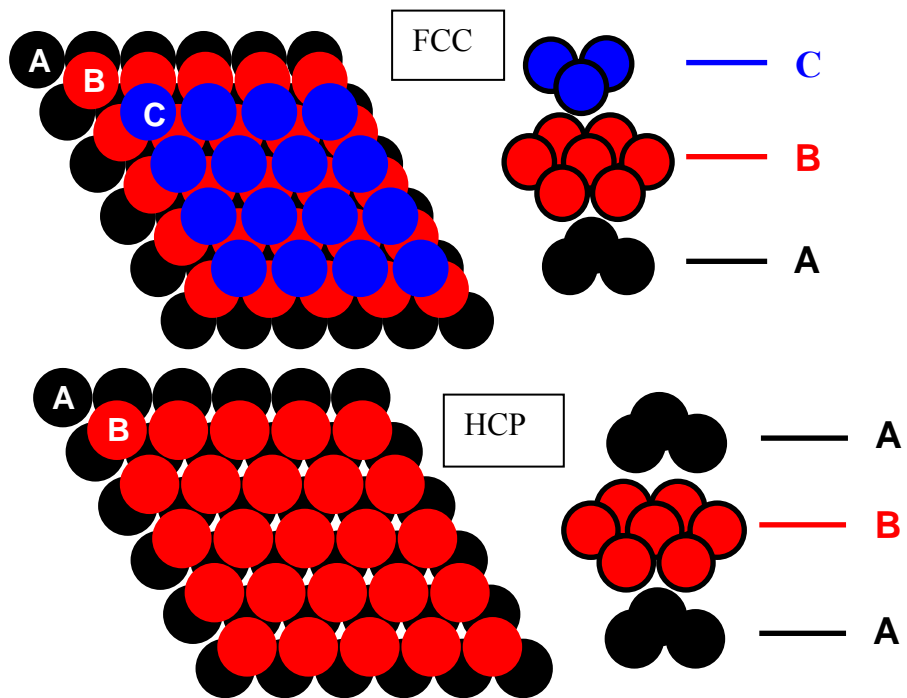
Fig. 24 Simple model showing stacking sequences of FCC and HCP close pack structures.
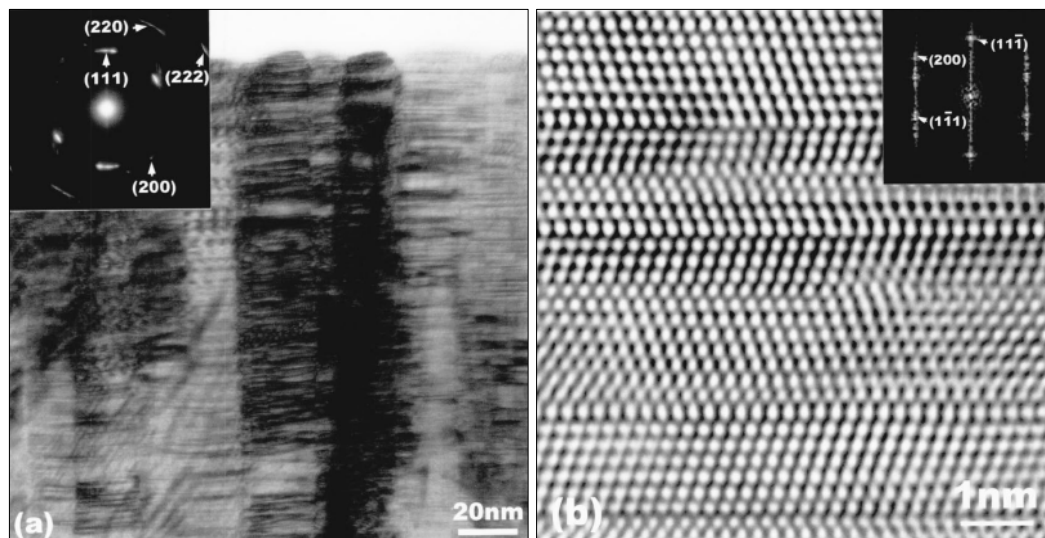
Fig. 25 (a) TEM of 330 SS films with an average columnar grain size of 30 nm, showing high density growth twins **(b)** Twin interfaces can easily be detected in HRTEM image [67].

There are two methods widely used to produce nanoscale growth twins, electrodeposition [68-72] and PVD (Sputtered SS330 shows nanotwins in Figure 25) [15, 67, 73]. However, recent research shows that the formation of twins is fundamentally different in these techniques [74-76]. The formation of twins in sputtered films will be discussed in detail. In electrodeposition, it was proposed that, during pulse deposition of Cu films, highly strained Cu can undergo re-crystallization and grain growth to relax stress and form strain-relaxed nanotwins. In addition, the strain-relaxed nanotwinned Cu is energetically more stable than the strained fcc Cu [76]. The story is totally different in the case of sputtering.

During PVD, initial nuclei that form may be either 'perfect' or have stacking faults and/or twins. The total free energy (ΔG_1) of a disc-shaped 'perfect' nucleus with radius r and height h is given as:

$$\Delta G_1 = 2\pi r h \gamma - \pi r^2 h \Delta G_V, \tag{7}$$

where γ is the surface energy and ΔG_V is the bulk free energy per unit volume driving the nucleation. Introduction of a twin interface changes Eq. (7) to:

$$\Delta G_2 = 2\pi r h \gamma - \pi r^2 h \Delta G_V + \pi r^2 \gamma_t, \tag{8}$$

By adding an extra $\pi r^2 \gamma_t$ term, where γ_t is the twin boundary energy. Using Eqs. (7) and (8), the critical size r^* may be derived by setting the differential of ΔG with respect to r to zero. For the perfect nucleus case, it follows that

$$r^*_{perfect} = \frac{\gamma}{\Delta G_V} \tag{9}$$

For the twinned nucleus case, the result is

$$r^*_{perfect} = \frac{\gamma}{\Delta G_V - \dfrac{\gamma_t}{h}} \qquad (10)$$

Note that ΔG_V will be positive and hence, $r_{perfect}^* < r_{twin}$ which implies that the nucleation of a perfect nucleus will be preferred to a twinned nucleus. However, for low γ_t and high values of ΔG_V the difference between $r_{perfect}^*$ and r_{twin}^* will be negligibly small. Then, the formation of twinned nuclei may occur randomly during growth. Also ΔG_V is proportional to deposition rate. As a result higher deposition rate and lower stacking fault energy are two important parameters that favor the formation of twins. The practical meaning of these results will be the following: Deposition rate required to form a certain twin density in Ag ($\gamma_{SF} = 20$ mJ/m^2) will be different than that of Cu ($\gamma_{SF} = 50$ mJ/m^2). Figure 26a shows that at higher deposition rates the difference for the cases of perfect and twinned nuclei becomes negligible. Figure 26b shows the effect of twin boundary energy on r_{twin}^* at a constant deposition rate of 0.4 nm/s. The horizontal dotted line shows the value of $r_{perfect}^*$ at this deposition rate. Note that at very low γ_t, $r_{perfect}^* \approx r_{twin}^*$, but with increasing γ_t, r_{twin}^* rapidly increases as compared to $r_{perfect}^*$, indicating that twin or stacking fault nucleation becomes much more difficult at low deposition rates as the fault energy increases. For example, Al films deposited at rates of a few nm/s are unlikely to show any stacking faults or twins.

51
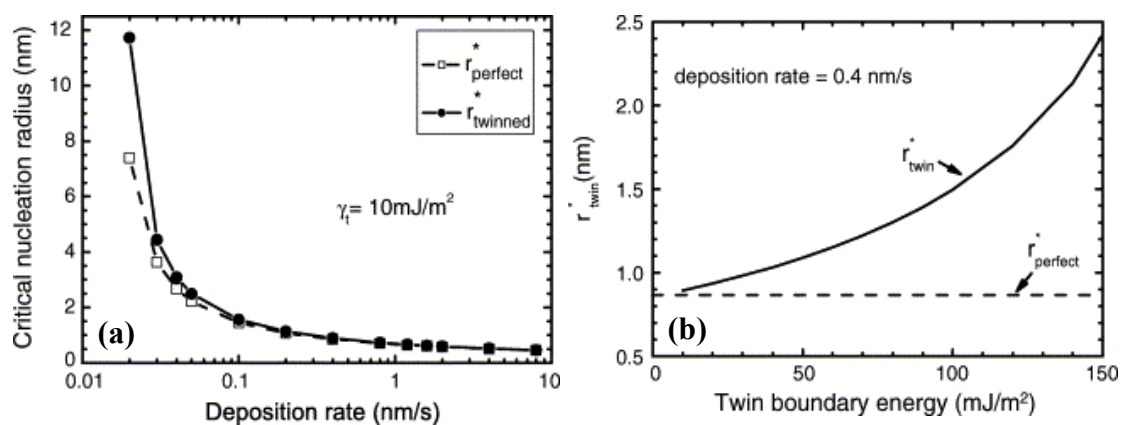
Fig. 26 (a) The formation of twins is favored with increasing deposition rate at constant twin boundary energy. The difference becomes negligible after 0.4 nm/s. **(b)** At a deposition rate of 0.4 nm/s, it is difficult to form twins in a metal with high stacking fault energy, such as Al [74].

CHAPTER II

EXPERIMENTAL TECHNIQUES

II.1. Fabrication of nanotwinned Cu films

Magnetron sputtering (Figure 27) is the technique used to produce nanotwinned Cu films in this work. A Cu 99.999% target was sputtered to produce 1-40 μm thick Cu films/foils. The difference between epitaxial and polycrystalline nanotwinned Cu films is the choice of substrate. For polycrystalline Cu films Si (100) with a native 1 μm thick SiO_2 layer was used. For epitaxial growth, however single crystal substrates of Si (100), (110), and (111) were etched in HF. After etching the substrates were placed into chamber immediately. The time interval between etching and placing the etched substrates into high vacuum chamber is usually less then 10 minutes. The chamber was evacuated to a base pressure of 5×10^{-8}-3×10^{-7} torr prior to deposition. Prior to deposition, Cu is also pre-sputtered to clean the target itself from contamination. The depositions are made at room temperature. No heating or cooling was applied to the substrate during deposition. However, for long depositions such as 40 μm thick foil, there was usually a 10 minutes pause time after every 10 μm. The purpose of pausing is to eliminate the over heating of substrate. A thermocouple is placed on the Cu sample holder to monitor the temperature fluctuations during deposition. Depending on the longevity and power used the temperature was usually around 50-60 °C at most. It should also be mentioned that the thermocouple was in contact with the Cu sample
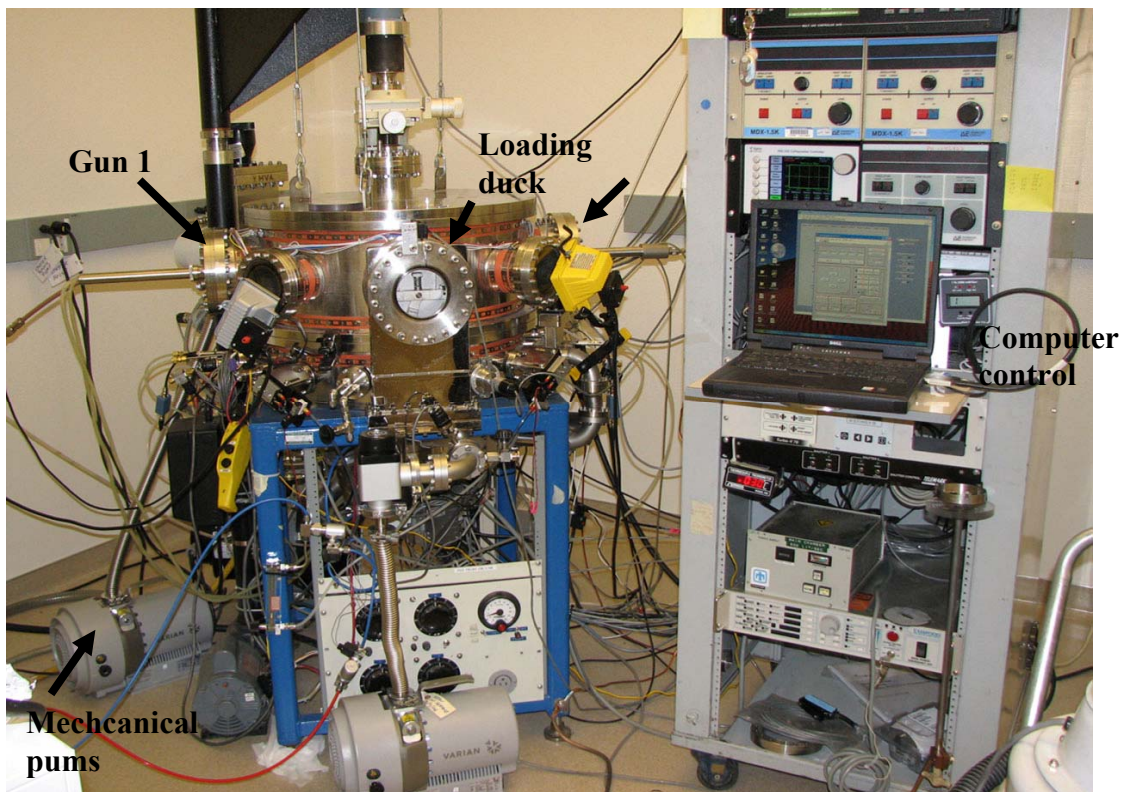
Fig. 27 Magnetron sputter system. There are 3 guns in this system. The system is fully computer controlled (The 3rd gun is at the back side, not seen in the photo).

holder plate but the actual temperature of the film being deposited is expected to be higher than what thermocouple displays because of the Si substrate between the film and holder plate. Nevertheless, high resolution TEM images show a clear Cu/Si interface.

The deposition rate was varied in the range of 5–100 Å/s by controlling the dc power to the magnetron gun and the distance between target to substrate. For thick (>20 µm) polycrystalline Cu films deposition rate was typically 5-20 Å/s. For thin films, the deposition rate of up to 100 Å/s was used. Since the film is thin and deposition rate is high, it takes only 100 seconds to deposit a 1 µm thick film at 100 Å/s. It is not expected to see a dramatic change in temperature from beginning to end since at this rate thermocouple shows an increase of temperate about 2-4 °C/minute.

The basics of sputter deposition are discussed in the introduction section. Among the other sputtering techniques, magnetron sputtering is the most common DC sputtering technique. For the same voltage applied, one to two orders of magnitude more current is available in magnetron than DC discharges. Existence of magnetic field traps the electrons uniformly close to the surface of target as shown in Figure 28a. A parallel magnetic field is superposed on the glow discharge. Electrons in the glow discharge show cycloid motion, and the orbit drifts in the direction of the $E \times M$, where E and M denote the electric field in the discharge and the superposed magnetic field. Magnetic field is oriented such that these drift paths for electrons form a closed loop. This causes an increased rate of collision between the electrons and the sputtering gas molecules. The magnetic field causes the plasma density to increase which leads to increased current density at the cathode and hence increase the sputtering rate and efficiency of the sputtering reactor. Sputtering with a transverse magnetic field produces several important modifications. Target-generated secondary electrons do not bombard substrates because they are trapped in cycloidal trajectories near the target, and thus do not contribute to increased substrate temperature and radiation damage. This allows the use of substrates that are temperature-sensitive (for example, plastic materials) and surface sensitive (for example, metal-oxides-semiconductor devices) with minimal adverse effects. In addition, this class of sputtering sources produces higher deposition rates than conventional sources and lends itself to economic, large-area industrial applications.
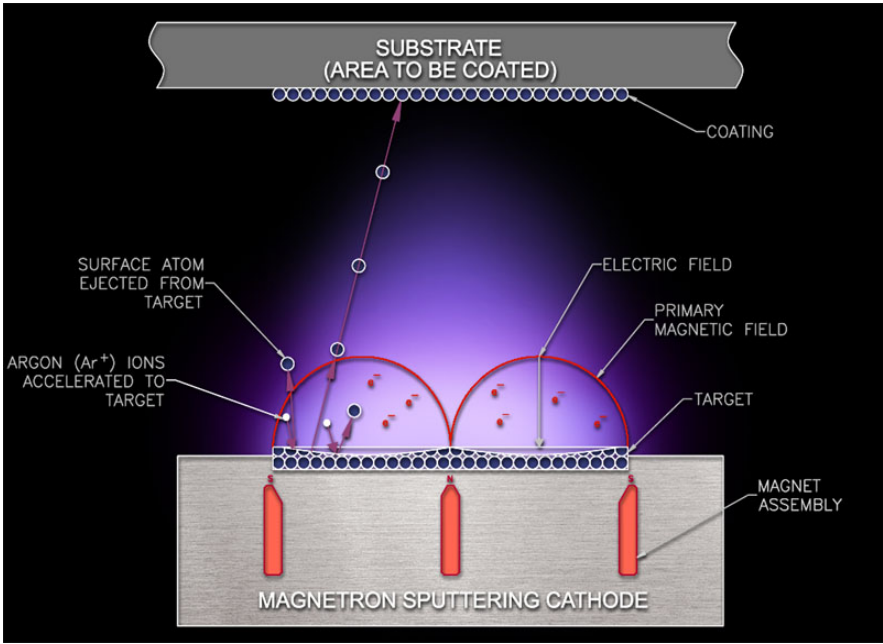
Fig. 28a Working principle of magnetron sputtering [77].
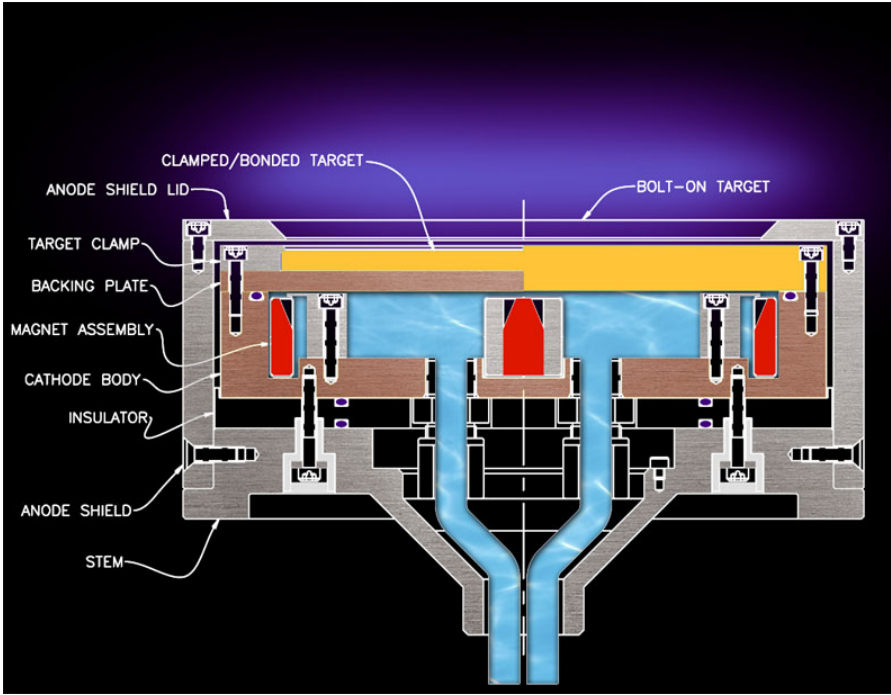
Fig. 28b Inside magnetron sputter gun [77].

The shape of magnetron sources vary depending on applications. There are cylindrical, conical, and planar magnetron sources, all with particular advantages and disadvantages for specific applications.

Figure 28b shows a schematic of a magnetron gun assembly. In the assembly backing plate is also shown behind the target. Backing plate prevents the cooling fluid (usually water) from leaking into chamber. That can cause problems such as poor vacuum, or it can electrically connect target clamp with the shield, and short the target. Gun can also be shorted also because of the metal flakes than can fall in between anode shield and target clamp. It is important to check the resistance between these two after changing the targets. A commercial vacuum cleaner is usually used for that purpose. It is important to understand the gun components. If one fails to place the shield back after changing the target, shield will also sputter together with the target. This will introduce contamination to deposited film. An example of this will be given in the next chapter.

II.2 Microstructural characterization of nanotwinned Cu thin films

II.2.1. Residual stress measurement

Thin films on a substrate are usually in a stressed state (compressive or tensile). The internal stress in a film causes the film-substrate compound to bend until an equilibrium state is reached. From the curvature of the elastically deformed coated substrate the average film stress can be found. The curvature of a stress bar (substrate) is measured prior to deposition by scanning the laser beam along the longitudinal direction of a stress bar with rectangular shape. After deposition, the curvature of the same stress

bar is measured again. Several measurements (5-10) are taken, and average values are calculated. Then, using the Stoney equation residual stresses in the deposited films are calculated.

$$\sigma = \frac{Et_s^2}{6(1-v)Rt_f} \tag{11}$$

$$R = \frac{1}{1/R_1 - 1/R_2} \tag{12}$$

where E, v, t_S, and t_f are Young's modulus, Poisson's ratio, thickness of the substrate and thickness of the film respectively. R_1 and R_2 are radius of the curvatures before and after depositions respectively. The results could be positive or negative depending on the state of the stress. A positive value implies tensile and a negative value implies compressive residual stress. It is also important to note that there are assumptions in using the Stoney equation. A first requirement is that the substrate is thick compared to the thickness of the film, but still thin enough that it bends due to the stress in the film. A second requirement is that the film is in a state of plane stress, meaning that in the plane of the film the stress is independent of direction.

The laser curvature measurement system used in this study is home-made and shown below in Figure 29. It is a simple yet powerful tool for measuring the residual stress in thin films. The system contains a laser, several mirrors, and an optical table. Commercial products are also available in the market.
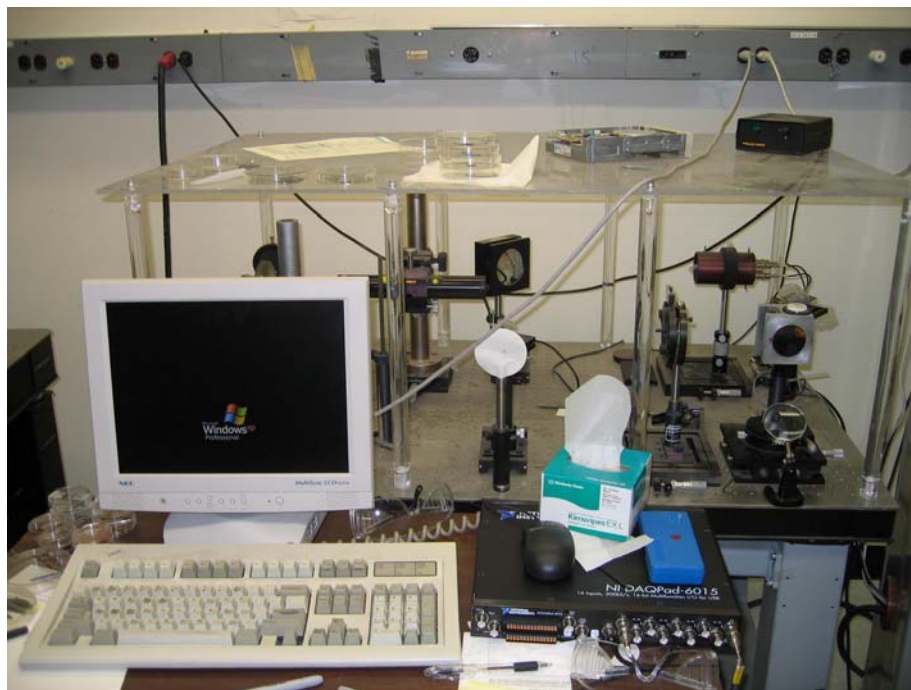
Fig. 29 Laser curvature measurement set-up.

II.2.2. X-ray diffraction

The crystallographic texture of the polycrystalline and epitaxial Cu films was determined with X-ray diffraction (XRD) in a Rigaku Ultima III diffractometer. X-ray diffraction is a powerful and non-destructive tool to analyze the microstructure of thin films. It is a quick and versatile technique and usually does not require sample preparation. XRD is extensively utilized in this study especially for studying the crystallinity of epitaxial Cu films. The advantage of using XRD in this study can be summarized as follows. First of all, epitaxy and texture are the two microstructural characteristics studied in this thesis. However, epitaxial and textured materials show similar diffraction behavior. Hence, to determine if the film is textured or epitaxial

requires additional experiment besides he regular θ-2θ scans. That can still be done by using X-ray diffractometer which is capable of pole-figure measurement (performing rocking curve measurement or performing in-plane and out-of-plane crystallinity measurement). In this study, instead of using pole-figure experiments we conducted extensive TEM experiments to determine the crystallinity of Cu films. X-ray was also frequently used to determine if Cu is highly textured or has polycrystalline nature.

II.2.3. Scanning electron microscopy (SEM)

The surface morphology of the polycrystalline foils before and after deformation was characterized using FEI Quanta SEM using a field emission gun. After rolling the surface and cross section of the foils were examined for uniformity and cracks or fractures. Examination of the surface of the rolled foils does not require sample preparations. However, for the cross-sectional SEM analyses rolled foils were sandwiched between two Si pieces using M-bond, and then grinded using SiC grinding paper (15 uμ) and polished with diamond lapping papers (final polishing 1 uμ). One has to pay attention not to float M-Bond on to Cu foil when sandwiched between Si substrates to avoid the observation of artifacts. Secondary electron (SE) detectors were used in the experiments to examine surface morphology of rolled Cu foils.

II.2.4. Transmission electron microscopy (TEM)

TEM is critical in examinations of the size of various features in nanotwinned Cu films, such as twins, domain, and columnar grains. In addition to size, crystallographic

directions also play an important role. For instance, nanoscale twins in sputtered Cu films can only be observed from cross-sectional view, not from top-down view (plan view). Furthermore, in epitaxial nanotwinned Cu films only a specific orientation will reveal twins. The details will be discussed in following chapters. JEOL 2010 operated at 200kV and JEOL 3000F operated at 300kV were used for low magnification and high magnification (atomic resolution) images respectively. The former also allows one to tilt the sample to higher angles (±45°) due to larger gap between pole pieces. Smaller gap in pole piece of JEOL 3000F allows higher resolution but limits the tilting capability of TEM.

We will now briefly introduce the components and working principle of TEM. As the name implies, in TEM a beam of electrons is transmitted through an ultra thin specimen, interacting with the specimen as they pass through. An image is formed from the interaction of the electrons transmitted through the specimen, which is magnified and focused onto a fluorescent screen. The image on the screen can be acquired on a layer of photographic film, or can be detected by a CCD camera. Both of these techniques are utilized in this study. They have different advantages. A film needs to be developed in a dark room using chemical (developer, fixer etc). Therefore requires extra effort, however captures a much larger view area than a CCD. On the other hand image acquired using CCD does not require extra work and can be analyzed immediately. One can rapidly check, with CCD, the quality of the image (stigmatisms and focus etc) on the computer screen. However the view area of current CCDs is usually much smaller than that captured by a film. Using smaller magnifications together with diffraction aperture (not

objective) the view area can be enlarged. It is up to user to choose one over the other. We have utilized CCD whenever it was necessary.

The reason that TEM microscopes are capable of imaging at a higher resolution than light microscopes, is because of the small de Broglie wavelength of electrons. This enables the instrument to be able to examine fine detail as small as a single column of atoms. At lower magnifications TEM image contrast is affected by the absorption of electrons in the material, the thickness and composition of the material, and defects in the material. At higher magnifications complex wave interactions modulate the intensity of the image, requiring expert analysis of observed images. Figure 30 is a picture of TEM used in this study.

Fig. 30 JEOL 3000F, transmission electron microscope.

II.2.4.1 Sample preparation for TEM

Sample preparation for TEM studies, whether cross-sectional or plan view, is a challenge because of the tiny dimensions of specimens. Typically a TEM holder has about 3 mm space for the sample to be analyzed. However the thickness of the electron transparent film is on the order of nanometers. Focused ion beam cutting (FIB) is a new method of sample preparation for TEM. The advantages of FIB can be summarized as the success rate, large electron transparent thin area, as well as the precise tailoring of the shape and the location of the area of interest. Today, there are several in-situ TEM analysis techniques that require the usage of FIB instrument. There also are some concerns with FIB cutting such as ion irradiation damage and local heating. A thin Pt film is typically coated on the surface of interest area to avoid ion irradiation damage. If the sample is temperature sensitive it may be a good idea to avoid the FIB cutting technique. The classical sample preparation method was used in this study that includes several steps for a sample to become electron transparent. A free standing foil requires just one additional step than a film on a substrate. In both cases the films need to be sandwiched between Si pieces for protection. Free standing foils of about 2x2 mm are cut using a scissors. The foils are then glued between two Si pieces using M-bond and pressed to cure. Normally M-bond cures at about 100 °C in 3 hours. However in some cases where heating is prohibited, we allow the M-bond to cure at room temperature for 3-4 days. For instance rolled Cu foils are not heated because heating can cause relaxation or annihilation of dislocations. Epitaxial films cannot be heated because heating can cause formation of silicide at the Cu/Si interface. In short, when preparing samples for

TEM, we cure M-bond at room temperature. Once the sample is cured, it is then bonded on glass cylinder using crystal bond for grinding and polishing experiments. Note that crystal bond also melts at around 70 °C, so one has to cool the sample quickly (in 10-15 seconds) to prevent the formation of silicides. Once the first side is finished with a 1 micron diamond lapping paper the sample is turned up-side down and the other side is grinded down to 80-10 μm thickness. Then the sample is further thinned by Gatan dimpler. Figure 31 shows a simple schematic of an ideal sample after dimpling. The last step is ion-milling the sample. Before taking the film to ion-mill, it is bounded to a ring (a TEM grid) for support and handling. Usually low energy milling with 4-5 kV followed by polishing with 2 kV results a good sample assuming all the steps are done properly including ion-milling.
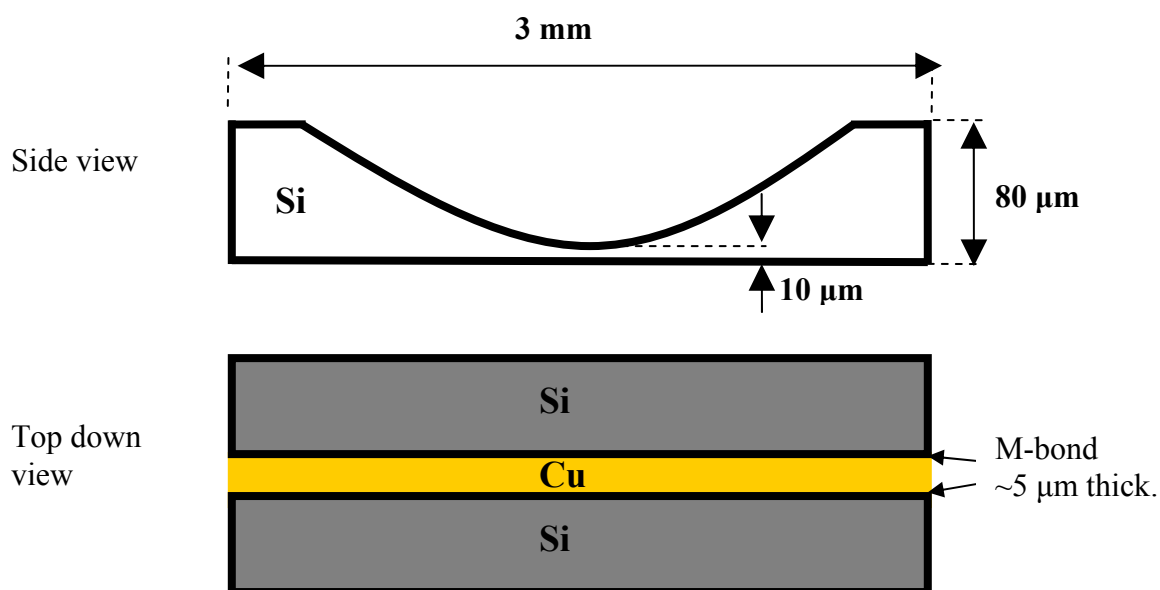
Fig. 31 (Top) Side view of a sample after successful dimpling. The sample is ready for ion-milling. (Down) Top-down view of a sandwiched sample. No gap between Cu film and Si pieces is a key for successful sample preparation.

The sample preparation steps can be summarized as:

1. Cutting the required dimension using Diamond pen/saw

2. Rotary grinders for rough lapping/ polishing.

3. Tripod polishers for fine finish polishing.

4. Dimpler thinning.

5. Ion mill thinning.

There are several issues associated to the ion-milling process. Basically ion-milling is a sputtering process. One needs to be careful with the energy to be used for milling. Higher energy can get the job done quickly but it can also damage the sample. A moderate energy followed by polishing is needed. Polishing is also important because some of the sputtered particles can re-deposit onto the film. Failure to clean those can lead to a totally different microstructure. We have used Gatan Precision Ion Polishing System (PIPS) for ion milling. For cross-section samples one sputter gun was kept on the top at ~5° and the other one is kept down at 6°. The milling energy was 4 kV and followed by a 5-10 minutes polishing at 2 kV. In the case of polycrystalline nanotwinned Cu, the foil can be cut in any direction since the grains are randomly oriented in the plane. However, the direction is important for epitaxial nanotwinned films because the domains are not randomly oriented. If the cutting is not done correctly, then one may not be able observe the twins under TEM because of the geometrical constraints. The epitaxial Cu films on Si (110) substrates must be cut in such a way that it will allow the cross-sectional view of Cu from <110> direction (or Si <111>). Fortunately this is the easy cut direction for Si (110) substrate. Figure 32 depicts a simple schematic.

Red arrow indicates the Si [112] (corresponds to Cu [112]) which does not reveal twins.

60°

Blue arrow indicates the Si [111] (corresponds to Cu [110]) which allows one to observe twins.

Si (110) substrate
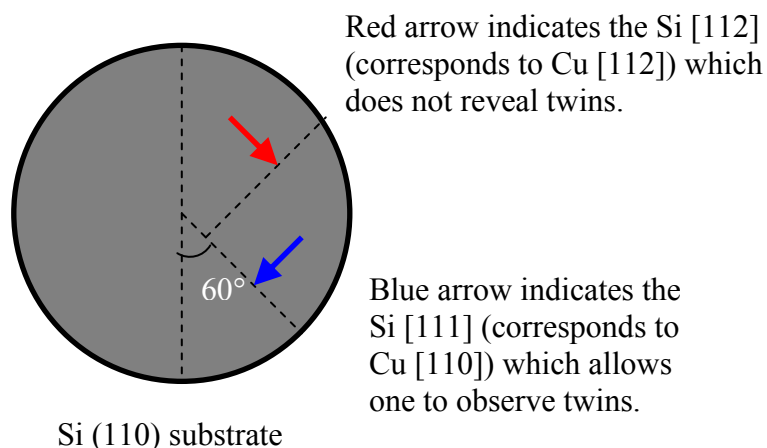
Fig. 32 Epitaxial nanotwinned Cu films require careful examination for the direction to be cut.

The procedure for plan view sample prep is somewhat easier. In this case for a film on substrate the film side does not need any polishing. Free standing foils can be directly glued on a Mo (or Cu) ring and ion-milled. For a film on substrate, a slice (about 2 × 2mm) of Cu over silicon is cut with the help of diamond tip cutting pen. The slice is then cleaned gently using acetone to remove all the impurities on the surface of the copper film; slice is bonded to polishing crystal cylinder with Cu film facing down, so that the silicon substrate could be polished. The slice is polished to an approximate thickness of 80 μm using polisher, followed by dimpling to a final thickness of about 10 μm on Gatan dimple polishing machine. The specimen is then ion milled to obtained the required electron transparency by using Gatan PIPS, with ion beam energy at 4KeV and dual beam configuration. Both top guns are oriented at angle 5.5° and sample rotation speed is kept at 3rpm.

II.3. Electrical properties: Resistivity measurements

The temperature-dependent (4–300 °K) electrical resistivity measurements were made with a low-frequency ac resistance bridge. A four-probe sample configuration was used, and Ohmic contacts were made with a silver conductive paint. A commercial physical properties measurement system (PPMS) with Four Point Probe resistant test setting was used for the resistivity measurements. Most of the times resistivity measurements are made on Cu films that are deposited on to pre-cut (using wafer saw) substrates that is 2x12 mm in dimension. Four point probe resistance measurement test is a relatively simple resistivity measurement technique, without any curve fitting process and any need to the measurement of physical dimensions of the resistor. Figure 33 shows a schematic of a sample for four point resistivity measurement. Contacts are made using thin Pt wire. Pt wires are connected to sample using silver paste and to sample holder by soldering. Pt wire is usually very stiff and needs annealing. Also poor contacts cause problem during temperature dependent measurements. Especially at low temperatures the differences between coefficients of thermal expansion can fail the experiment by causing a contact to pop off the film. Therefore special attention must be paid when using silver paste to connect Pt wire to sample.

Measured resistance R can be converted to resistivity using the following relation:

$$\rho = \frac{R \times w \times t}{l} \tag{13}$$

where w and t are the width and thickness of the film on the substrate. l is the distance between two contact points that the voltage is read. Attention must be paid to the size of the contacts.
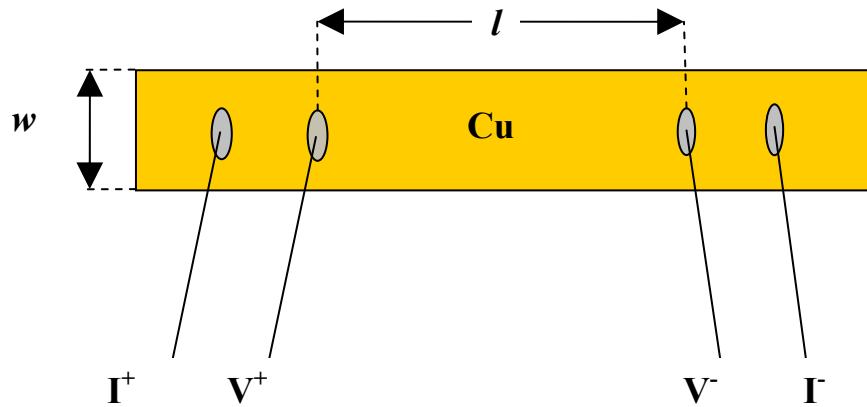
Fig. 33 Schematic of a four point resistivity measurement.

Usually the distance from the center of the two contacts is measured as l. However, the size of the contact needs to be as small as possible for an accurate measurement. Also, the contacts must be made using a material that has better conductivity than the material to be tested. It is also important to note that the current distribution between two contact points is not uniform. For a more accurate measurement (errors associated with the shape of the sample that is being tested) we have also determined the resistivity using Van der Pauw method [78]. The four point test results are also confirmed with another sample using Van der Pauw technique. Figure 34 shows a basic set up of the Van der Pauw measurement. Once the two resistance values

R_A and R_B are measured, then the film resistance R_S is calculated numerically solving the following equation:

$$\exp(-\pi R_A/R_s) + \exp(-\pi R_B/R_s) = 1 \qquad (14)$$

Resistivity is given by multiplying R_s with the thickness of the film.
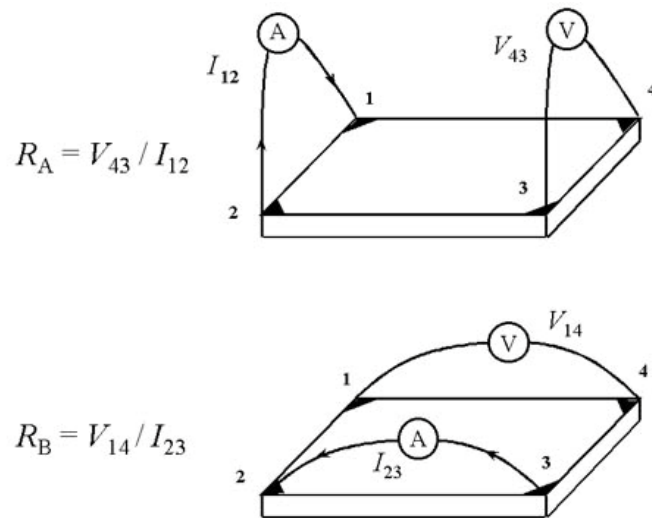
Fig. 34 A basic set up of the Van der Pauw measurement.

II.4. Mechanical properties: Nanoindentation

II.4.1. Definition of hardness

Hardness is one of important mechanical properties of material and indicates a material's resistance to localized plastic deformation or to permanent penetration by another hard material. Hardness can be measured by performing carefully designed laboratory experiments that replicate as close as possible the service conditions [26]. Measuring hardness involves two steps. First, a small and hard indenter is pressed into the material with a load F and the displacement has both elastic and plastic components.

However, when the indenter is retracted, the elastic deformation is recovered and only the residual area is measured [79]. Figure 35 shows the schematic diagram of the cross section of an indentation [80]. The hardness is defined by

$$H = P/A \tag{15}$$

where H is hardness, P is load and A is residual area. Based on the hardness definition, quantitative hardness measurement techniques have been developed over the years and they include Rockwell, Brinell, Vickers and Knoop hardness tests [81]. These conventional methods satisfy the need of hardness measurement for the bulk materials with larger dimensions. However, the load and indenter size limit the applications in small scale materials such as thin films, and nanowires. Micro-scale or nano-scale materials are often subjected to extreme conditions and their hardnesses are different from that of the bulk materials due to dimension constraints. So a novel approach to measure hardness of micro- or nano-scale materials is desirable. Nanoindentation technique combined with high resolution record of indentation depth and load and corresponding data analyses was developed to perform the hardness measurement of small structures [79].
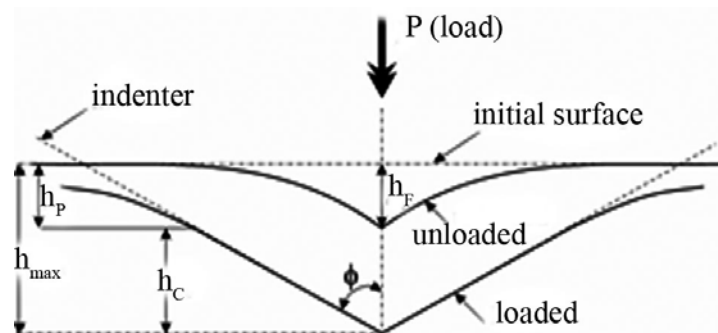
Fig. 35 Schematic representation of the cross sectional indentation [80].

II.4.2. Determination of indentation hardness

The nanoindentation instrument must have the capability of applying and recording the predetermined load and displacement with very high resolution during indentation, and use powerful computational method to perform the indentation load displacement analysis and obtain the mechanical properties directly from the load-displacement data.

The hardness of materials measured by nanoindentation is referred as indentation hardness (*HIT*) and it is determined by:

$$HIT = F_{max}/A_C \tag{16}$$

where F_{max} is the maximum applied force and A_c is the projected cross-sectional area of the contact between the indenter and the test piece. A_c can not be measured directly, it is determined from load-displacement curve. It depends on the shape of the indenter tip, and penetration depth. Hence, A_c is expressed as a mathematic function relating to the depth of contact of the indenter with the test piece ($A_c = f(h_c)$) [82].

The indentation hardness measurement process is similar to the conventional techniques. Hardness values are directly obtained from the load-displacement curve, but they are sensitive to the details of the analysis. Data analysis methods include elastic contact model [83-85], continuous stiffness method [86], Herzian contact solution for spherical indenters [87, 88]. Among these, the analysis based on elastic contact model developed and refined by Oliver and Pharr in 1992 [85] is the most commonly used nanoindentation analysis method. The method is used to determine the indentation hardness of thin films. There are several assumptions: (1) deformation upon unloading is

purely elastic; (2) the compliances of the samples and of the indenter tip can be combined as springs in series and (3) the contact can be modeled using an analytical model for contact between a rigid indenter of defined shape with a homogeneous isotropic elastic half space using equation:

$$S = \frac{2 E_r \sqrt{A_c}}{\sqrt{\pi}}$$ (17)

where S is the contact stiffness, A_C is the contact area, and E_r is reduced modulus [85].

Based on these assumptions, contact depth h_c can be expressed by

$$h_c = h_{max} - \varepsilon(h_{max} - h_i)$$ (18)

where h_{max} is the maximum depth and h_i, the intercept depth, is the intercept of the tangent to the load-displacement data at the maximum load on unloading with the depth axis [85]. The correction factor ε, a function of the shape of the indenter tip, for different indenter geometries is shown in Table 4 [82].

Table 4 Correction factor for different indenter geometries [82].

Indenter Geometry	ε
Flat punch	1
Conical	$2(\pi-2)/\pi=0.73$
Berkovich, Vickers	3/4
Paraboloid of revolution (includes spherical)	3/4

The procedure for data analysis to obtain indentation hardness is as follows: The slope of the fit at F_{max} is used to obtain h_i, and h_{max} at F_{max} is acquired in load-

displacement curve shown in Figure 36 [89]. Correction factor ε is determined by the shape of indenter tip. So the contact depth h_c can be obtained by inputting h_{max}, h_i and ε according to equation (4). The project area A_c is a function of shape of indenter tip. For a Vickers indenter, a pyramid shape indenter with a square base, $A_c = 24.5 \times h_c^2$ and for a perfect Berkovich indenter, a diamond pyramid with triangular base, $A_c = 23.96 \times h_c^2$ [82]. The obtained h_c is inputted into the area function to get A_c. Finally the indentation hardness can be obtained according to equation (2).
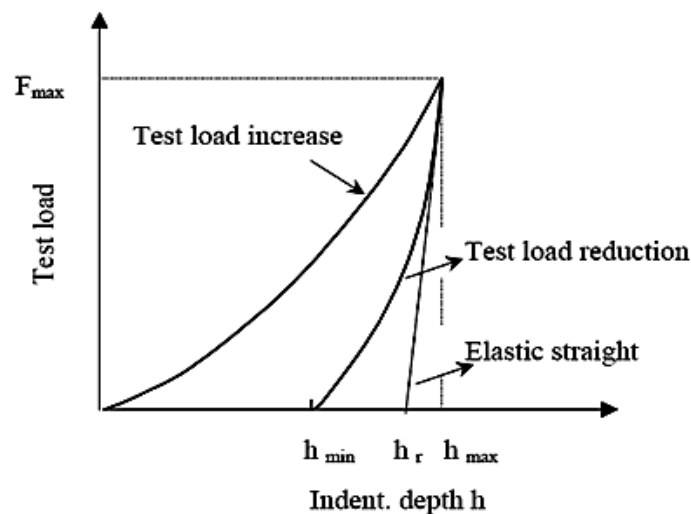
Fig. 36 Schematic diagram of cross section of indention, where h_{max} is maximum displacement, h_f is final depth and h_i is the intercept displacement [89].

II.4.3. Determination of indentation modulus

The elastic contact model assumes that the compliances of the samples and of the indenter tip can be combined as springs in series:

$$\frac{1}{E_r} = (\frac{1-v_{indenter}^{2}}{E_{indenter}}) + (\frac{1-v_{IT}^{2}}{E_{IT}}) \qquad (19)$$

where E_r is reduced modulus, $E_{indenter}$ is the modulus of indenter and E_{IT} is modulus of the tested materials. $v_{indenter}$ and v_{IT} are the Poisson's ratio of the indenter and the tested materials, respectively. In the contact model, the contact stiffness describes the slope of the tangent of load-displacement curve during unloading cycle and can be expressed by Eq. (17) [85]. So reduced modulus is obtained by a rearrangement of eq. (17):

$$E_r = \frac{S\sqrt{\pi}}{2\sqrt{A_c}} \qquad (20)$$

E_{IT}, modulus of the tested materials can be expressed by re-arranging Eq. 19:

$$E_{IT} = (1-V_{IT}^{2})/(\frac{1}{E_r} - (\frac{1-v_{indenter}^{2}}{E_{indenter}})) \qquad (21)$$

E_r can be obtained from equation (20) once the contact stiffness, the slope of the tangent, is acquired from loading-unloading curves. So, combining equations (20) and (21), E_{IT} can be obtained:

$$E_{IT} = (1-V_{IT}^{2})/(\frac{2\sqrt{A_c}}{S\sqrt{\pi}} - (\frac{1-v_{indenter}^{2}}{E_{indenter}})) \qquad (22)$$

Accurate quantitative measurements of indentation hardness and modulus may be obtained by the nanoindentation measurements. However, results from this technique are

affected by many factors such as tip geometry, machine compliance, time-dependent displacements, surface roughness, indentation size, etc [90-94].

II.4.4. Measurement of thin film hardness

The hardness measurements in this study were performed by both a Hystiron Triboscope and a Fischerscope HM2000XYp measurement system, which measures the indentation hardness according to ISO 14577. The hardness is determined from the area of the indenter displacement under load. The indentation depth and a constant, specific to each indenter, are used to calculate the area of the indenter displacement. The positioning devices consist of the holding device for the measuring head and a microscope with an attached video camera for viewing the test area in a video image. A Berkowich tip was used in Hysitron whereas a Vickers indenter tip was used in Fischerscope HM2000. The load range is from 0.4 to 2000 mN. The hardness and indentation modulus of Cu thin films were measured based on an average of 9-25 indents at different indentation depths at room temperature with the same loading rate. The maximum indentation depth was kept at ~ 200 nm for all specimens. The low surface roughness of the thin film (a few nm) leads to a negligible roughness effect. The total thicknesses of the films are ~ 2 μm, so the maximum depth is kept below 200 nm, which satisfies the one-tenth of film thickness "rule of thumb" to eliminate the substrate effect [87].

CHAPTER III

THERMAL STABILITY OF SPUTTERED CU FILMS WITH NANOSCALE GROWTH TWINS[*]

III.1. Overview

This work summarizes the investigation of the thermal stability of sputter-deposited Cu films with high density of nanoscale growth twins by using high-vacuum annealing up to 800 °C for 1 hour. Experiments show that average twin lamellae thickness increased gradually from approximately 5 nm for as-deposited films to slightly less than 20 nm after annealing at 800 °C. The average columnar grain size, on the other hand, increased rapidly from approximately 50 nm for as-deposited to 500 nm for Cu annealed at 800 °C. In spite of an order of magnitude increase in grain size, the annealed films retained a high hardness of 2.2 GPa, reduced from 3.5 GPa in the as-deposited state. The high hardness of the annealed films is interpreted in terms of the thermally stable nanotwinned structures. This study shows that nanostructures with a layered arrangement of low-angle coherent twin boundaries may exhibit better thermal stability than nanocrystals with high-angle grain boundaries.

---

[*] Part of the data reported in this chapter is reprinted with permission from "Thermal Stability of Sputtered Cu Foils with Nanotwins" O. Anderoglu, A. Misra, H. Wang, and X. Zhang, 2008. *Journal of Applied Physics* 103, 094322-1 - 094322-6, Copyright © 2008 by American Institute of Physics.

III.2. Introduction

Recent experimental work and molecular dynamic simulations show that mechanical strength of metallic materials can be significantly increased via grain size refinement down to nanoscale [27, 28, 30, 95-97]. Using molecular dynamics (MD) simulations with 100 million atoms to simulate plastic deformation of nanocrystalline copper, it was shown that by varying the grain size between 5 and 50 nanometers, the strength exhibit a maximum at a grain size of 10 to 15 nanometers. This maximum was attributed to a shift in the microscopic deformation mechanism from dislocation-mediated plasticity in the coarse-grained material to grain boundary sliding in the nanocrystalline region [28]. In an earlier study on Cu and Ni with average grain sizes in the range of 3–12 nm, authors reported a change in deformation mechanism. While at the smallest grain sizes all deformation is accommodated in the grain boundaries, at higher grain sizes intragrain deformation is observed. Analysis of the atomic configurations shows that intrinsic stacking faults are produced by motion of Shockley partial dislocations generated and absorbed in opposite grain boundaries. In Cu the stacking faults are observed at a grain size of 8 nm [7]. On the other hand experimental results showed that for pure Cu with grain sizes as small as 10 nm, hardness still follows the classical H–P relation, and that the rate sensitivity value is one order of magnitude higher than that for CG-Cu. The flow stress activation volume for nc Cu with $d = 10$ nm was found to be about $8b^3$. This was proposed as experimental evidence indicating that GB diffusion related activities are enhanced with grain refinement in the nanometer scale, but are not yet a dominating mechanism in plastic deformation of nc Cu with d

values as small as 10 nm [95]. The authors proposed that since plastic deformation in nc materials is more strain rate sensitive compared to CG counterparts the discrepancy between experimental results and atomistic simulations could stem from the fact that the atomistic simulations were performed at extremely high strain rates ($>10^7$ s^{-1}), several orders of magnitude higher than that experimentally accessible. As an alternative way to grain refinement, it was also shown that certain nanoscale multilayer films have shown unusually high hardness [98-101]. In nanocrystalline (nc) metals and nanoscale multilayer films, dislocation activities (nucleation and transmission) are significantly suppressed via either grain boundaries or layer interfaces. Recently another approach has been used to strengthen metals. Face-centered-cubic (fcc) metals and alloys such as Cu and austenitic stainless steel 330 with twin thickness on the order of 10-100 nm have shown very high mechanical strengths [15, 102, 103. It was demonstrated via atomistic modeling that twin boundaries are effective barriers to transmission of dislocations, similar to high-angle grain boundaries [67, 95, 104, 105] and nanometer-spaced twin boundaries can significantly increase mechanical strength. A model based on thermodynamics and kinetics of physical vapor deposition was developed to understand the formation of nanoscale growth twins [15, 75, 106].

The applications of high-strength nanocrystalline metals at high temperatures are very challenging, because in general high purity nanocrystalline monolithic metals have low thermal stability at elevated temperatures. It is known that grain growth occurs in nanocrystalline Cu even at room temperature [107]. Kobiyama and co-workers studied the thermal stability of nc Cu with different fiber textures and grain sizes [108]. The nc

Cu sample with <111> fiber texture and an average grain size of 30 nm showed a drastic

drop in hardness from 2.5 to 1.2 GPa after annealing at 400 °C. Moreover, for the same

annealing condition, the hardness of Cu with a weak texture dropped to about 0.6 GPa,

similar to the hardness of coarse grained (cg) Cu
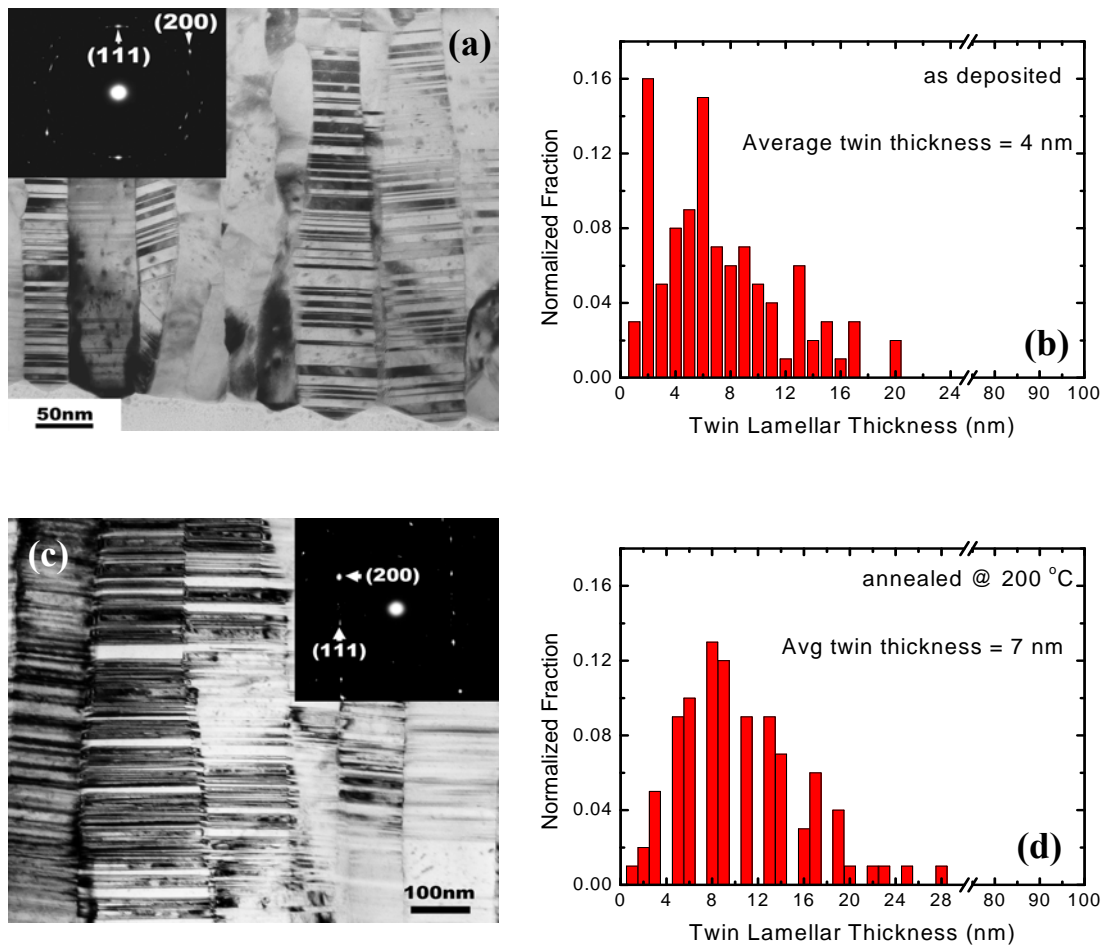
Fig. 37 Cross sectional TEM micrographs of polycrystalline Cu films and plots of statistical distribution of twins respectively: **(a)** and **(b)** as deposited; vacuum annealed for 1 hour at 200 °C **(c)** and **(d)**, 400 °C **(e)** and **(f)**, 600 °C **(g)** and **(h)**, 800 °C **(i)** and **(j)** [112].
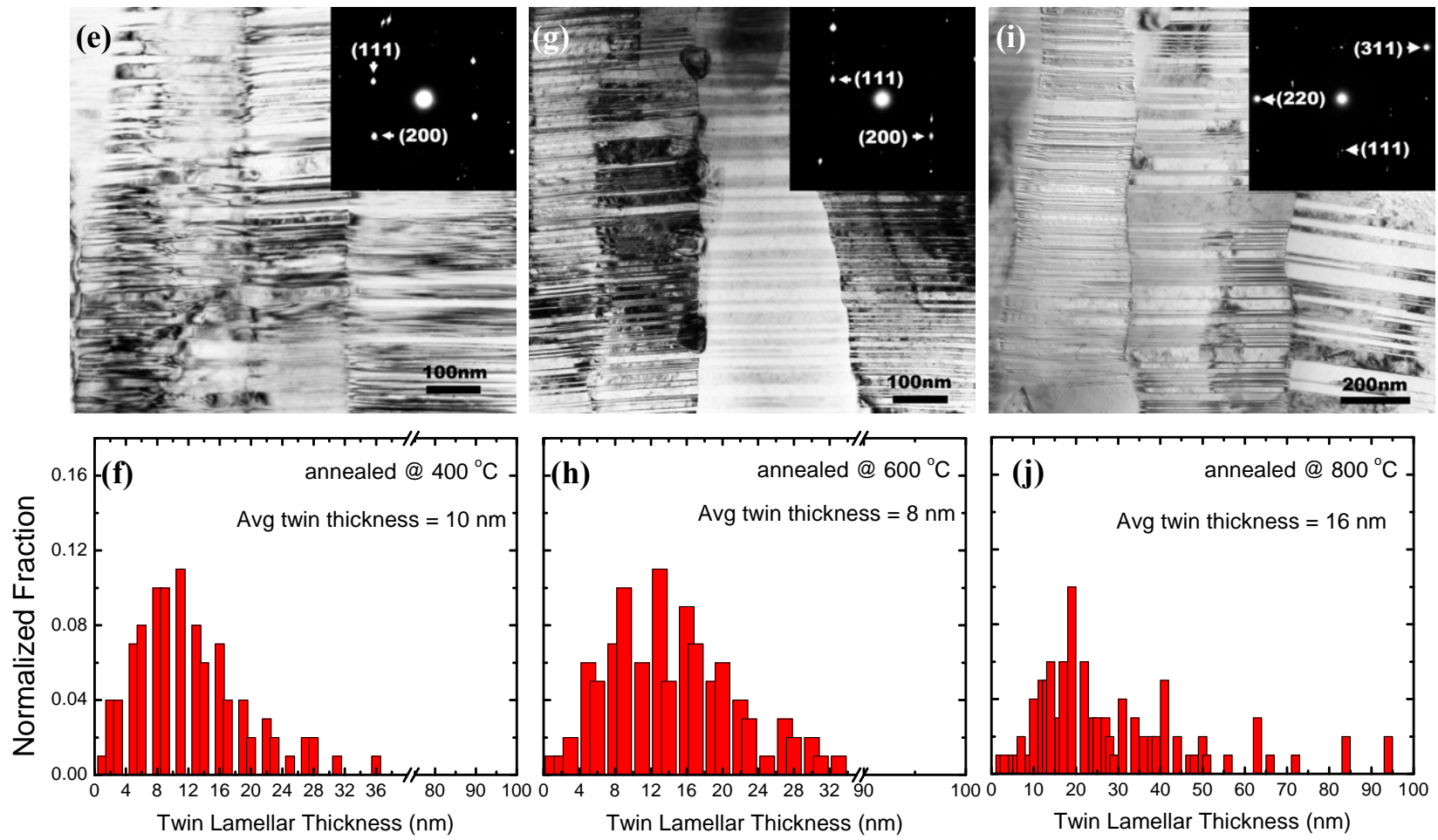
Fig. 37 Continued.

In another study on ultra-fine grained (UFG) Cu, it was shown that grains enlarged by an order of magnitude after annealing at 200 °C [109]. Oh-ishi and coworkers showed that the average grain size of torsion strained UFG Cu increased from 170 nm to an order of magnitude higher as a result of annealing at 300 °C with a subsequent decrease in hardness [110]. In severe plastically deformed (SPD) Cu and Ni, initial grain sizes of approximately 100 nm increased up to an order of magnitude after annealing at about 250 and 300 °C, respectively [111]. In addition, the hardness of the SPD Cu starts at around 1.7 GPa and reduces to 0.85 GPa after annealing at 400 °C. It should also be noted that the studies on nc Cu and Au showed that the samples with smaller grain sizes and strong textures have better thermal stability compared to samples with larger grains and weak textures [108, 113].

Despite the high mechanical strength of nanotwinned Cu films, their thermal stability at elevated temperatures remains to be evaluated. In an earlier work, we showed that nano-twins in sputter-deposited 330 SS films have considerable thermal stability; average twin spacing and orientation of twin interfaces remain unchanged after annealing up to 500 °C [114]. In this study, we show that nanoscale growth twins in Cu films are indeed much more stable than high angle grain boundaries in nc and UFG Cu. The retention of high mechanical strength in Cu after annealing at 800 °C is a result of the thermal stability of twin boundaries at elevated temperatures. The coarsening kinetics of columnar grains and twin lamellae is discussed in terms of their relative energies.

III.3. Results

III.3.1. Microstructural characterization

The microstructures of the as-deposited and annealed Cu films at temperatures from 200°C to 800°C were characterized using TEM and HRTEM as shown in Figure 37. As-deposited Cu thin films exhibit a <111> fiber texture along the growth direction and have an average columnar grain size of 43 nm, as shown in Figure 37a, with a high-density of growth twins oriented parallel to the substrate surface. Since the columnar grains get divided into a layered arrangement of matrix and twins, we use an average lamellae thickness to represent the length scale of nano-twins. The nanoscale growth twins are retained in all annealed specimens with noticeable increase of columnar grain sizes (Figure 37 c, d, f, and h). Some planar faults were identified to be stacking faults. The statistical measurements of lamellae thickness distributions for as-deposited and annealed Cu specimens (200, 400, 600, and 800°C) are shown in Figure 37 (b, d, f, h, and j). Careful examination reveals that annealing leads to a modest increase as well as a broader distribution in the average lamellae thickness. The variations of average lamellae thickness and columnar grain size as a function of annealing temperature are plotted in Figure 38a. The average columnar grain size has increased by an order of magnitude, from 43 nm for as-deposited Cu to over 500 nm for Cu films annealed at 800°C. Figure 38b shows that the average lamellae thickness has increased from 4 nm to approximately 16 nm after annealing.

HRTEM micrograph reveals the details of twin interface and columnar grain boundaries in Cu films annealed at 400°C. The inset in Figure 39a is magnified in

Figure 39b to show the twin lamella in adjacent columnar grains and the formation of facets along the columnar grain boundaries. The two columnar grains have a low angle grain boundary, approximately 9° as shown by fast Fourier fast transform of the image in Figure 39b.
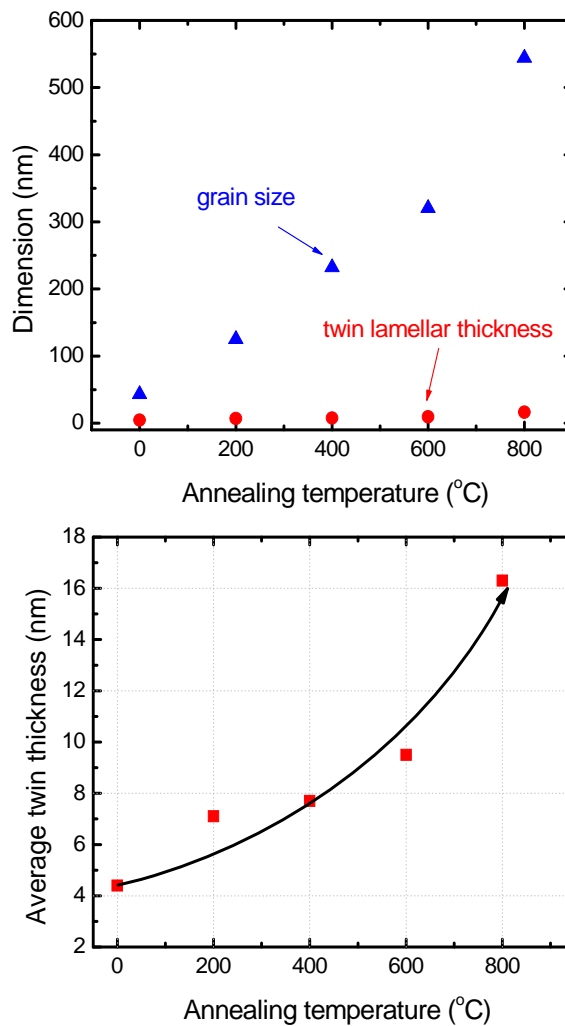
Fig. 38 (a) Evolution of twin lamellar thickness and grain size as a function of annealing temperature. Grains grow at a much higher rate than twins in vertical direction [112]. **(b)** Twin evolution in vertical direction a function of annealing temperature. The cross sectional TEM images show that twins accompany grains in lateral dimension.
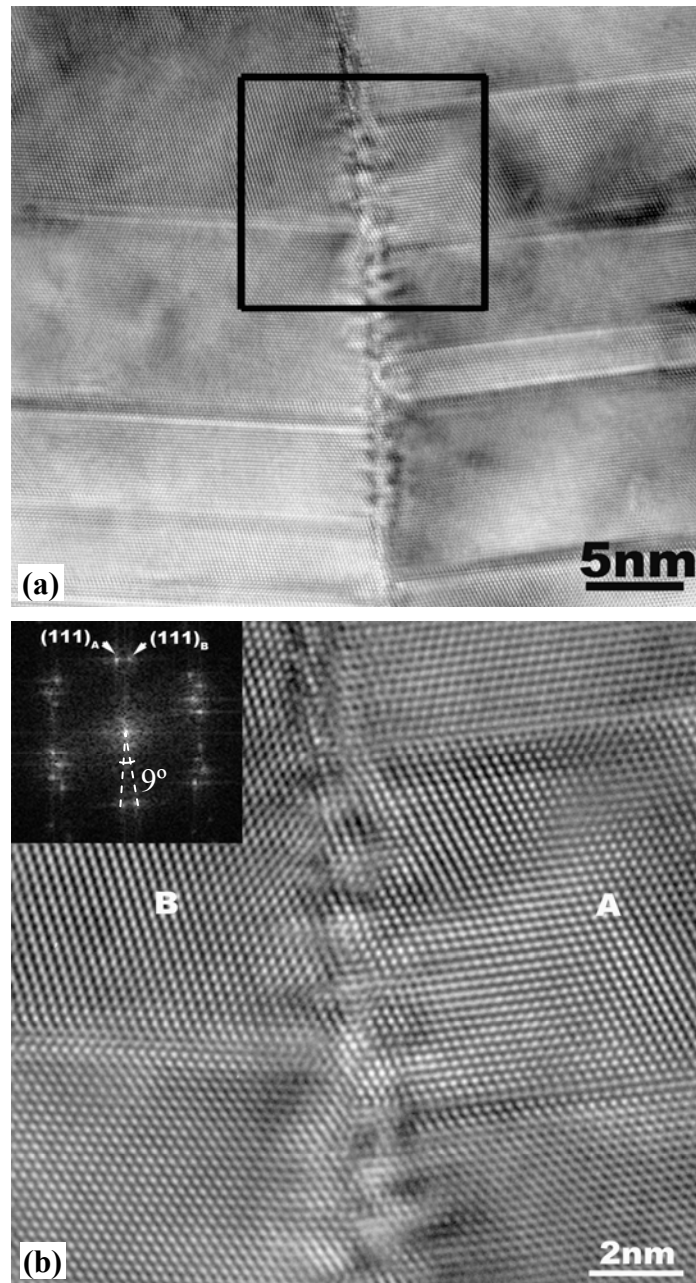
Fig. 39 (a) HRTEM micrograph reveals the details of twin interface (horizontal boundary) and columnar grain boundaries (vertical boundary) in Cu films annealed at 400°C. **(b)** The region in black square in (a) is magnified and shows twin lamella in adjacent columnar grains. The two columnar grains have a low angle grain boundary, approximately 9° as shown by fast Fourier transform of the image [112].

III.3.2. Hardness

The hardness of as deposited Cu thin films decreased gradually and continuously from ~ 3.5 GPa, with increasing annealing temperature to approximately 2.2 GPa after annealing at 800°C as shown in Figure 40. In comparison, hardness of Cu with grain sizes of submicron or greater decreases rapidly to ~1 GPa or below at annealing temperatures of 400 °C or lower [108,109, 113]. In all cases, the hardness of Cu thin films are about an order of magnitude higher than that of bulk Cu which is about 0.6 GPa at room temperature indicated by the dashed line in Figure 41.
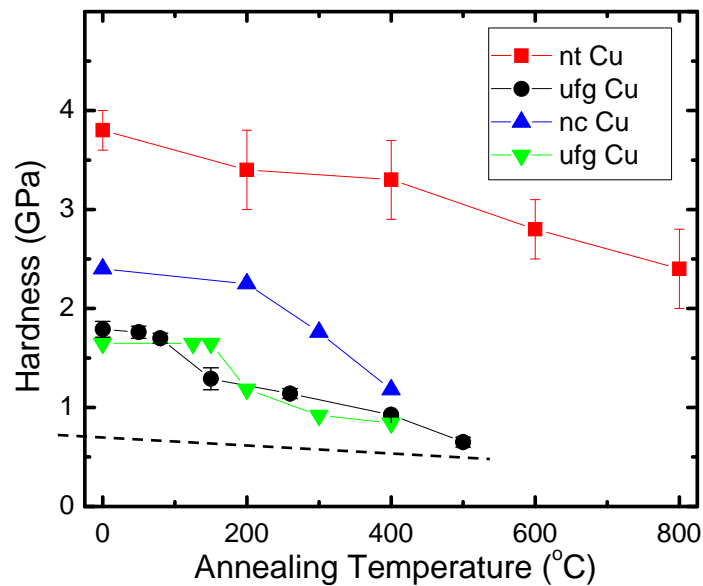
Fig. 40 Indentation hardness of nanotwinned Cu films as a function of annealing temperature. The literature data for ultra fine grained (UFG) and nanocrystalline (nc) Cu are also included in the plot for comparison [112].
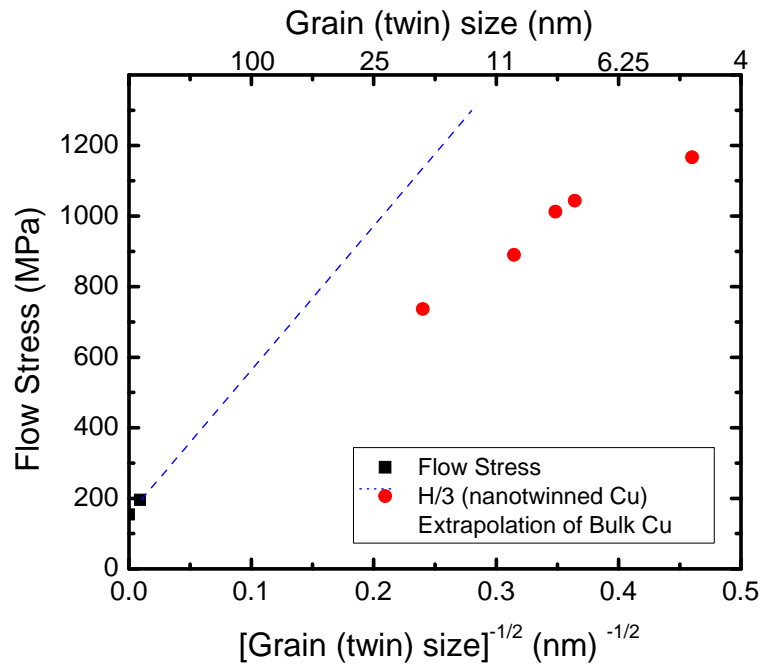
Fig. 41 Plot of flow stress vs. $l^{1/2}(t^{1/2})$ where l is average grain size, or average twin lamellae thickness (t). The data for coarse grained (cg) Cu from literature also included in the plot for comparison. The dashed line is the extrapolation of cg Cu [112].

A Hall-Petch plot of the hardness as a function of $t^{-1/2}$ (where t stands for the average lamellae thickness that varied from $\approx$ 4 nm for as-deposited to $\approx$16 nm for 800°C annealed samples) is given in Figure 41. For comparison, flow stress data, corresponding to approximately 10% strain, from annealed cg Cu are also shown in the same plot [115]. The Hall-Petch slope (k) of the cg Cu is approximately 0.15 MPa.m$^{1/2}$ and its extrapolation to the nanometer range overestimates the flow stresses of nanotwinned Cu. A linear fit through the data for nanotwinned Cu gives a slope of $\approx$0.06 MPa.m$^{1/2}$ that is two times lower than the k for bulk Cu. This indicates that the weak dependence of flow stress of nanotwinned Cu on lamellae thickness (in the range

of 4 to 16 nm investigated here) cannot be explained via an extrapolation of the continuum dislocation pile-up based Hall-Petch model.
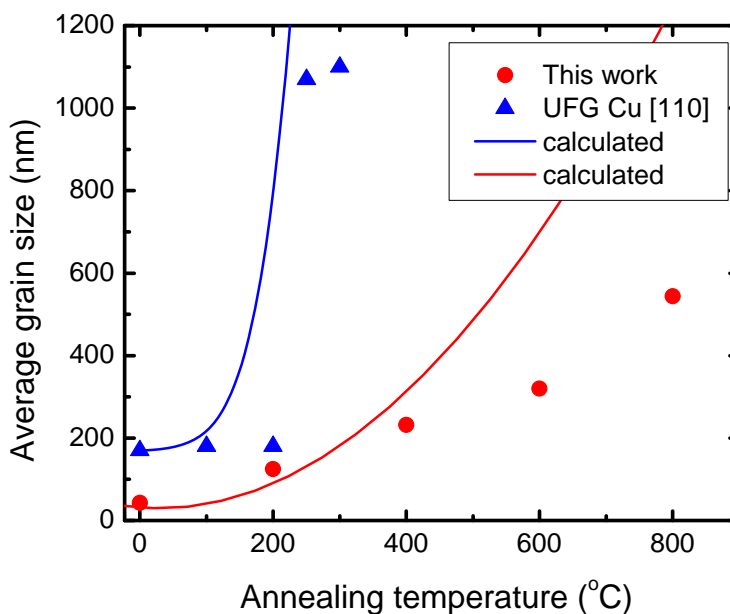
Fig. 42 Grain growth as a function of annealing temperature. For comparison literature data for UFG Cu film is also included. The solid lines are plotted based on normal grain growth equation (Equation 1) [112].

III.4. Discussion

III.4.1. Thermal stability of nanoscale growth twins

The nanoscale growth twins in Cu films show remarkable thermal stability. Even at temperatures as high as 800 °C (0.74T$_m$), (where T_m is the melting point of Cu ~1083 °C) no significant coarsening of the nanoscale twinned structure in the vertical dimension was discerned from TEM studies. The average columnar grain sizes however, increased rapidly by over an order of magnitude, from 43 nm to around 544 nm, in lateral dimension. Grain growth in nc or UFG Cu normally starts at around 150-300 °C

[111, 113, 116]. Compared to some annealing studies available in the literature for UFG pure Cu, grain growth in this study seems to be a lot less [110, 111]. Figure 42 exhibits the effect of annealing on the grain growth of nanotwinned Cu together with data on UFG Cu [110]. The curves are plotted using the normal grain growth equation:

$$D^n - D_0^n = K_0 t \exp(-Q/RT) \tag{23}$$

where D_0 is the initial average grain size, D is the average grain size after a time t, n is the grain growth exponent, K_0 is a constant [117], Q is the activation energy for grain growth, R is the gas constant and T is the annealing temperature. Q for normal grain growth in pure, bulk copper was experimentally determined to be 83 kJ/mol [118]. The exponent n usually varies from 2 to 4 [118-120]. As shown in Figure 42, for UFG Cu, n = 2.5 seems to fit the data well [119]. However, for nanotwinned Cu, even n = 4 over estimates the experimentally measured grain growth. Thus, the coarsening of the columnar grains from 43 nm (as-deposited) to around 544 nm (800 °C anneal) is too sluggish compared to normal grain growth in pure ultra-fine grain Cu.

Several factors may play a role in enhancing the thermal stability of columnar grains in nanotwinned Cu. First, in the current study, as-deposited Cu films have columnar grains with ~ 40 nm in diameter, but tens of microns in height. The magnitude of grain boundary energy stored in these columnar grains will be much less than that stored in equiaxed grains with similar grain size. Second, faceted columnar grain boundaries are typically observed in annealed nanotwinned Cu, as shown in Figure 39. Facets may originate from the propagation of twin boundaries in lateral direction. The
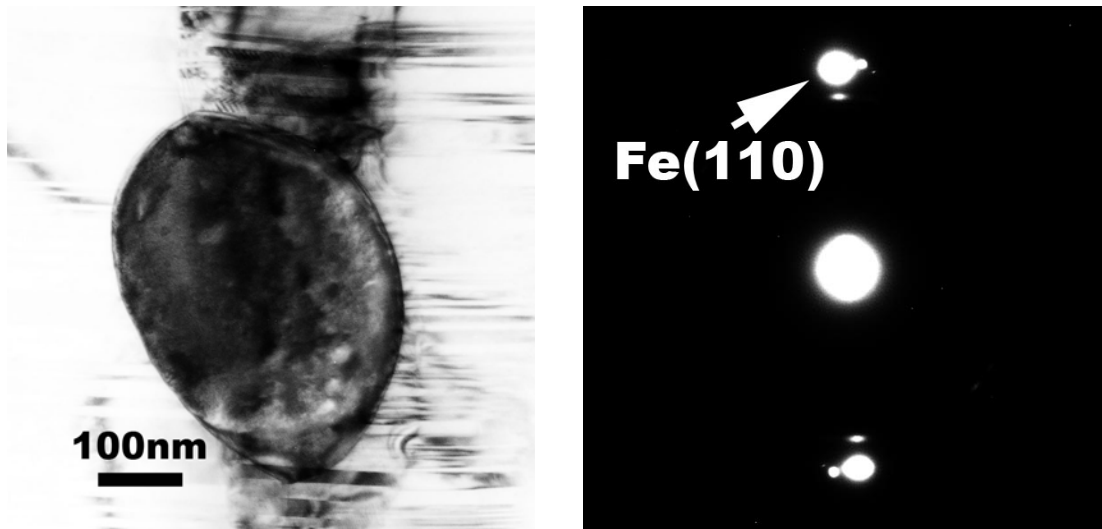
Fig. 43 (a) TEM shows that the precipitate in 800 C annealed film. **(b)** The micro-diffraction analysis on the precipitate shows that the precipitate is Fe.

formation of facets typically indicates a pinning effect on the migration of grain boundaries. Also, the twin boundaries grow laterally as the column boundaries migrate, thereby adding extra energy in the form of new twin boundaries that are created, that may also retard the grain growth in nanotwinned Cu. However, this may be a small effect since twin boundaries also get eliminated in the columnar grains that shrink. Third, it is known that precipitates exert a Zener drag force on the grain boundary migration [121]. High temperature annealing show Fe precipitates at the grain boundaries ($\sim$ 0.5at% Fe) as shown in Figure 43. But these precipitates do not appear in the as deposited film which suggests that such small amount of Fe probably exists in the form of solid solution and precipitates upon elevated temperature annealing. Sputtering is a non-equilibrium process and has been show to increase solid solubility in certain systems. Fe, in the form of solid solution in Cu may segregate to grain boundaries and

retard grain growth [121, 122]. Temperature dependent resistivity measurements also show the existence of magnetic impurity. What is known as Kondo effect is seen in Figure 44. A resistivity minimum is reached around 30 K. MD simulation shows that presence of 1 % Fe in Cu could cause an order of magnitude increase in barrier strength for grain boundary migration [123]. Finally, nanotwinned Cu has a strong <111> texture. It is known that a strong texture results in relatively smaller misorientation between the grains and therefore reduces the driving force for grain growth [124].
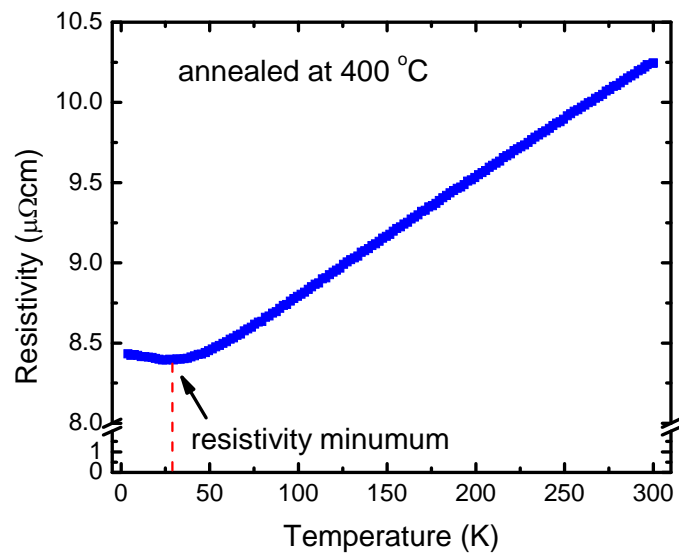
Fig. 44 Temperature dependent resistivity measurements indicate existence of magnetic impurity in Cu. A resistivity minimum is reached around 30 K which is known as Kondo effect.

The unusually high temperature thermal stability of nanoscale twin lamellae could be interpreted from thermodynamics point of view. The energy of a high angle grain boundary in Cu is typically 625-710 mJ /m^2, [125, 126] whereas the twin boundary

energy of Cu is much smaller, typically 24-39 mJ /m^2 [126, 127]. The ratio of the energy of a coherent twin boundary to a high-angle grain boundary (γ_{TB}/γ_{GB}) in Cu is about 0.034 [127]. For instance, if we assume a surface area of 1 m^2, the total grain boundary energy stored within 1 μm thick films is around 27 J, whereas the total twin boundary energy stored is approximately 5 J. The driving force for reducing the total energy of the system via grain coarsening is obviously higher than that of twin coarsening. After annealing at 800 °C, the total energy stored at column grain boundaries, with an average diameter of 500 nm, is approximately 2.5 J, similar to the energy stored in twin boundaries, 1.25 J, with an average twin spacing of ≈ 20 nm. If we use equation (1) with $n = 4$ and an annealing time of 1 hour at 800 °C, the activation energy for twin boundary migration for an observed coarsening from 4 to 16 nm, is calculated as 238 kJ/mol. This is almost a factor of three higher than the activation energy (83 kJ/mol) for high-angle grain boundary migration in pure Cu, consistent with the fact that the driving force for twin boundary migration is lower due to its lower energy.

III.4.2. Hardening from nanoscale growth twins

First we will examine the influence of twin thickness on hardness of Cu films. The average columnar grain size is over 500 nm for Cu films annealed at 800 °C. From Hall-Petch plot for cg Cu (hardness vs. grain size), grain size of 500 nm will lead to a hardness of ~1.1 GPa, much lower than our experimental value, 2.2 GPa. As twin thickness is always an order of magnitude smaller than grain sizes, it is obvious that the strength of Cu films is mostly due to confinement of dislocation movement by twin

boundaries. With increasing twin thickness, the hardness of nanotwinned Cu decreases gradually. In this case, the smallest dimension that is the twin lamellae thickness plays a dominant role in controlling film hardness.

Although the traditional H-P relation seems to hold down to 10 nm for nc Cu films, and 16 nm for powder consolidated nc Cu [27, 96], the hardness values of nanotwinned Cu does not follow H–P relation even at the highest lamellae thickness of 16 nm as shown in the Fig 6. The reason why the continuum pile up is not applicable in the nanotwinned Cu case will be explained next. It should also be mentioned that no softening was observed in nanotwinned Cu even at the smallest length scale, whereas MD simulations show that softening appears at about 10–15 nm in nc-Cu [29]. Nieh and Wadsworth [128] proposed the following relation to compute the equilibrium distance between two edge dislocations:

$$l_C = \frac{3Gb}{\pi(1-\upsilon)H} \tag{24}$$

where,

l_C : The equilibrium distance between two edge dislocations
G : Shear modulus, ~ 48 GPa
b : Burgers vector, ~ 0.256 nm
υ : Poisson's ratio, ~ 0.34
H : Hardness

The model is based on the fact that if l_C is greater than average grain size, then there will be no dislocation pile-ups and the H-P relation would not apply. If the grain size is larger than l_C then the H-P relation stands. Such model has been applied to several materials

with reasonable agreement [128]. Based on this model (instead of grain size, twin thickness is used) the critical distance between two edge dislocations is 5, 7 and 8 nm for the nanotwinned Cu samples with average twin thickness values of 4, 10, and 16 nm respectively indicating that the dislocation pile is not possible in any twin lamellar. A similar trend was observed in nanotwinned austenitic stainless steel [67]. Therefore at such small twin spacing, resistance for transmission of a single dislocation across twin interface determines the strength of materials [129-131]. MD simulations of slip transmission across twin boundaries in fcc metals have shown twins to be very strong barriers of slip [67, 132, 133]. Since the characteristic barrier stress for slip transmission across twin boundaries is independent of twin lamellae thickness, the weak dependence of strength on average lamellae thickness may result from the broad distribution in the lamellae thickness that gets broader in annealed samples.

III.5. Summary

Sputter-deposited Cu thin films with high-density nanoscale growth twins have shown remarkable thermal stability after annealing at 800º C ($0.74T_M$). The driving force for twin growth is much lower than that for grain coarsening because twin boundary energy is an order of magnitude lower than grain boundary energy. Such high thermal stability of nanotwins lead to the retention of hardness of 2.2 GPa in annealed nanotwinned Cu. Low energy twin boundary may provide a unique way to achieve both high strength and high temperature thermal stability in certain metallic materials.

CHAPTER IV

PLASTIC FLOW STABILITY OF NANOTWINNED CU FOILS[*]

IV.1. Overview

Sputter deposited, highly (111) textured, self-supporting nanotwinned Cu foils were rolled from 17% up to 50% thickness reduction at room temperature. Scanning electron microscopy (SEM) shows uniform reduction in the thickness. X-ray pole figure measurements indicate no significant out-of-plane rotation of the grains after even 50% reduction in the thickness. Statistical measurements from transmission electron microscopy (TEM) analysis indicate no significant change in the average twin lamellar thickness although the height of the columnar grains was reduced by a factor of two after rolling. High resolution transmission electron microscopy (HRTEM) experiments revealed that rolling induced high density dislocations at twin interfaces. Deformations enabled by twin interface-dislocation interactions and subsequent twin interface migrations normal to the interfaces. Molecular dynamic (MD) simulations suggest that plastic deformation is facilitated by the migration of twin boundaries vertically up or down. A model based on MD simulations and HRTEM observations explains the plastic deformation mechanism in the nanotwinned Cu foil. It was also found that rolling induces moderate increase in flow strength. A moderate work-hardening was observed in

---

[*] Reprinted with permission from "Plastic Flow Stability of Nanotwinned Cu Foils" O. Anderoglu, A. Misra, J. Wang, R. G. Hoagland, J. P. Hirth, and X. Zhang, 2009. *International Journal of Plasticity*, in press. Copyright © 2009 by Elsevier.

rolled nanotwinned Cu foils and is discussed based on the introduction of high density dislocations at twin interfaces.

IV.2. Introduction

Nanotwinned (nt) metals have been the subject of significant recent research due to novel mechanical and electrical properties that emerge as the average twin thickness is reduced nanometer scale [15, 69, 74]. The average twin thickness can be controlled by electro [133] or physical vapor deposition [49, 135]. The next chapter of this thesis deals with the controlled synthesis of nt Cu films via magnetron sputtering. The controlled synthesis is important because it allows one to tailor the microstructure to obtain the desired properties [69, 49]. In addition, in the previous chapter we showed that low energy and high symmetry associated with coherent twin boundaries provides stability at elevated temperatures [112]. Nt metals exhibit high strengths similar to their nanocrystalline (nc) counterparts. Experiments and simulations show that coherent twin boundaries (CTB) can inhibit dislocation motion like conventional grain boundaries (GBs) [64, 104, 105, 136]. However, unlike nc metals significant increase in strength does not cause a pronounced decrease in ductility in nt metals. This suggests that the plastic deformation mechanism takes place in nt metals must be different than that of nanocrystalline metals.

Recently, understanding the role of twin boundaries (TBs) in the plastic deformation process of metals has attracted significant attention from the scientific community [137-140]. Molecular Dynamic (MD) simulations suggest that plasticity is

dominated by twin boundary migration (TBM) or slip transmission thru TB and that the former mechanism depends on the twin boundary migration energy (generalized planar fault energy curves-GPF) and the latter depends on the stacking fault energy associated with the metal [139, 140, 141]. Froseth et al investigated the effect of grown-in twin boundaries on the plastic deformation mechanism in nc-Ni and Cu, and showed that (1) for these particular fcc metals TB migration is not the favored deformation mechanism and (2) that the Schmid factors of the grown-in twin plane play a correspondingly important role. The authors explained the results in terms of the different ratios of the extrema of the generalized planar fault curves [139]. In another simulation Jin et al. studied the interactions between screw dislocation and CTB for three fcc metals, Cu, Ni and Al and showed that depending on the material and the applied strain, a screw dislocation approaching the coherent twin boundary from one side may either propagate into the adjacent twin grain by cutting through the boundary or it may dissociate within the boundary plane. They reported that interaction modes depend on the material dependent energy barrier for the nucleation of Shockley partial dislocations [142]. Later on, same group completed the preliminary results by studying purely stress-driven interactions between 60° non-screw lattice dislocation and CTB. They found that depending on the material and the applied strain, slip interacted with the boundary in different ways: if a 60° dislocation is forced by an external stress into a CTB, it dissociated into different partial dislocations gliding into the twin as well as along the twin boundary. They also showed that a sessile dislocation lock may be generated at the CTB if the transited slip is incomplete and that the details of the interaction are

controlled by the material-dependent energy barriers for the formation of Shockley partial dislocations from the site where the lattice dislocation impinges upon the boundary [143]. Afanasyev et al investigated the role of growth twin boundaries on the slip activity of gold nanopillars under uniaxial compression by MD simulation and found a new type of size-dependent strengthening in twinned gold nanopillars [137]. The study showed that strengthening results from slip arrests in the form of Lomer-Cottrell locks at the intersection of partial dislocations and twin boundaries. In addition, the significance of such phenomenon was found to depend on the twin size. Cao et al. studied the plastic deformation of polycrystalline Cu with ultrathin lamella twins using MD simulations and showed that the abundance of twin boundaries provides obstacles to dislocation motion, which in consequence leads to a high strain hardening rate in the nanotwinned Cu [144]. They also showed that the twin lamellar spacing plays a vital role in controlling the strengthening effects such that the thinner the thickness of the twin lamella, the harder the material and that the twin boundaries can act as dislocation nucleation sites as they gradually lose coherency at large strain. Zheng et al investigated the tensile deformation of nc Cu with and without growth twins by large-scale MD Simulations and found that the twins can significantly enhance the material strength and that the high strength and superior ductility come not only from the effective decrease in grain size due to the presence of TBs, but also from the TB pinning effect and interface-mediated slip transfer reactions, including both the complete transmission of screw dislocations and the incomplete transmission of non-screw dislocations [145]. In the simulation jog was observed as result of the interactions between these transmitted dislocations. They

suggested that a sample of appropriate thickness should be used in MD simulations to understand the real deformation mechanisms of nc materials. Zhu et al developed a mechanistic framework for predicting the rate sensitivity and elucidating the origin of ductility in terms of the interactions of dislocations with interfaces and showed that slip transfer reactions mediated by twin boundary are the rate-controlling mechanisms of plastic flow using atomistic reaction pathway calculations [133]. The study attributed the relatively high ductility of nanotwinned copper to the hardening of twin boundaries as they gradually lose coherency during plastic deformation. Jaruselam et al. proposed a continuum description of the effective response of nt ufg crystals [146]. The model was based on a finite element formulation of the continuum three-dimensional problem describing the deformation of polycrystal grains explicitly and the contribution of the twins was considered through a homogenized representation of the twin planes in the crystal lattice in each grain. In this study, simulations of tensile tests captured the increased level of strength with increasing twin densities and also a study of the influence of crystallographic texture on the effective response was presented. The authors show that the model captured the three-dimensional features of the deformation of nanotwinned ultrafine crystals and provided a modeling framework for predicting the transition from intragrain to intergrain mechanisms of failure.

In addition to the MDs mentioned briefly above, there is also a good number of experimental works studying the deformation of nanotwins. Some of this work is presented briefly.

Field et al. observed in polycrystalline Cu deformed at room temperature that a fraction of the TBs in the material migrated during deformation and that in a few isolated instances narrow twin grains consisting of two parallel boundaries separated by a small distance were mechanically annihilated during this process [147, 148]. They proposed that this interface migration was due to the boundaries acting as non-regenerative sources for dislocations. In addition, the orientation gradient in a parent grain near an annihilated twin was analyzed for dislocation density and it was found that sufficient geometrically necessary dislocation content was present to be consistent with the proposed mechanism.

Lu et al. investigated the rate sensitivity of flow stress and the extent of strengthening in polycrystalline copper containing different volume fractions of nanotwins with the same average grain size and found that the loading rate sensitivity of UFG Cu with a high density of CTBs significantly higher than that of ufg Cu without twins and that with a decrease of CTB density, the hardness and the rate sensitivity also decrease [149]. Their post deformation TEM observations in ufc Cu with higher concentration of nanotwins indicated noticeable displacement and movement of CTBs, formation of steps and jogs along CTBs, and the generation of high dislocation density around CTBs, especially in the vicinity of stress concentrations. They proposed that these processes lead to a thermal activation volume during plastic flow which is three orders of magnitude smaller than that found for UFG fcc metals. The study also showed that the CTBs with a high density of defects and displaced CTBs serves as dislocation sources, very much like conventional GBs.

In situ TEM experiments present further evidence of TBs acting as dislocation sources by the formation of steps at the interface thru sessile Frank partials. Wang et al. revealed the real-time dynamic process of TB migration mediated by Shockley partial emission via in situ TEM for the first time and showed that this is the preferred deformation mechanism in the initial stage of plastic deformation in nt Cu, where the microstructure is dominated by the high-density GB/TB intersections and that the latter facilitate the nucleation of the emitting partials to travel on the atomic plane right next to the TBs [150]. The in situ experiments presented strong evidence of TBs acting as dislocation sources and detailed HRTEM analysis suggested that the existence of a TB step formed by a sessile Frank partial is beneficial to TB dislocation emission [151].

Previous experimental work on the deformation mechanism of nanotwinned Cu is based on foils that are electrodeposited. In general electrodeposited Cu has large grains oriented randomly with embedded nanotwins. In this article, we report on the plastic flow stability of highly textured nt Cu foils. We also studied the texture evolution in free standing nt polycrytalline Cu foils deformed by room temperature rolling and developed a plasticity model to explain the change in average twin size as a result of thickness reduction and hardness change.

IV.3. Results

IV.3.1. Microstructure

Cross-sectional SEM experiments show that all Cu foils deformed uniformly without the detection of any crack. A representative SEM micrograph of nt Cu foil

sandwiched between two Si substrates, as shown in Figure 45, reveals uniform thickness

reduction after 17 and 50% rolling strain. The images show no indication of cracks.
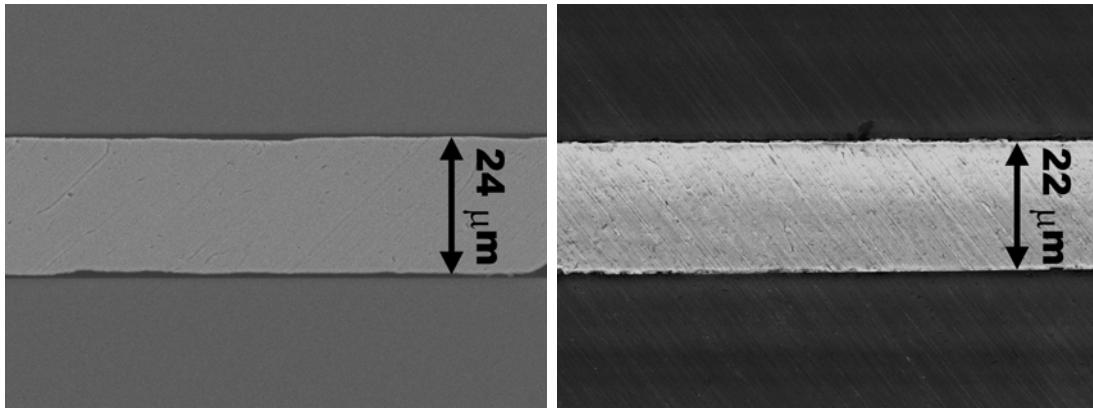
Fig. 45 Cross-sectional SEM images show uniform thickness reduction and no indications of cracks after rolling **(a)** 40% rolling reduction **(b)** 50% rolling reduction.
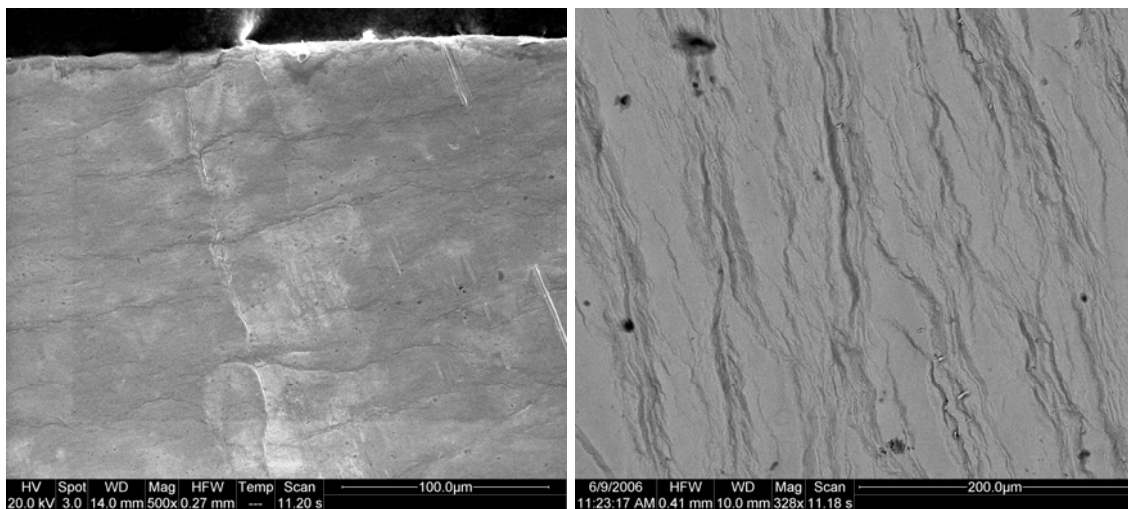
Fig. 46 Plan view SEM images show surface morphologies of the nanotwinned Cu foils after rolling. Shear bands perpendicular to rolling direction were observed regardless of the sandwich material used to roll the nanotwinned Cu foils: **(a)** 40% **(b)** 50% thickness reduction.

Plan view SEM images are shown in Figure 46. Rolling induces bands that are perpendicular to rolling direction as seen in the figures. The sandwich materials used to roll these foils were SS 330. Identical features were also seen on the SS 330 plates. Bright field TEM micrographs of the cross-section views are shown in Figure 47 for (a) as deposited and (b) 50% rolled Cu foils. Note that the nanotwins are still present in the 50% rolled Cu foil. In rolled Cu, the twin interfaces do not appear as sharp as before, and the contrast within twin lamella is complicated due to the presence of high density of dislocations. Comparisons of the inserted selected area diffraction (SAD) patterns show that <111> fiber texture is retained after the rolling strain of 50%. The normalized statistical distributions of the twin thicknesses before and after rolling are shown in Figure 47 (c-d). The average twin lamellae thickness (L_{avg}^{twin}) is obtained from numerous XTEM micrographs and calculated from the arithmetic average of the statistical thickness distributions of twin and matrix. After rolling, the L_{avg}^{twin} value increases only slightly from 5 to 7 nm after 50% thickness reduction. The change in the statistical distribution of twin spacing after rolling is shown in Figure 47e, which is obtained by subtracting normalized distribution in (d) from (e). It is clear that the number fraction of nanotwins with twin spacing of 1-2 nm decreases significantly, whereas that of thicker twins, with twin spacing of 5-8 nm increase more dramatically. Statistical distributions of columnar grain sizes, obtained from the XTEM studies are shown in Figure 48 a and b. The average columnar grain size increases from 43 nm in the as-received Cu foil to 124 nm after 50% rolling reduction.
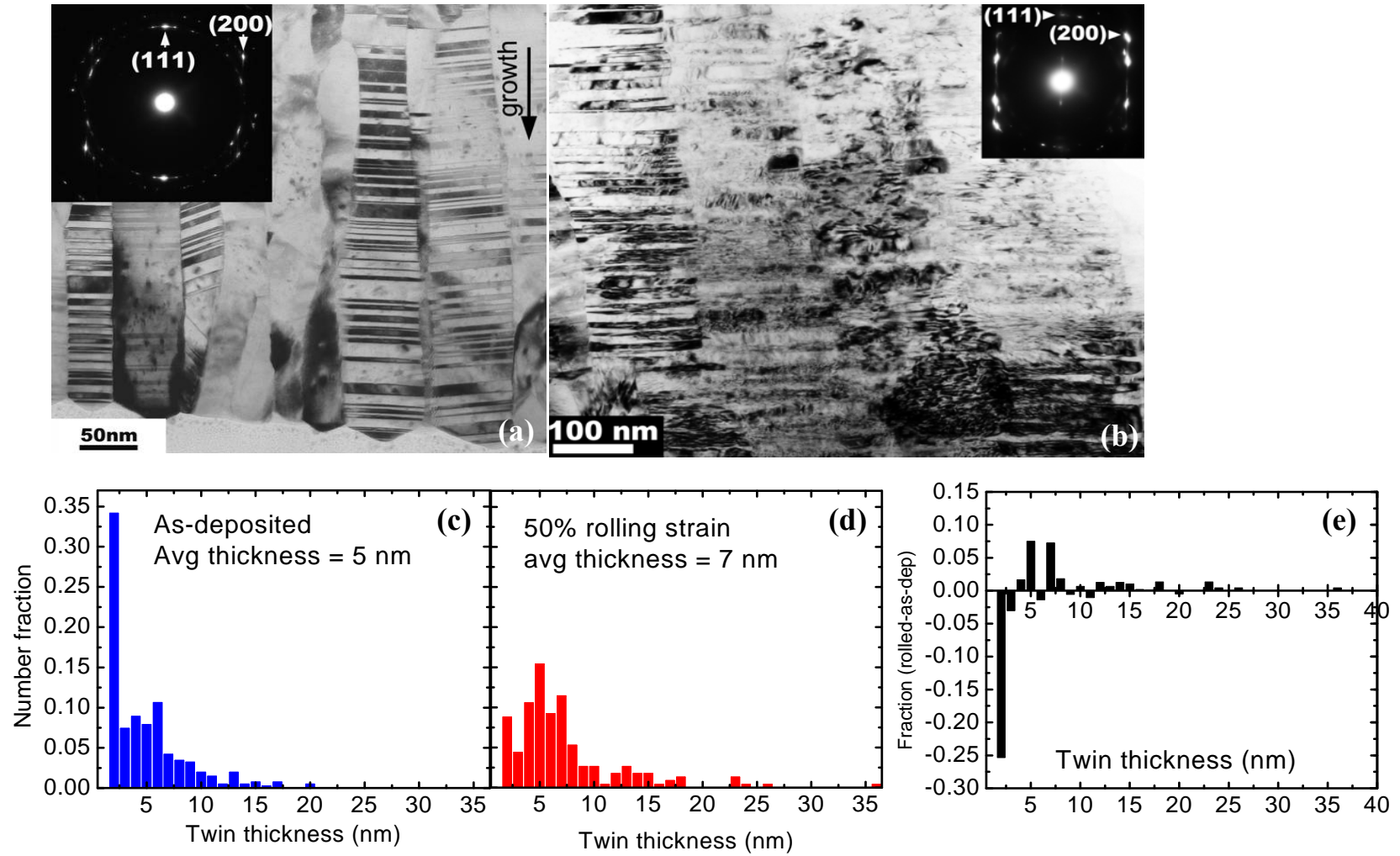
Fig. 47 Cross-sectional TEM images of nanotwinned Cu foil **(a)** as deposited **(b)** after 50% rolling reduction. Normalized statistical distributions of twins are shown in **(c)** as deposited **(d)** after 50% rolling reduction. **(e)** is obtained by subtracting **(d)** from (e).
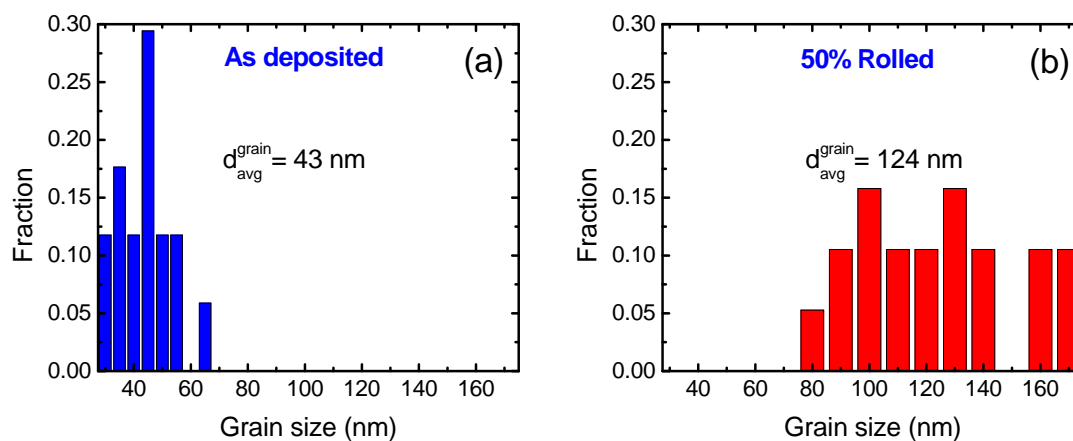
Fig. 48 Normalized statistical distribution of columnar grains obtained from several TEM micrographs **(a)** as deposited **(b)** after 50% rolling reduction.

To examine the introduction of dislocations in nt Cu, systematic XTEM experiments were performed. Figure 49a is a higher magnification, bright field XTEM image of 50% rolled Cu taken along the Cu <110> zone axis. High density dislocations are observed along twin interfaces and within twin lamella. To reveal the characteristics of defect density at twin interfaces, the same specimen is tilted so that only Cu {111} diffraction spots are highlighted, as shown in the SAD inset of Figure 49b. Such conditions, close to the two-beam condition, reveal a series of white dots aligned along twin interfaces, which are not discernable due to the current imaging conditions. These white dots reveal the core of dislocations where the distortion induced a maximum contrast. The average spacing of dislocation at the twin interface is estimated to be approximately 6 nm. Dislocation segments within the twin lamella are also observed as shown in the magnified XTEM micrograph in Figure 49c. HRTEM experiments were performed to identify the type of dislocations at or in close proximity to twin interfaces.
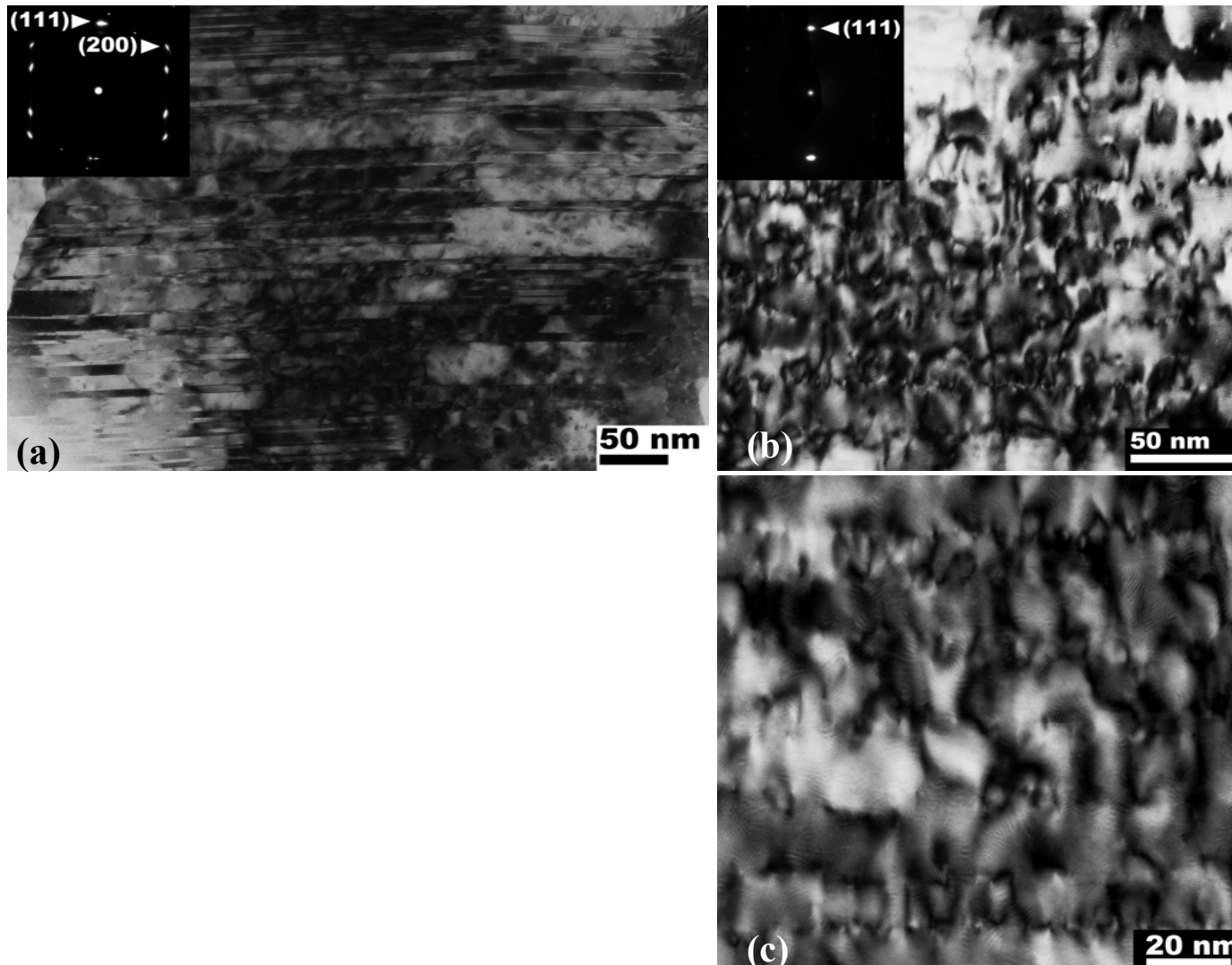
Fig. 49 (a) Cross-sectional TEM image after 40% rolling strain from <110> zone as suggested by inserted SAD showing twins. **(b)** Part of the image in (a) is tilted close to two-beam condition so that the defects can be seen. Note that inserted SAD shows (111) spots only. **(c)** Part of the view area in (b) is seen at a higher magnification shows dislocations trapped at the twin interfaces.

Figure 50a is an HRTEM micrograph of the foil rolled to 50%, showing defects at twin interfaces. The squares in Figure 50a are magnified in Figure 50 (b-c). Figure 50b shows a step (ledge) at the twin interface. The dislocation associated with the step at the twin boundary is identified to be a Shockley partial, with $\vec{b} = \dfrac{a}{6} <112>$, by drawing Frank circuit [152]. The circuit starts at S_2 and ends at F_2 at the upper part of the TB and starts at S_1 and ends at F_1 at the lower part of the TB. At a few atomic layer underneath the twin interface lies a Frank partial dislocation, with $\vec{b} = \dfrac{a}{3} <111>$. Similar types of defects are also observed in Figure 50c. (Figure 50d is inverse FFT of Fig.6c showing only one set of inclined (111) planes whereas Figure 50e shows two sets of inclined (111) planes. Several dislocations are identified in both of these images.

Figure 51a displays X-ray diffraction pole figures of as-deposited nt Cu film. The texture strength and RP error of the ODF calculation are noted on the figure. Pole figure were recalculated from the ODF in order to display non-measured regions at sample tilt angles greater than 80°.
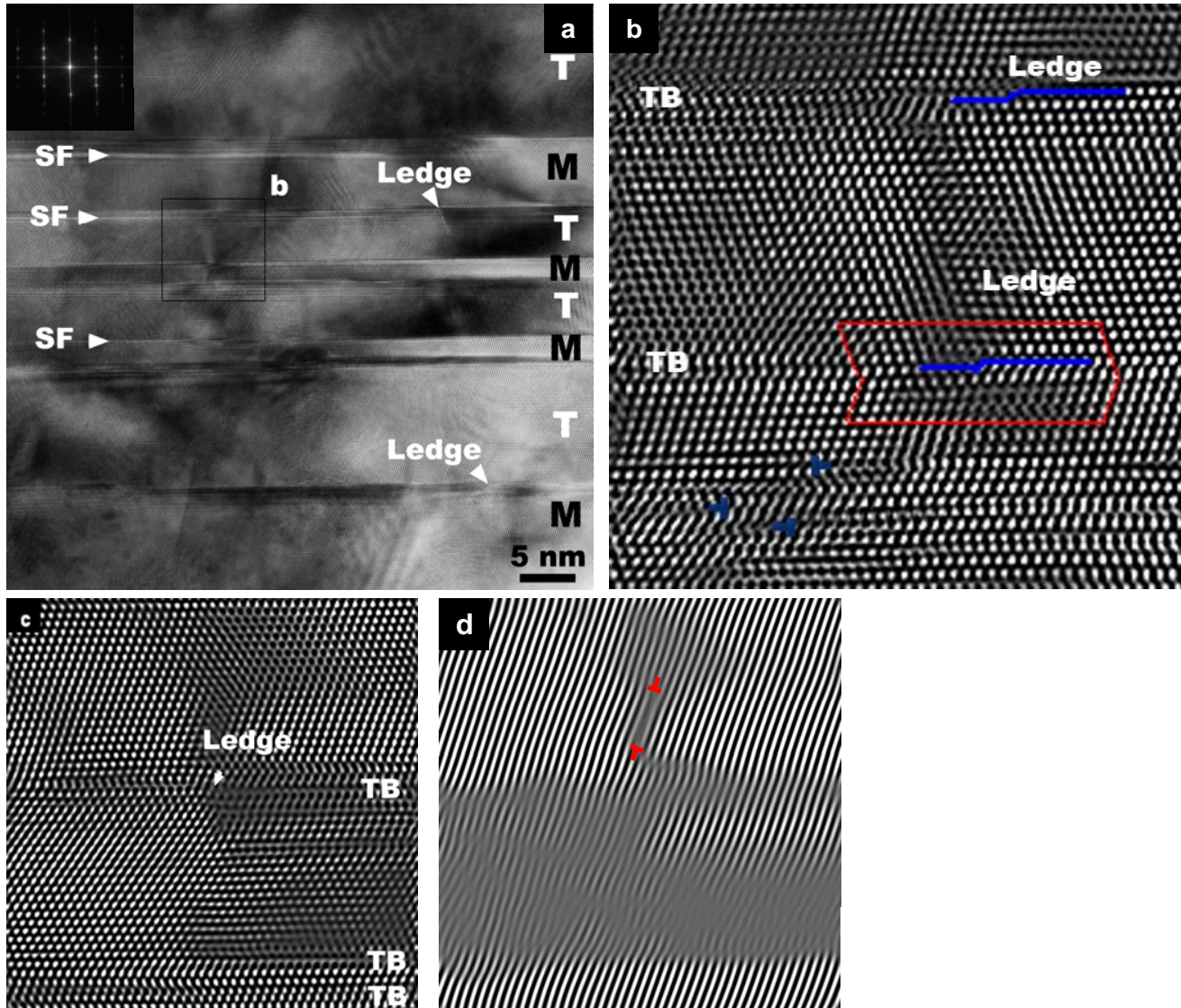
Fig. 50 (a) High resolution cross-sectional TEM image and inserted FFT of the film after 33% rolling strain **(b)** The section in square b is magnified. The step at the interface is shown along with the Frank circuit **(c)** The section in square c is magnified. The step at the interface is seen. In addition microtwin is identified in this figure **(d)** Only one set of inclined (111) planes of image (c) shows the dislocations.
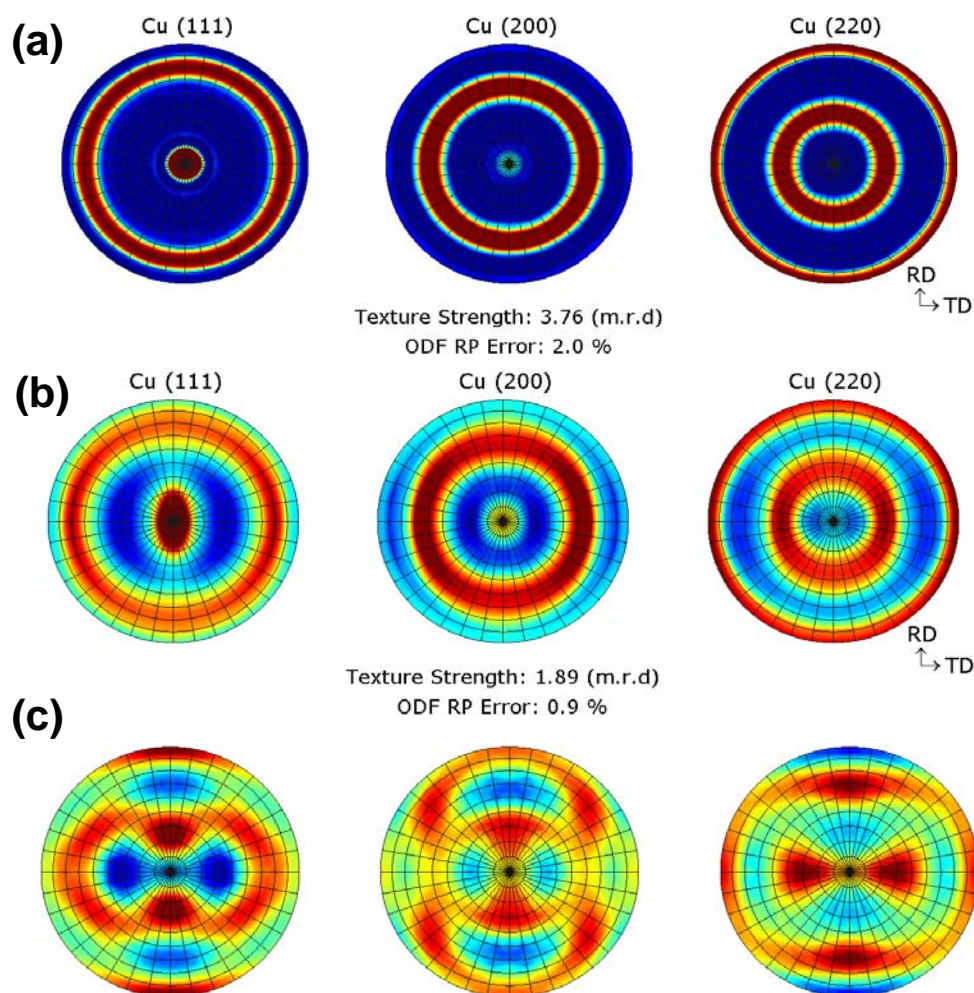
Fig. 51 (a) X-ray pole figure of as deposited nanotwinned polycrystalline Cu films **(b)** X-ray pole figure of nanotwinned polycrystalline Cu films after 50% rolling strain. **(c)** X-ray pole figure of polycrystalline Cu films without twins show a split indication of out-of-plane rotation after rolling.

The accuracy of these regions is dependent on the relative ODF error. The X-ray pole figures show strong <111> fiber texture perpendicular to rolling plane (or twin interface). The uniform outer rings indicate that the polycrystalline Cu has a random distribution of in-plane grain orientation. Figure 51b displays the X-ray diffraction pole figure results after 50% rolling strain. The results show insignificant out-of-plane rotation

after rolling, comparing to significant crystal rotations in bulk Cu subjected to the similar magnitude rolling as shown in Figure 51c.

IV.3.2. Rolling induced work hardening

Figure 52 shows evolution of true stress, estimated as 1/3 of measured hardness values, as a function of rolling strain (true strain). There is a gradual and moderate increase in true stress after 50% rolling strain or true strain.
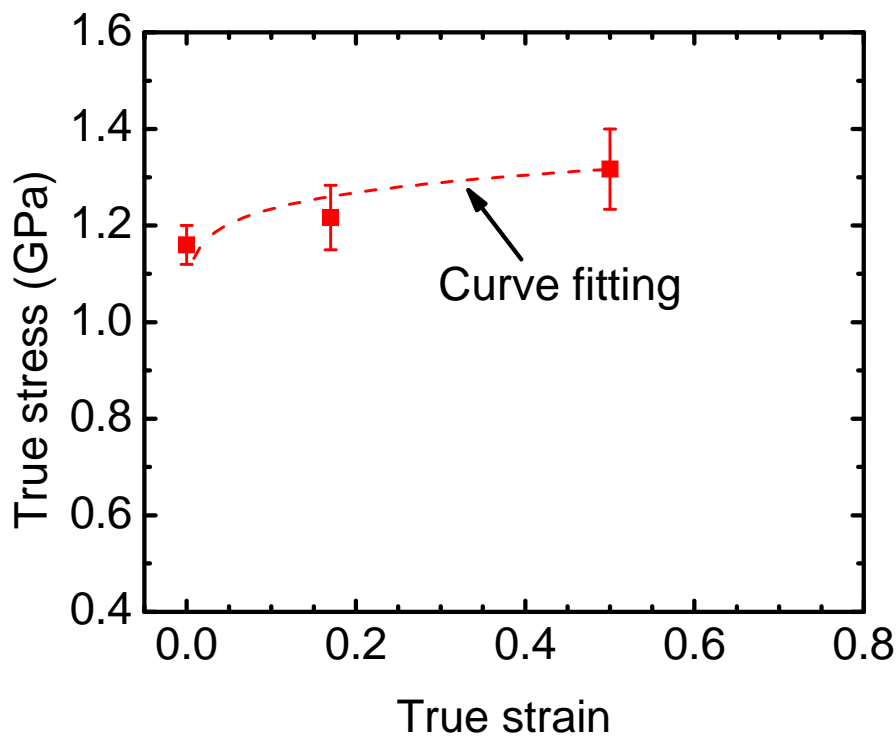
Fig. 52 Evolution of true stress, estimated as 1/3 of hardness, vs. true strain (rolling strain) in nt Cu. Hardness increases moderately after rolling, and such work hardening behavior is simulated, shown as a dash line, by using equation described in the text.

The work hardening, evolution of true stress (σ) vs. strain (ε) in nt Cu is simulated by using

$$\sigma = K_1 + K_2 \varepsilon^n \tag{25}$$

where K_1, K_2 and n are fitting constants, and n is known as work hardening exponent. For comparisons, work hardening results in bulk Cu and Cu/Nb 30nm multilayers (the individual layer thickness in Cu and Nb is identical to be 30 nm), are also shown [153]. The values of fitting constants are shown in Table 5.

Table 5. Comparisons of constants in work hardening equation ($\sigma = K_1 + K_2 \varepsilon^n$) for nanotwinned Cu, bulk Cu with coarse grains, and Cu/Nb 30 nm nanolayers.

	K_1 (MPa)	K_2 (MPa)	n
Nt Cu	780	570	0.1
Bulk Cu	~ 0	350	0.35
Cu/Nb 30nm	1370	300	0.25

The value of K_1 is significantly higher than that of bulk Cu as a result of higher yield strength of the as-deposited nt Cu, and is moderately lower than that of Cu/Nb 30 nm specimen. K_2, representing the increment in strength due to unit increase in strain, is greater than those of Cu/Nb, ~ 300 MPa, and bulk Cu. ~ 350 MPa. The rate of work hardening is calculated based on the fitting parameters, and results are shown in Table 6.

Table 6. Calculated work hardening rate for nanotwinned Cu, bulk Cu with coarse grains, and Cu/Nb 30 nm nanolayers.

	nt Cu	Bulk Cu	Cu/Nb 30 nm
$\sigma(\varepsilon=0.5)/\sigma\ (\varepsilon=0)$	1.14	10	1.25
$d\sigma/d\varepsilon$	$57\varepsilon^{-0.9}$	$124\varepsilon^{-0.65}$	$76\varepsilon^{-0.75}$

The evolution of work hardening rates vs. true strain are given in Figure 53 for both nt Cu and bulk Cu. The magnitude of work hardening rate of nt Cu is similar to that of bulk Cu at a true strain level of 3-4 %, and reduces more rapidly thereafter.
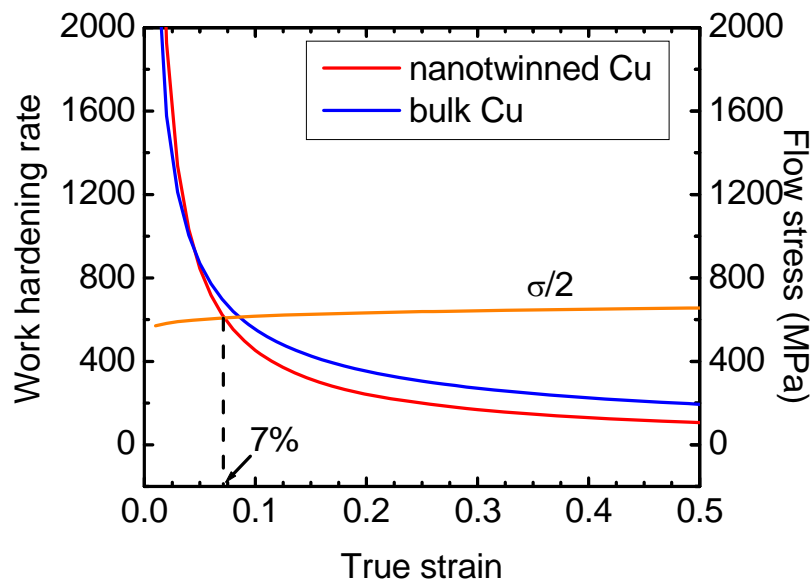
Fig. 53 Comparisons of work hardening rate in nanotwinned Cu and coarse grained bulk Cu.

IV.4. Discussion

IV.4.1. Texture evolution

Rolling of coarse grained Cu typically induces out-of-planes rotations of parent planes, such as {111} planes. Such rotations can accommodate the shear strains induced during rolling and imply characteristic deformation mechanisms in coarse grained materials. The suppression of such rotations in nt Cu suggests the activation of different type of deformation mechanisms.

Also it is known that the rolling texture of fcc metals depends on the stacking fault energy associated with the metal [154, 155]. In a previous study on electro deposited nanotwinned Cu shear bands were seen [156] as a result of deformation. The formation of shear bands is attributed to inhomogeneous deformation in thinner twins. Similar to current study, the Shockley partials were activated extensively along the TBs producing a high density of ledges. The study also showed that shear banding destroys the lamellar twin structure. The deformed structure was dominated by a lamellar dislocation structure typical for cold rolled samples. However, the current study does not reveal shear bands.

The concept of symmetric slip is used to interpret the insignificant out-of-plane rotation observed in rolled nt Cu. This idea has also been applied to rolled nanolayered Cu/Nb multilayer [157]. In twinned fcc structures, both sides (i.e. the matrix and the twin) of a twin boundary contain three conventional {1 1 1}-type glide planes non-parallel to twin boundary plane, and each {1 1 1} plane contains two glide dislocations with ½ <1 1 0> type Burgers vector that are not contained in the twin boundary. Both sides of twin boundaries also contain three less likely, but sometimes observed, {1 0 0}-type glide planes non-parallel to the twin boundary, and each {1 0 0} plane contains one

glide dislocation with ½ <1 1 0> Burgers vector. When foils are subjected to normal loading (perpendicular to twin boundary plane), Schmid factor is 0.32 for all glide dislocations on {1 1 1}-type glide planes, and 0.48 for all glide dislocations on {1 0 0}-type glide planes. Therefore, the activity of dislocations is the same either on all {1 1 1}-type planes or on all {1 0 0}-type planes. Given the same number of slip systems and the same slip activity on all glide planes, plastic deformation can take place in symmetrical mode in both crystals of twin boundaries. As a result, there is no net rotation of the (1 1 1) twin plane.

IV.4.2. The retention of the average twin lamellar thickness due to annihilation of twin interfaces

If we assume there is no annihilation of twin interfaces and columnar grain boundaries and no volume change after rolling to 50% strain, the average twin thickness and columnar grain sizes should be ~ 2 nm (1/2 of original twin thickness) and 86 nm (double the original grain size), respectively. However TEM analyses reveal the negligible change of the average twin spacing and an average grain size of ~ 124 nm. Hence a large fraction of twin interface and columnar grain boundaries must have been annihilated. The annihilation of very fine twins, 1-2 nm in thickness is observed as shown in Fig 47e.

From a geometric point of view, the annihilation of these fine twins will surely lead to slight increase of average twin spacing, a phenomena also confirmed in Figure 47d. However, continuous rolling will subject thicker twins to constant compressive and shear strain and hence reduce the twin thickness. Hence, the competition between twin

thickening due to interface annihilation and twin thinning due to continuous rolling to the retention of the average twin thickness.

We shall now discuss the mechanisms of twin thickness variations, thinning or thickening. Our MD simulations have shown that twin interface is a strong barrier to the transmission of single dislocations in twin lamella. Figure 54 shows the transmission of a perfect dislocation across twin interface under tension and shear stress. In both cases, a ledge is generated at twin interface as a result of trespassing event. A Shockley partial is created at the ledge. The Shockley partials created this way can glide up or down along the twin interfaces causing the migration of TBs as shown schematically in Figure 55.
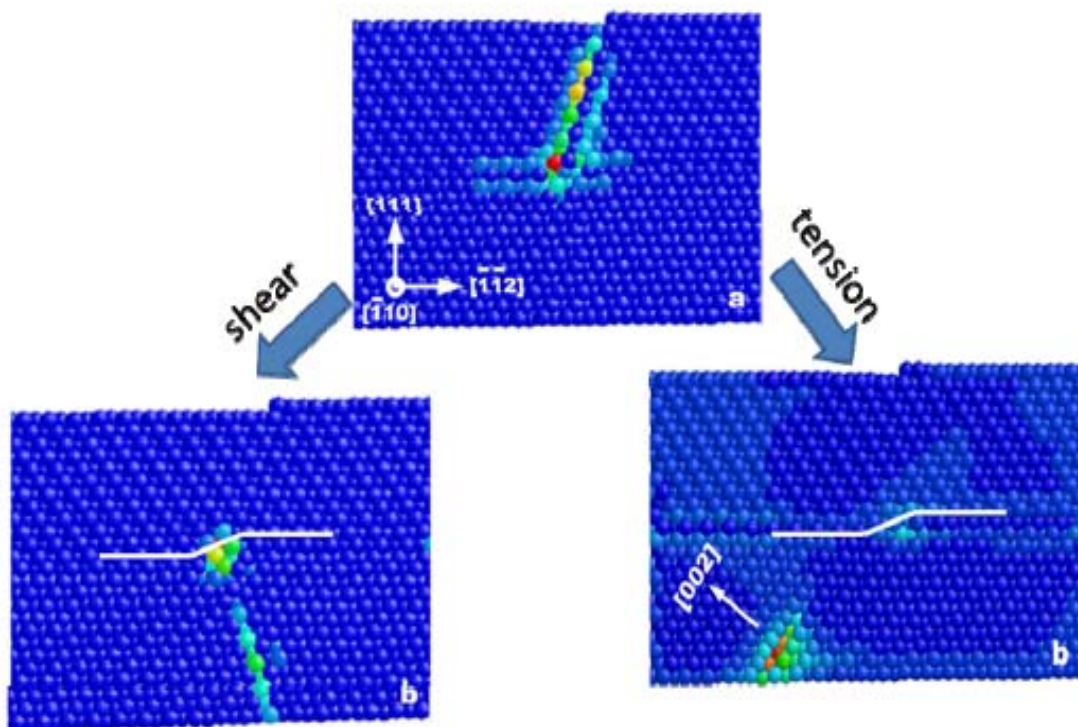
Fig. 54 Generation of ledge, Shockley partials, at the twin interface due to the transmission of perfect dislocations across twin interfaces.
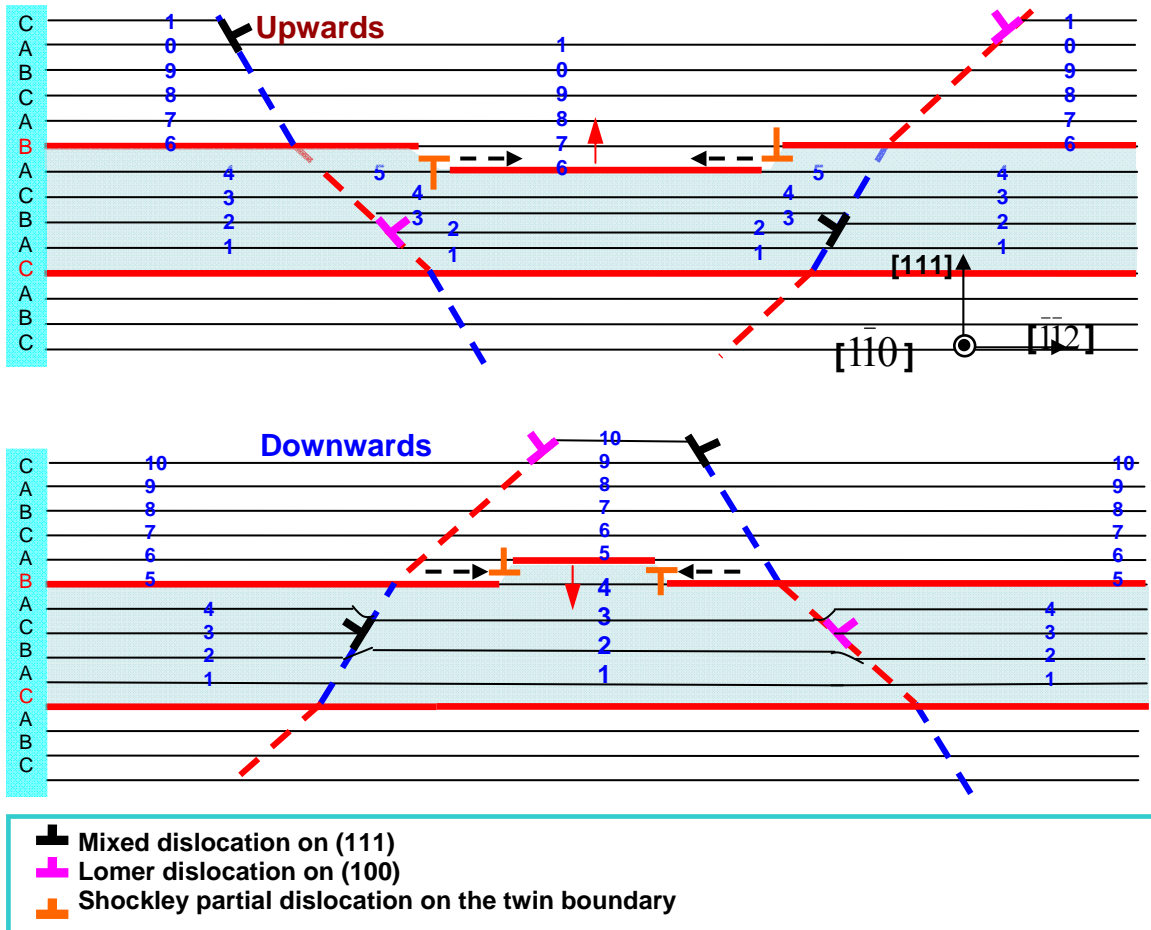
Fig. 55 Migration of twin interface along its direction normal up or down as a result of glide of Shockley partials along twin interfaces.

The glide of these Shockley partials can lead to the migration of twin interfaces along their direction normal. The vertical migration of twin interfaces is crucial to explain the annihilation of twin interfaces. When twin interfaces are very close to each other, 1 nm or less, the two interfaces will be annihilated by slightly shear the twin lamella and as a result of annihilation, the strain energy stored at twin interfaces are reduced.

Recent studies on electrodeposited nt Cu show that when the glissile Shockley partials encounter sessile Frank sites they form nanometer size steps [102, 149, 151]. When several steps combined together at a CTB they change the morphology from flat to curved [144, 151] which is not the case in the current study. It is mostly because of the relatively small grain size in this study compared to electrodeposited nt Cu. Small grain size in this study does not allow accommodate several nanometer size steps that changes the morphology. It was also experimentally shown that these steps act as a dislocation source [144, 137, 151]

Furthermore, one can estimate the elongation based on the dislocation density shown in Figure 41c. The average spacing of dislocations along twin interfaces is ~ 6 nm, and the average twin thickness is~ 6-7 nm. Such analysis yields a dislocation density of $2.4 \times 10^{16}/m^2$. Such a high dislocation density is comparable to those of severely deformed bulk metals. Also by using the Burgers vector of a perfect dislocation in Cu and the average distance of dislocation along twin interface, the average distortion caused by dislocations alone amounts to ~11% elongation along the rolling direction.

IV.4.3. Work hardening in nanotwinned Cu

In spite of lower work hardening exponent, n, the nt Cu does show considerable work hardening capability. The work hardening rate of nt Cu is initially comparable to that of bulk Cu. A plot of flow stress divided by 2, $\sigma/2$, is given in Fig. 53. And the interception of such plot with the work hardening rate leads to a uniform strain of ~ 8%, based on the flow stability criteria of $d\sigma/d\varepsilon > \sigma/2$. This is different than the conventional criteria of $d\sigma/d\varepsilon > \sigma$, where diffuse necking is typically observed. Localize necking is

typically observed in thin sheet metals due to a geometric softening effect [153]. Twin interfaces has extraordinary capacity in storing high density dislocations as discussed previously. Beside glissile Shockley partials, Frank partials as well as Lomer dislocations are frequently observed in rolled Cu. These defects will create extra barriers to the glide of dislocations and hence contribute to work hardening. Work hardening may also originate from the generation of steps at twin interfaces, where Shockley partial dislocations may resist the transmission of dislocations. Misfit dislocations at nanolayer interfaces have shown to be strong obstacles to the glide of dislocations within the layers [153, 157]. Also, lattice dislocations can accumulate at boundaries as in the symmetric slip model, with their edge components acting to relieve misfit. Local dislocation accumulation locally hardens the region and causes further slip to occur elsewhere or on a different system and). Burgers vectors from different systems can interact to form Lomer dislocations, which in turn can annihilate with opposite sign Lomer dislocations, both being recovery effects. If this hardening/recovery process were perfect, stable flow could occur without macroscopic hardening. However, statistically, dislocations of a given sign tend to accumulate locally, giving dislocation storage, as observed, and added hardening. All of these factors contribute to local hardening and consequent plastic stability. The average spacing of dislocations along twin interfaces is 6 nm, and the average twin thickness is 6–7 nm. These values yield a dislocation density of $2.4 \times 10^{16}/m^2$. Such a high dislocation density is comparable to those of severely deformed bulk metals.

IV.5. Summary

Nanotwinned Cu shows remarkable plastic flow stability under room temperature rolling. No shear bands are observed after 50% rolling reduction. The retention of {1 1 1} fiber texture after rolling is interpreted in terms of symmetric slip. The retention of average lamellae thickness after 50% reduction in sample thickness implies elimination of some twin interfaces during rolling. This is confirmed by measured statistics of twin lamellae thickness before and after rolling. The observed work hardening after rolling is interpreted in terms of stored dislocations at interfaces.

CHAPTER V

EPITAXIAL NANOTWINNED CU FILMS WITH HIGH STRENGTH

AND HIGH CONDUCTIVITY[*]

V.1. Overview

This chapter reports the successful synthesis of epitaxial (single-crystal like), nanotwinned Cu films with tailored twin boundary spacing. Epitaxial nanotwinned Cu films, with an average twin spacing ranging from 7 to 16 nm, exhibit a high ratio of hardness-to-electrical resistivity. The hardness of these Cu films approaches 2.8 GPa, and their electrical resistivities are comparable to that of oxygen free high conductivity Cu. The achievement of high strength-to-resistivity ratio is due to the unique characteristics of coherent twin interfaces, i.e., their inherently high resistance to the transmission of single dislocations, and an order of magnitude lower electron scattering coefficient than high angle grain boundaries. Theoretical analysis shows that the strength-to-resistivity ratio decreases with reducing grain size in nanocrystalline metals with high-angle grain boundaries, but increases with reducing twin spacing in nanotwinned metals. A unique superlattice structure is observed across domain boundaries. Metal films with high strength and high conductivity could have superior electromigration resistance for microelectronics applications. High strength, ductile metal films also have impact in MEMS/NEMS devices.

---

[*] Part of the data reported in this chapter is reprinted with permission from "Significant enhancement of the strength-to-resistivity ratio by nanotwins in epitaxial Cu films" O. Anderoglu, A. Misra, F. Ronning, H. Wang, and X. Zhang, 2009. *Journal* of *Applied Physics.* 106, 024313-1-024313-9, Copyright © 2009 by American Institute of Physics.

V.2. Introduction

Conducting metals are being used in diverse applications including electrical interconnects in microelectronics, electrical power transmission and electrical conductors in high-field magnets, and it is desirable to have both high yield strength and high electrical conductivity. Strengthening mechanisms such as grain refinement, alloying, cold working, etc significantly lower the electrical conductivity of pure metals. The development of high tensile strength and high electrical conductivity alloys has been an active research subject for decades. Various approaches have been used to increase the strength-to-resistivity ratio in Cu-based conductors, such as alloying [158-162], precipitate hardening [163, 164] etc. Recent works on nanoscale growth twins show that the nanotwinned structures are promising in increasing the strength without significantly compromising the electrical conductivity [69, 134]. Coherent twin boundaries are effective in blocking dislocation motion and thus providing substantial strengthening to the material [64, 104, 136, 165]. Strengthening due to nanoscale twin interface has been studied in detail both experimentally [15, 69] and via atomistic modeling [137, 138]. At the same time, high electrical conductivity can be achieved in twinned metals as the electron scattering coefficient at coherent twin boundaries is typically considered to be an order of magnitude lower than that at high angle grain boundaries [69, 134]. Pulsed electrodeposition has been proven effective in achieving high strength and high conductivity in Cu by fabricating high density twins in submicron sized Cu grain [69]. In a recent article Lu et al investigated the maximum strength of nanotwinned copper samples with different twin thicknesses and found that the strength increases with

decreasing twin thickness, reaching a maximum at 15 nanometers, followed by a softening at smaller values that is accompanied by enhanced strain hardening and tensile ductility. They also showed that the strongest twin thickness originates from a transition in the yielding mechanism from the slip transfer across twin boundaries to the activity of preexisting easy dislocation sources [166]. However, high strength and high conductivity have not been realized simultaneously in sputtered Cu films.

Magnetron sputtering has been used to fabricate high strength Cu, Ni, and 330 stainless steel films with fine-scale twins [15, 74, 167]. Previously we have shown that sputtered polycrystalline (poly), nanotwinned (nt) Cu films have twin interfaces oriented preferentially normal to growth direction [15]. These poly nt films have an order of magnitude higher hardness (~ 3.5 GPa) than their bulk counterpart. However, due to the presence of high-angle grain boundaries and in some cases, minute Fe impurities, the resistivity was also found to be very high. High temperature vacuum annealing was used to enlarge the column grain size while maintaining a high density of growth twins in an attempt to increase the strength-to-resistivity ratio of poly nt Cu films. The nanotwins in sputtered Cu films show very high thermal stability. After vacuum annealing up to 800°C, Cu films retain an average twin spacing of less than 20 nm, and high hardness, exceeding 2 GPa. Grains coarsen significantly from 50 to more than 500 nm with a substantial decrease in resistivity [112]. But the resistivities of these annealed Cu films are still high compared to that of OFHC Cu. Recently, we reported another approach that has the promise of achieving high strength-to-resistivity ratio. Epitaxial Cu films with a high density of growth twins have been fabricated on Si substrates [135]. In this paper, we present a thorough study of the correlations of microstructure, mechanical and

electrical properties of these epitaxial nanotwinned Cu films. Such study indicates that compared to nanocrystalline metals with high-angle grain boundaries, coherent nanotwinned structures offer a much more effective approach in enhancing the strength-to-resistivity ratio.

V.3. Results

V.3.1. Microstructure

XRD patterns of Cu films deposited on Si (110) substrates are shown in Figure 56 with deposition rates of 9 and 30 Å/sec. Both patterns show that the films have only one orientation, Cu {111}, indicating epitaxial growth.
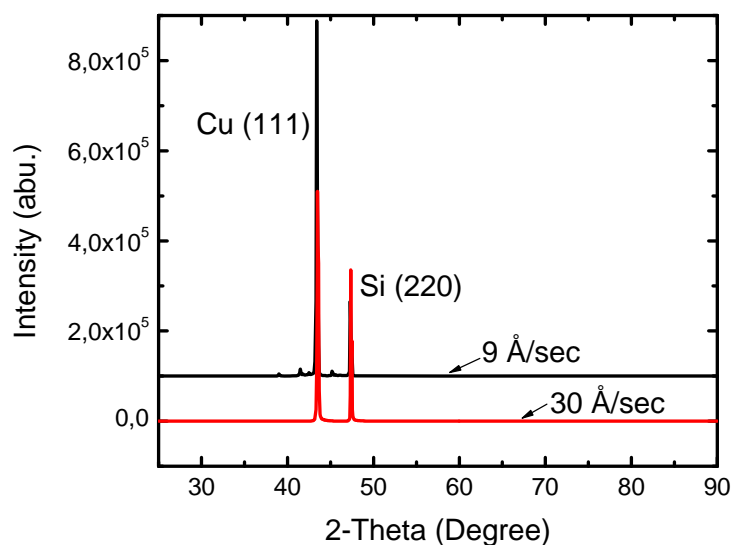
Fig. 56 Out of plane XRD patterns of Cu films deposited at a rate of 9 and 30 Å /sec respectively showing single Cu (111) peak on Si (110) substrates [135].
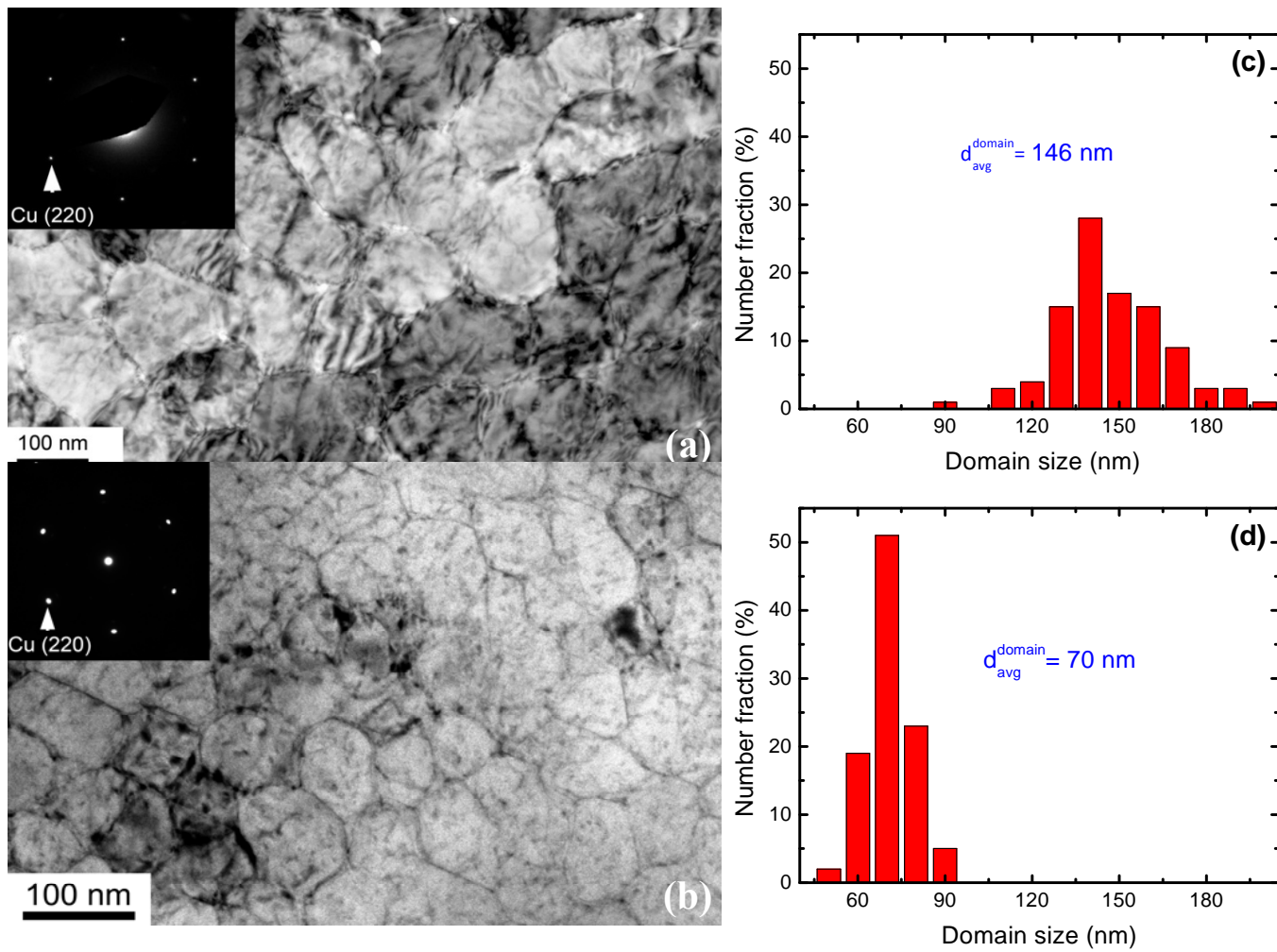
Fig. 57 The plan view TEM images of Cu deposited at **(a)** 9 and **(b)** 40 Å/sec. Corresponding statistical distribution of domain sizes shown in **(c)** and **(d)** [135].

To confirm the epitaxial growth of Cu {111} on Si (110) substrate, TEM experiments were performed. The plan view TEM images of Cu deposited at 9 and 40 Å/sec are shown in Figure 57(a) and (b). At the first glance both images seem to indicate polycrystalline structures of these films. However, selected area diffraction (SAD) patterns (obtained through an aperture covering the whole image) reveal distinct spots as opposed to arc or rings. In both cases, the SAD patterns indicated a single crystal face-centered cubic structure imaged along a <111> zone axis. Figure 57(c) and (d) show the size distributions of the domains. The average domain size decreases from 146 to 70 nm with increasing deposition rate from 9 to 40 Å/sec.

The cross section of the films can be observed from two axes, Si <111> and <112>, normal to each other. Cross-sectional TEM (XTEM) micrographs of Cu films deposited at 9, 30 and 40 Å/sec are shown in Figure 58 (a-c) along Si <111> zone axis. Along the Cu <110> zone axis, both the {111} plane that is parallel to the twin boundaries and the {111} plane that is twinned are visible Thus, twin contrast is observed along this orientation. Films have columnar structure and a high density of {111} type twin interfaces oriented perpendicular to growth direction. The inserted SADs show single crystal Cu along [011] zone axis with spot splitting across the $(11\bar{1})$ twin plane. The statistical distributions of the twin thicknesses are shown in Figure 58 (d-f). The average twin lamellae thickness (L_{avg}^{twin}) is calculated from the approximate full-width at half maximum (FWHM) of the statistical thickness distributions of twin and matrix. L_{avg}^{twin} decreases from 16 to 7 nm when the deposition rate increases from 9 to 40 Å/sec.

Figure 59 (a) shows the (XTEM) micrograph of a Cu film deposited at 30 Å/sec from Si <112> diffraction zone axis. Inserted SAD pattern reveals distinct spots,
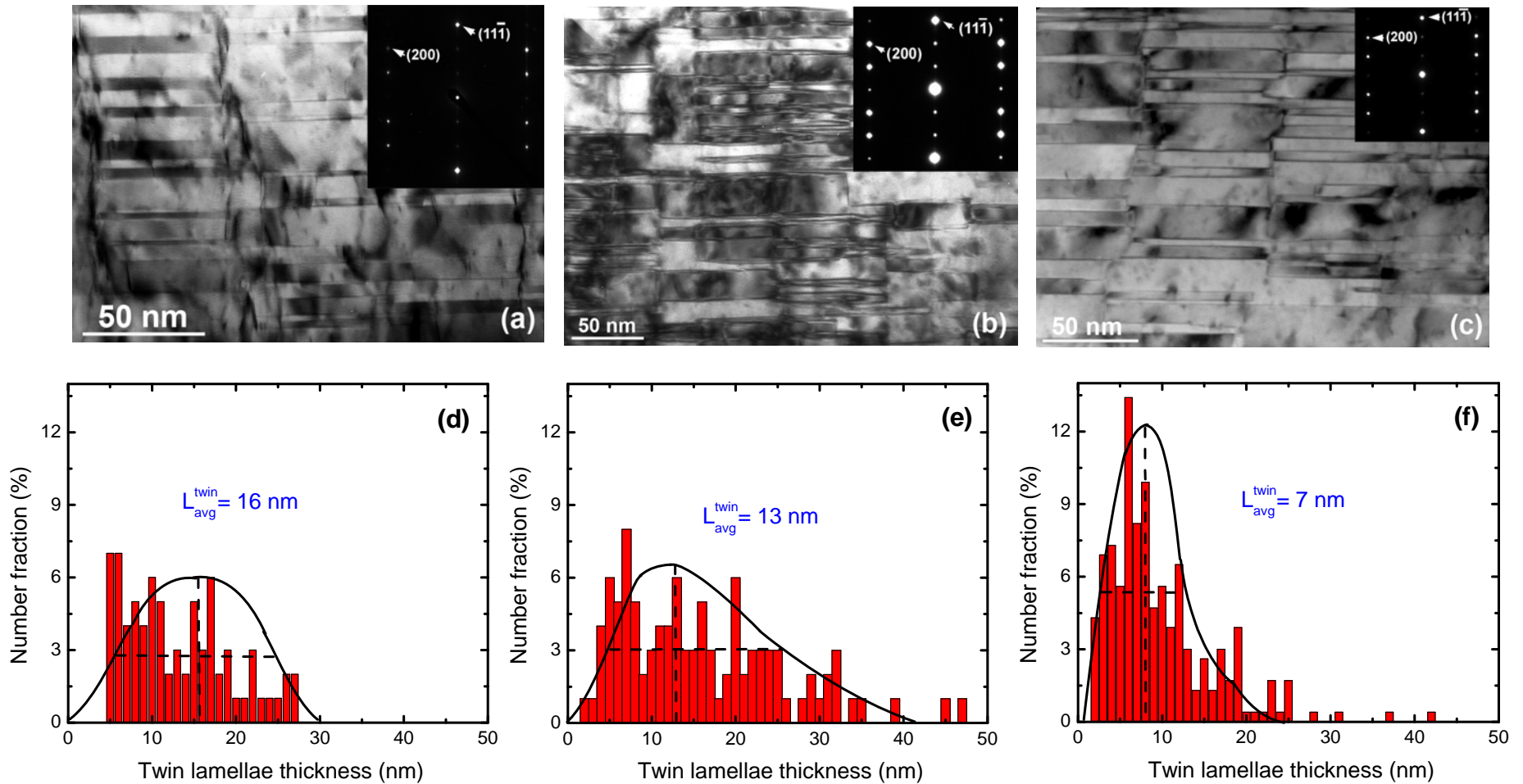
Figure 58 (a-c) Cross sectional TEM images of Cu films deposited at 9, 30, and 40 Å /sec, respectively, examined from Si [111] diffraction zone. High density {111} twins are seen in all cases with twin planes oriented normal to growth direction. SAD patterns confirm typical twin pattern as well as the epitaxial growth of Cu films. **(d-f)** Statistical distribution of twin thicknesses of Cu deposited at 9, 30, and 40 Å/sec respectively. Average twin spacing decreases with increasing deposition rate [134].
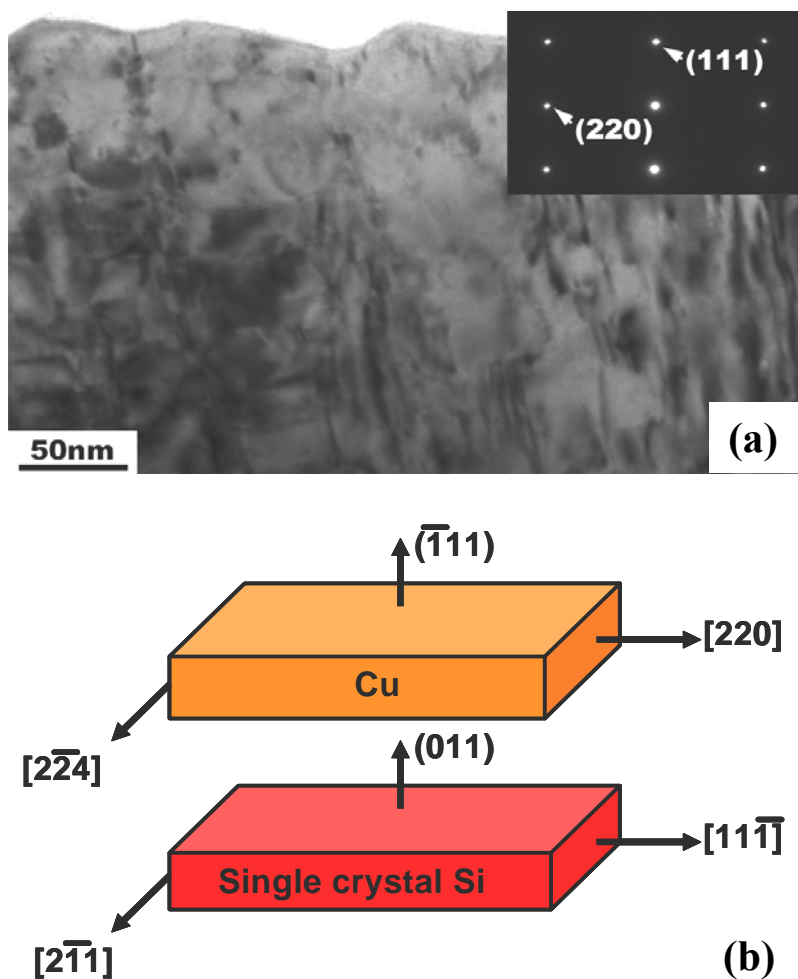
Fig. 59 (a) Cross sectional TEM micrograph of epitaxial Cu films (deposited at 30 Å /sec) on Si (110) substrate examined from Si <112> diffraction zone. SAD pattern indicates that Cu has single crystal like diffraction pattern along Cu <112> zone. **(b)** Schematics illustrate the epitaxial orientation relationship of twined Cu films grown on Si (011) substrates [134].

indicating single crystal characteristics of the films. Figure 59 (b) shows the schematic of the epitaxial growth of Cu (111) film on single crystal Si (110) substrate. The <112> zone axis only contains one set of {111} plane parallel to the twin boundaries, and hence the contrast from twins is not clearly evident in this image.
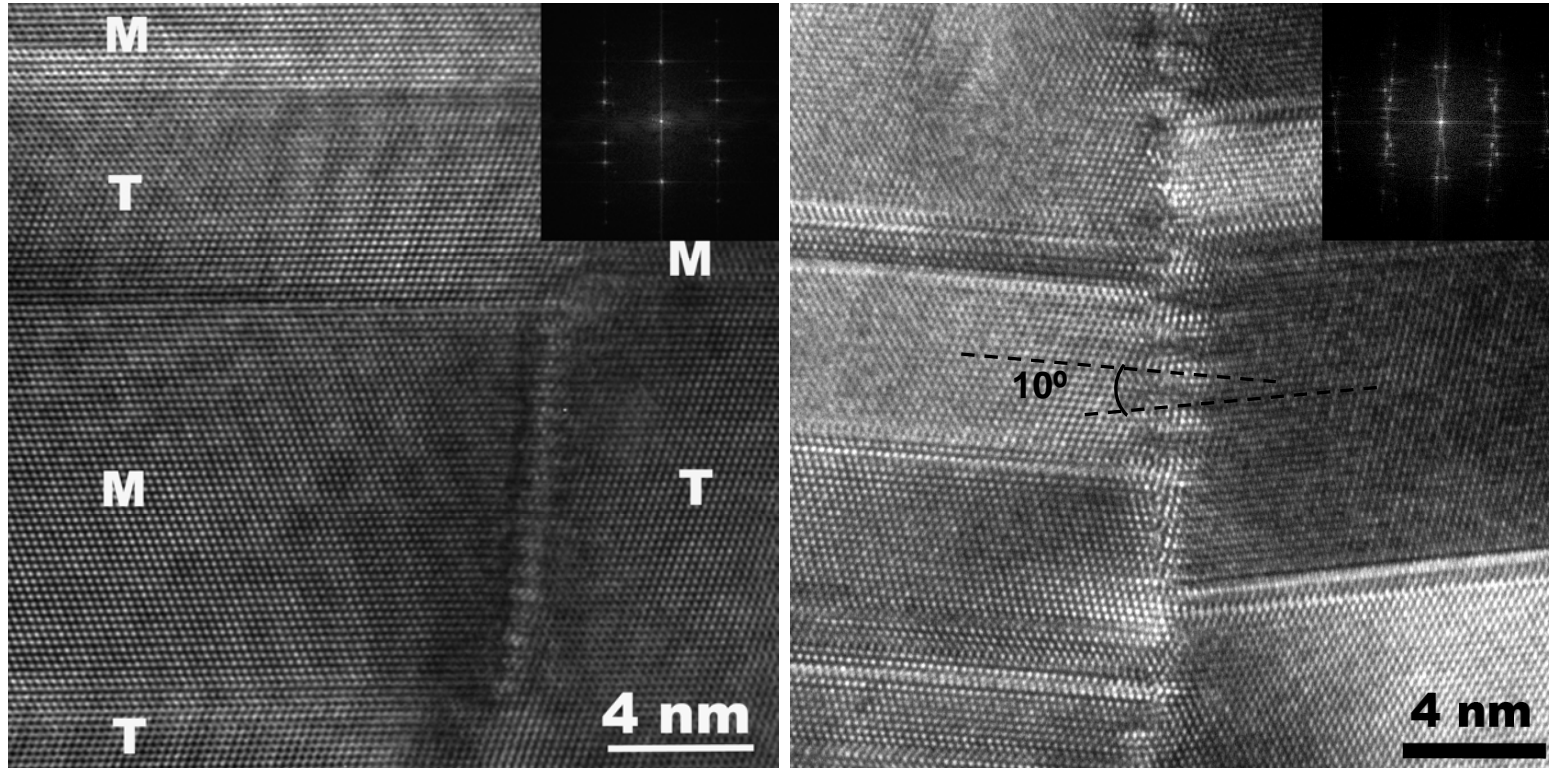
Fig. 60 (a) HRTEM image of Cu film deposited at 40 Å/sec shows the clear twin interface and low angle grain boundary between two neighboring domains. Twins coincide in the adjacent grains with a few atomic planes offset. **(b)** HRTEM image of nanocrystalline Cu with nanoscale twins. High-angle boundary separates the twins on each side of the grain, therefore twins grow independent from each other [134].

To examine the detail of domain boundary, HRTEM micrographs of epitaxial nt Cu (deposited at 40 Å/sec) and poly nt Cu films are compared in Figure 60. The vertical boundary is either the domain boundary in epitaxial nt Cu or grain boundary in poly nt Cu, and in both cases horizontal boundaries are twin interfaces. Note that in epitaxial nt Cu, {111} planes in the adjacent domains are continuous across domain boundaries with negligible misorientation as shown in Figure 60(a). However, in poly nt Cu films shown in Figure 60 (b), the {111} planes in the adjacent columns are misaligned by ~ 9° [135]. The inserted fast Fourier transform (FFT) images in Figure 60 also confirm the misalignment in poly nt Cu, and no misorientation in epitaxial nt Cu.

V.3.2. Hardness

Flow stress (estimated as hardness/2.7) vs. $t^{-1/2}$ or $d^{-1/2}$ (t - twin spacing, d – grain size) is plotted in Figure 61 for twinned and polycrystalline Cu. [134] In general hardness increases linearly with decreasing twin spacing (grain size) down to ~ 50 nm. A deviation from this typical Hall-Petch strengthening behavior is observed at smaller grain size and twin spacing. The strength of nc nt Cu and epitaxial nt Cu approaches 1 GPa or higher at a twin spacing of 10 nm or less. The Hall-Petch slope of twinned Cu seems to be lower than that of ultra-fine grain (UFG) Cu except when compared to condensed nc Cu powder, where incomplete consolidation leads to lower measured hardness values.
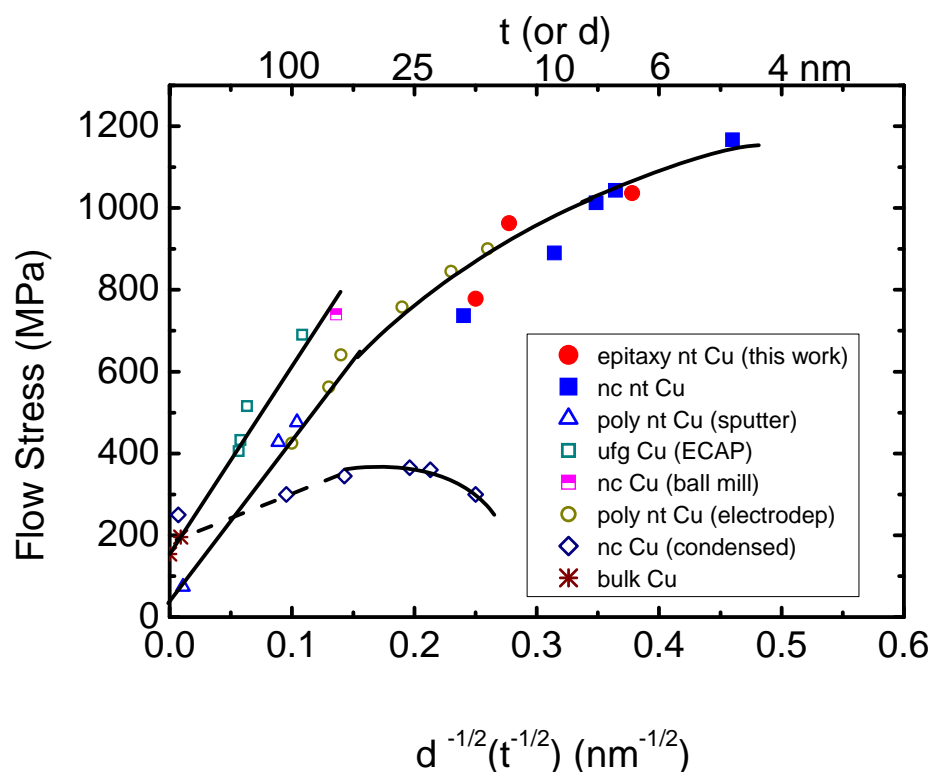
Fig. 61 Hall-Petch plot of sputtered epitaxial and nanocrystalline Cu with nanotwins, and polycrystalline Cu prepared by other techniques. Flow stress values of Cu films are obtained by dividing hardness by a factor of 2.7.

V.3.3. Electrical resistivity

The hardness of epitaxial nt Cu films increases from 2.1 to 2.8 GPa when the average twin spacing decreases from 16 to 7 nm. The results of the temperature dependent electrical resistivity measurements for epitaxial nt Cu are shown in Figure 62a. For comparison, the data for poly nt Cu (as deposited and annealed specimens) [168], and oxygen free high conductivity (OFHC) Cu [169] are also shown in the same plot. Annealing of poly nt Cu up to 800°C results in a significant reduction of resistivity down to ~ 3 μΩ•cm. Room temperature (~293 K) resistivities of epitaxial nt Cu films have

values of 1.69 to 2.31 μΩ•cm, very close to the resistivity of OFHC Cu (1.58 μΩ•cm), and are an order of magnitude lower than that of as-deposited poly nt Cu (28 μΩ•cm).
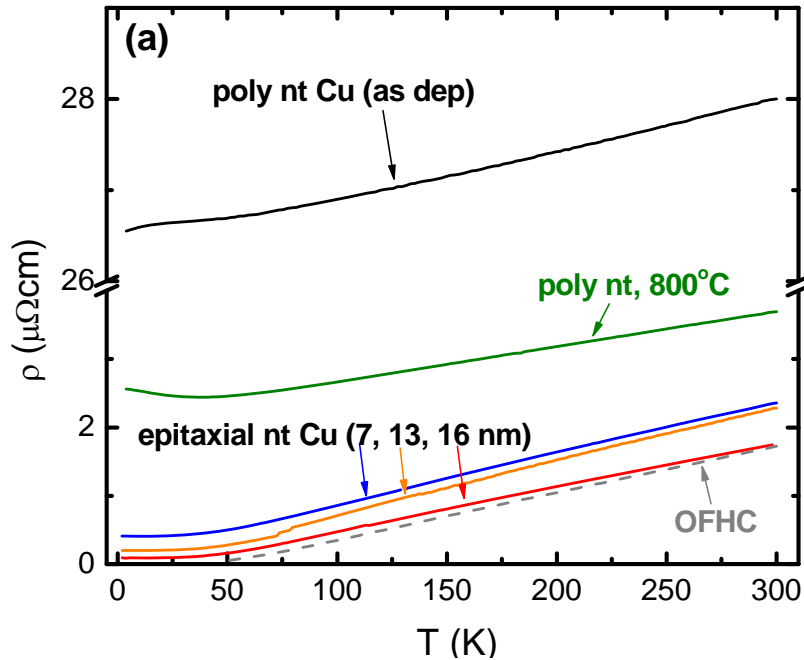
Fig. 62a Temperature dependent resistivity plots for epitaxial Cu films with different average twin thicknesses. For comparison, data for OFHC Cu and poly nt Cu (as deposited and annealed) are also shown.

Figure 62b shows low temperature resistivities of epitaxial nt Cu with three different average lamellae thicknesses. Electrical resistivity of a pure metal at low temperature is expressed by [170]

$$\rho = \rho_0 + JT^k \tag{26}$$

where ρ is the measured resistivity, ρ_0 is the residual resistivity, T is temperature and J and k are constants. ρ_0 and k values are obtained from the least mean squares fit of the data shown in Figure 62b and tabulated in the Table 7.

ρ_0 and k values for bulk OFHC Cu are 1.7×10^{-4} $\mu\Omega\bullet$cm and 4.16-4.84 respectively [169-171]. The ρ_0 values of epitaxial nt Cu films are two to three orders of magnitude higher, but k values are comparable to bulk Cu.
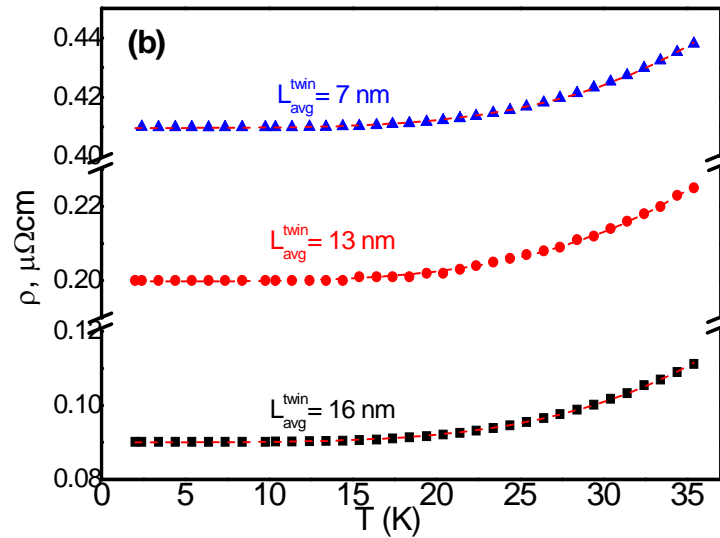
Fig. 62b Low temperature dependence of resistivity plots and fitting curves [134].

Table 7. ρ_0 and k values obtained from fitting resistivity-temperature plots in Fig.62b.

Material	t_{twin} nm	ρ_0 $\mu\Omega$cm	k
Bulk Cu	-	0.00017	4.16-4.84
Epitaxial nt Cu	16	0.09	4.10
Epitaxial nt Cu	13	0.20	3.96
Epitaxial nt Cu	7	0.41	4.11

V.4. Discussion

V.4.1. Microstructures of epitaxial Cu films with nanoscale twins

In our earlier work a model was developed to explain the formation of a high density of nanoscale twins in 330 stainless steel and Cu [74]. The model shows that higher deposition rates and lower stacking fault energies favor the formation of twins. The current study shows that higher deposition rate leads to a smaller average twin spacing. Molecular dynamics (MD) simulations also show that the binding energies of Cu atoms on (111) planes for FCC (perfect crystal) and HCP (twinned crystal) sites are close and hence favor the formation of twins [172]. In sputtered 330 stainless steel films [106], increasing the deposition rate results in a higher volume fraction of twinned columnar grains, however, the average twin lamellar thickness stays the same. In epitaxial nt Cu, essentially all the columns are twinned even at 9 Å/s, thus no change in the volume fraction of twinned grains is seen as the deposition rate is increased to over 9 Å/s.

The microstructure of epitaxial nt Cu films is remarkably different compared to that of poly nt Cu. First, in epitaxial nt Cu, {111} twin planes in adjacent domains are continuous across the twin boundaries with negligible misorientation, whereas in poly nt Cu, there is clearly a large misorientation by $\sim 9^{\circ}$ or greater across the columnar grain boundaries as seen in Fig 4. In epitaxial films, Cu essentially grows as a single crystal on Si with some threading dislocations and twins. In contrast, the Cu film on Si substrate with a native oxide grows by nucleating islands with random in-plane orientations. Within an island, the growth probability of (111) atomic plane is much higher than other atomic planes given its higher atomic bonding energy and higher packing density, and thus (111) fiber texture is dominant. The out-of-plane (along the growth direction) tilting

of Cu (111) atomic planes on Si with native oxide occurs whenever the first few atomic planes are not of (111) type. In epitaxial nt Cu, in-plane rotation of (111) domains is prohibited as well since mismatch strain is minimized only when Cu <110> // Si <111> and Cu <112> // Si <112>. Second, in epitaxial nt Cu, twin or matrix often extend across columnar domain boundary into adjacent columns as shown in Fig. 3 (a-c), 5(a). The epitaxial nt films may be considered as bicrystals consisting of horizontal Σ3 (111) twin interface and vertical Σ3 (112) twin boundaries. The Σ3 (112) domain boundaries form at the intersection of matrix from one column with twin from the adjacent column. Systematic HRTEM studies show that most (111) twin boundaries are coherent, whereas the (112) twin boundaries is either coherent or incoherent. In general, when deposition rate is lower, (112) twin boundaries tends to be more coherent.

V.4.2. Validation of the thermodynamics model describing the formation of growth twins

During sputtering deposition, atoms from the vapor phase condense on a substrate to form the solid film. The critical nucleus size r* for the perfect and twin nucleus is derived as [173]

$$r^*_{perfect} = \frac{\gamma}{\left(\dfrac{kT}{\Omega} \ln\left[\dfrac{J\sqrt{2\pi mkT}}{P_s} \right] \right)} \tag{27}$$

and

$$r^*_{twin} = \frac{\gamma}{\left(\dfrac{kT}{\Omega} \ln\left[\dfrac{J\sqrt{2\pi mkT}}{P_s} \right] - \dfrac{\gamma_t}{h} \right)} \tag{28}$$

where γ is the surface energy, k is the Boltzmann constant, T is the substrate temperature during deposition, Ω is the atomic volume, J is the deposition flux, and P_s is the vapor pressure above solid, γ_t and h is the twin boundary energy and the height of twin nuclei, respectively. In comparing eq. (27) with (28), we note that $r^{*}_{perfect} < r^{*}_{twin}$, and nucleation of a perfect nucleus will be preferred to a twinned nucleus. However, if γ_t is very low and J is very high, then the difference between $r^{*}_{perfect}$ and r^{*}_{twin} will be negligibly small, and the formation of twinned nuclei may occur with very high probability during growth. Our analysis has shown that the ration of nucleation rate between perfect and twinned nuclei can be expressed by:

$$\ln\frac{I_{perfect}}{I_{twin}} = -\frac{\Delta G^{*}_{perfect}}{kT} + \frac{\Delta G^{*}_{twin}}{kT} = \frac{\pi\gamma^{2}h\gamma_{t}}{kT\Delta G_{V}(h\Delta G_{V} - \gamma_{t})} \tag{29}$$

It follows that a higher deposition rate will lead to higher nucleation rate, and thus a higher twin density (smaller average twin spacing). This is consistent with our experimental observations on nt Cu that shows smaller average twin spacing at a higher deposition rate. It is worthwhile to point out that a similar study in sputtered 330 stainless steel films have shown that at higher deposition rate, the volume fraction of twinned grain increases continuously, whereas the average twin spacing remains approximately unchanged [47]. This is likely due to the fact that stainless steel has complicated chemistry, with Fe, Cr and Ni etc., and chemistry could play an important role in the formation of growth twins. Such aspect can not be captured by the thermodynamics model where only stacking fault energy and certain deposition parameters are considered.

V.4.3. Hardening from nanotwins

Comparisons of flow stress of nanotwinned Cu with polycrystalline Cu show that Hall-Petch pile up model is valid down to twin spacing of a few tens of nanometer and the linear characteristics quickly deviates thereafter. A similar Hall-Petch slope in nanotwinned and polycrystalline Cu indicates that the strengths of twin interface and grain boundaries are similar in blocking the transmission of dislocations. It has been shown previously by MD simulations that twin boundaries are important barriers to the transmission of single dislocations as dislocation interact with twin interface and a high shear stress or tensile stress is necessary to move the dislocation across twin interface on to {111} or {200} glide planes. MD simulation of nanotwinned Au nanopillar indicates strengthening could result from slip arrests in the form of Lomer-Cottrell locks at the intersection of partial dislocations and twin boundaries [137]. Such study together with a model based on the concept of twin boundary affected zone (TBAZ) predicts higher hardness at greater twin density in Au and Cu respectively [165]. Another independent study shows that relatively low coherent twin boundary shear strength can induce close-range attractive forces and cause slip to be absorbed into the twin plane.

Finally the observation of Frank partial (stacking fault) dislocation adjacent to twin boundaries may strengthen nanotwinned Cu even further as incoming dislocations would have to interact with the stacking fault, presumably adding more resistance to the transmission of single dislocations. Such aspects could be explored further by molecular dynamics simulations. Frank partials along twin interface are sessile dislocations, and thus could impede the propagation of twin boundaries in vertical direction during annealing. Our recent studies on nc nt Cu show that twin interfaces are much more stable

than grain boundaries, as twin boundary energy is much lower than that of grain boundary energy, and thus reduce the driving force to coarsen twins [135].

V.4.4. Electrical resistivity of epitaxial Cu films with nanoscale growth twins

The electrical resistivity of metals is influenced by defects in the crystals, such as grain boundaries, dislocations, stacking faults/twin boundaries. The reported values of resistivity coefficient of high angle grain boundaries in Cu range from 2.0 to 4.8×10^{-6} $\mu\Omega cm^2$ [173-175]. Literature data on the electrical resistivity coefficient of CTB is scarce. The resistivity coefficient of stacking fault in Cu has been estimated to be ~3.4 $\times 10^{-7}$ $\mu\Omega \bullet cm^2$ [173]) [174]. In epitaxial nanotwinned Cu films the predominant defects are two types of twin boundaries, $\Sigma 3$ (111) and (112). TEM studies show that grown-in threading dislocation density is rather low, and their contribution to total resistivity is comparable to that of fully annealed OFHC Cu.

We now attempt to estimate the resistivity coefficient of twins in epitaxial nt Cu films. According to the Mattiessen's rule, the resistivity of metals results from the scattering of conduction electrons by the imperfections and lattice vibrations (phonons) in the crystal. For simplicity we assume that the electrical resistivity of epitaxial nt Cu can be expressed by

$$\rho = \rho_T + \rho_D \tag{30}$$

where ρ_T is resistivity of OFHC Cu and is temperature dependent due to lattice vibrations. ρ_D is the contribution from growth defects, primarily {111} and {112} twin boundaries. The dependence of defect resistivity on temperature is typically considered negligible [11]. The contributions of impurities and dislocations are included in the

ρ_T term. Elastic modulus of the epitaxial nt Cu films is very close to that of bulk Cu, 120 GPa, indicating the sample is fully dense and hence porosity is not considered for estimation. For simplicity, we assume that the resistivity coefficient of {111} and {112} twin boundaries is the same. Thus ρ_D can be expressed by $A_{twin}\rho_{twin}$, where A_{twin} and ρ_{twin} represents the area and electrical resistivity of twin boundaries, respectively.

The values of ρ_{twin} is plotted vs. test temperature as shown in Figure 63a. The calculations were performed for results at three temperatures, 4, 70 and 293K, and yet the range of ρ_{twin} is clearly shown. The values of ρ_{twin} varies from 1 to 7×10^{-7} $\mu\Omega\bullet cm^2$, an
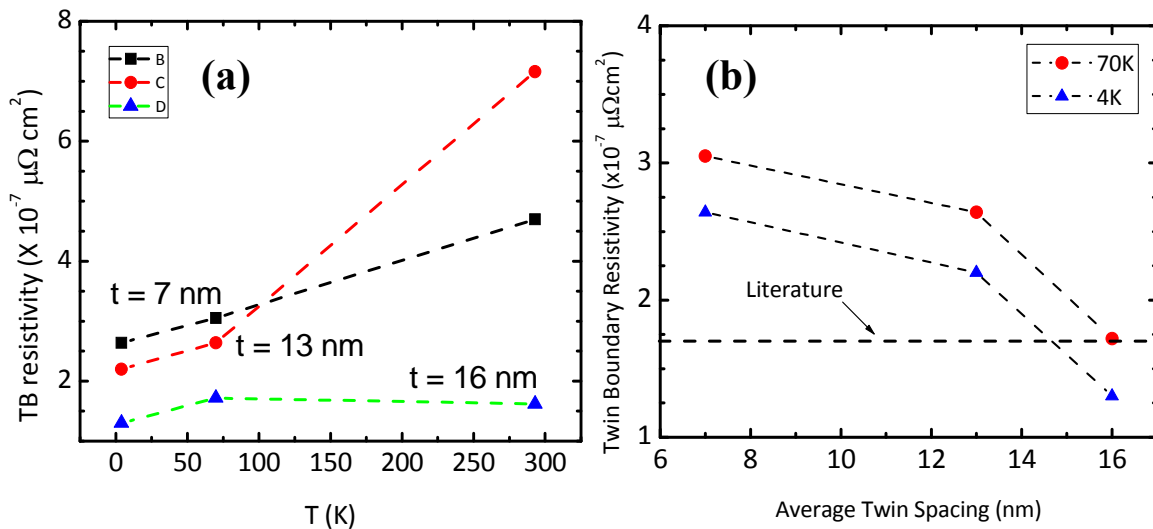
Fig. 63 (a) Twin boundary resistivity as a function of temperature at different average twin thicknesses shows variation. **(b)** Twin boundary resistivity as a function of average twin spacing [134].

order of magnitude lower than that of high angle grain boundaries, and is comparable to that of stacking fault. A clear temperature dependence of ρ_{twin} is observed. If a low

temperature dependence of resistivity of grain boundary and dislocations indicates a reduced coupling of defect atoms to crystal lattices, a temperature dependent ρ_{twin} would indicate the opposite occurs. Twin boundaries are low energy boundaries compared to that of grain boundaries, and hence such reduced lattice distortion would have less influence on the coupling of atoms along twin boundary to that of matrix, and hence reveal a stronger temperature dependent resistivity. Figure 63b shows a replot of calculated ρ_{twin} vs. the average twin spacing in epitaxial nt Cu. The reduction of ρ_{twin} with the average twin spacing seems bizarre as the characteristics (electrical resistivity) of twin interface should be independent of twin spacing. The reduction can only be interpreted as the enhanced coherency of twin interface with increasing average twin spacing. Indeed subtle changes are observed by examining the domain boundaries of epitaxial nt Cu. The lateral {111} twin boundaries are mostly coherent, whereas the characteristics of vertical {112} domain boundaries seem to be affected by deposition rate. At higher deposition rate, where the average twin spacing is 7 nm as shown in Figures 64 a-c, the {112} twin boundary has more defects. Figure 64c reveals a slight misorientation of {111} planes across domain boundaries. Such wandered {111} planes could pose more resistance to the transport of electrons across domain boundaries. On the other hand, at lower deposition rate, with an average twin spacing of 16 nm, the density of {111} offset planes are clearly much less, indicating an enhanced coherency across domain boundaries as shown in Figures 64 d-f. It is important to note that nc Cu with average grain size ~ 7 nm shows a room temperature resistivity of 14 μΩ•cm about an order of magnitude higher than that in the epitaxial nt Cu ($L_{avg}^{twin} = 7\,nm$) [176]. Significant scattering is observed in the case of nc Cu due to high angle grain boundaries,
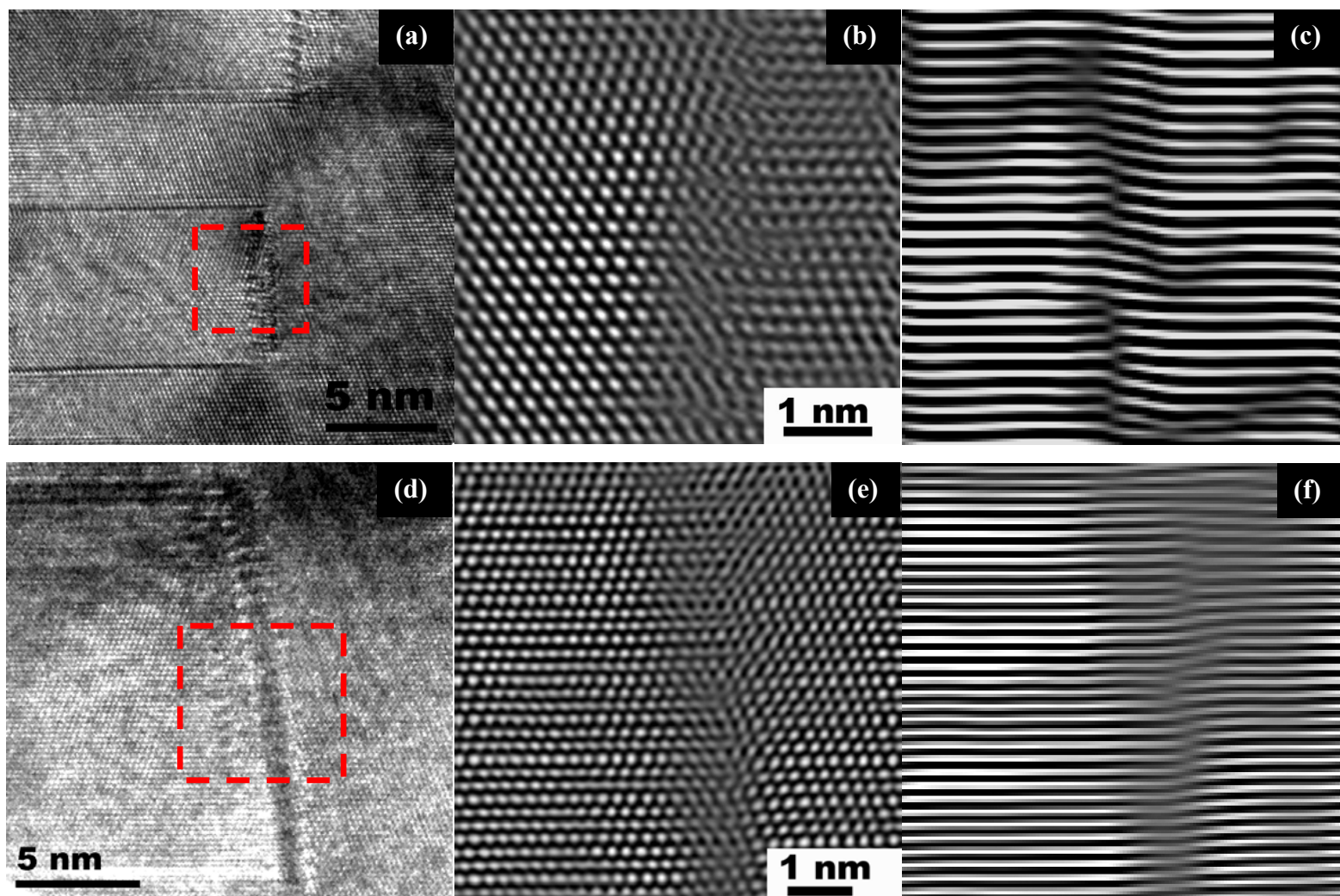
Fig. 64 (a-c) <112> TB is shown from a twin of ~7 nm size is from the 7 nm average twin thickness film. **(d-f)** <112> TB is shown from a twin of ~17 nm size from the 13 nm average twin thickness film [134].

Since CTBs are not significant scattering sources, resistivity of epitaxial nt Cu is still comparable to OFHC Cu resistivity.

V.4.5. Strength vs. conductivity of nt Cu

Figure 65a is a plot of hardness vs. conductivity for various Cu, including poly nt, epitaxial nt, electrodeposited nt, nc Cu and OFHC Cu. The strength of the epitaxial nt Cu films is discussed elsewhere [134]. The figure suggests that, in general, higher strength comes at the expense of lower conductivity. This is true for nc as well as poly nt Cu. For nc Cu, the conductivity is limited by high angle GBs. To enhance the conductivity of nc Cu, one must enlarge the grain size, which in turn decreases the strength. In nt Cu, as
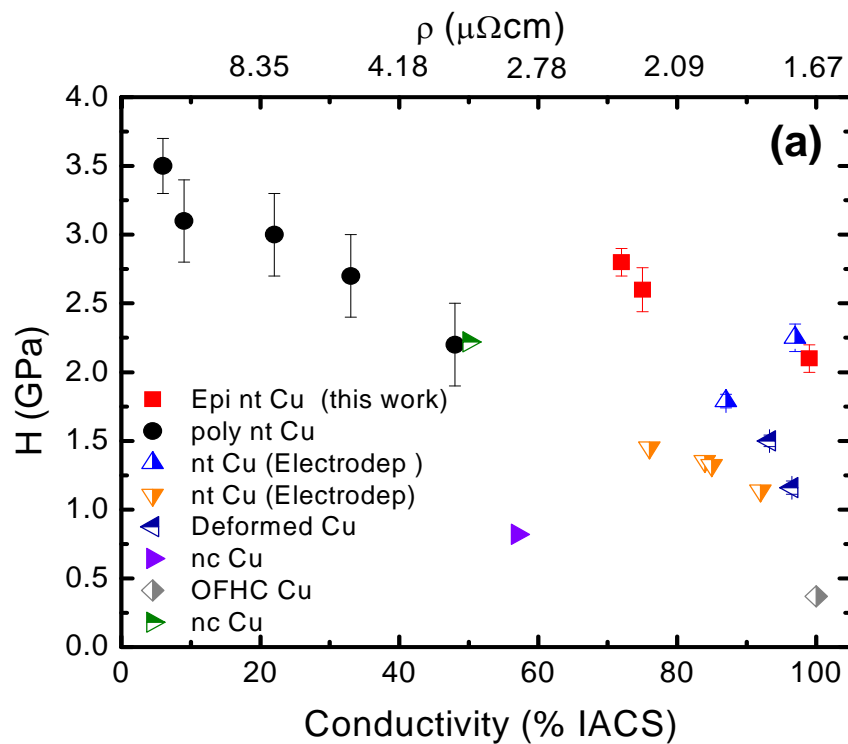
Fig. 65a Hardness as a function of conductivity plots. Literature data also included for comparison [134].

long as grain sizes are much greater than mean free path of Cu, a reasonably high electrical conductivity may be retained. However, the same trend applies, i.e. for similar grain sizes, smaller average twin spacing leads to high strength and lower conductivity.

The introduction of a high density of growth twins in single crystal like (epitaxial) Cu is a promising approach to push to the high strength and high conductivity limit. But the challenge is to increase the coherency of {112} twin boundaries or enlarge the domain size while keeping the twin spacing less than 10 nm. The {112} twin boundaries, oriented perpendicular to the growth direction (Figures 64a and d), form at the intersection of matrix in one island and twin in the adjacent island.

To elucidate the different characteristics of twin boundary and grain boundary in achieving high strength and high conductivity, we will attempt to estimate the influence of grain size or twin spacing on the ratio of flow strength to resistivity (at room temperature).

The flow strength (H-P relation is used) of polycrystalline (contains only grains, no twins) or single crystalline nt Cu (contains only twins, no grains) is estimated as follows:

$$\sigma = \sigma_0 + k.l_{grain/twin}^{-0.5} \tag{31}$$

where σ_0 is lattice friction, k is a constant and l is the thickness of twin lamellae along the {111} glide plane or grain diameter in the case of polycrystalline metals with no twins. For resistivity, we apply

$$\rho = \rho_0 + d_{grain/twin} \cdot \rho_{grain/twin} \tag{32}$$

where ρ_0 is the intrinsic resistivity, d is the density of grains or twins and $\rho_{grain/twin}$ is the scattering coefficient of GB or CTB.

Based on these equations, the ratio is given as,

$$\frac{\sigma}{\rho} = \frac{\sigma_0 + k.l_{grain/twin}^{-0.5}}{\rho_0 + d_{grain/twin} \cdot \rho_{grain/twin}} \tag{33}$$
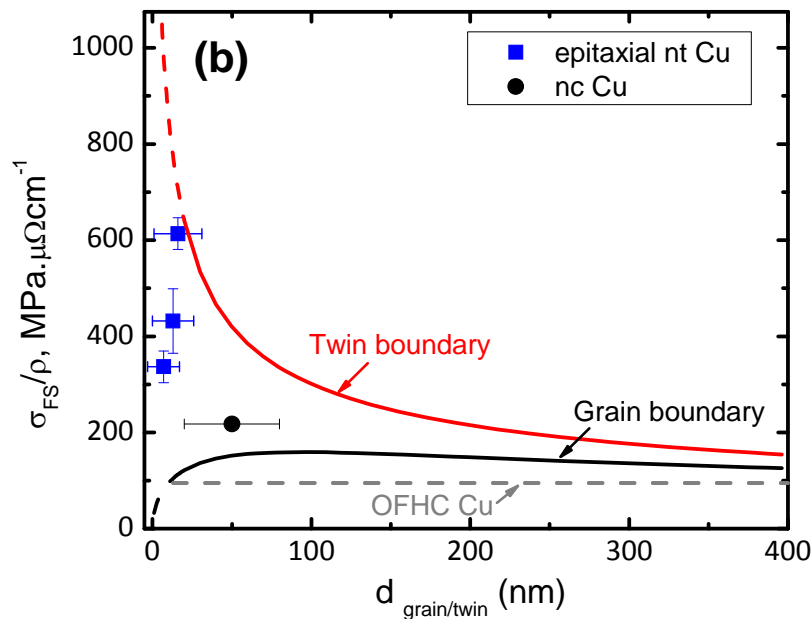
Fig. 65b Ratio of flow strength to resistivity as a function of grain size. Solid lines are calculated values. Blue and red dashed lines indicate the region where Hall-Petch model is no longer valid.

Figure 65b shows the plot of σ/ρ vs. grain size or twin spacing. The solid lines are constructed so that the increase in strength and resistivity is due to only twins or grains respectively. The plot also predicts what is achievable in theory when the strength can still be estimated by the H-P relation. The plot shows the size dependence of σ/ρ on twin boundary and grain boundary is very different; i.e. a smaller twin spacing can effectively increase σ/ρ, whereas reduced grain size will decrease σ/ρ when grain size is less than

mean the free path of Cu. Figure 65b also shows the experimental data from epitaxial nt Cu, electrodeposited nt Cu, nc Cu without twins and OFHC Cu [134, 171, 177-179]. Note that at smaller twin sizes, epitaxial nt Cu films show deviation from the model. This is because the twin spacing is small enough that the prediction based on H-P strength is not valid, and also because a non-negligible fraction of twin boundaries in epitaxial nt Cu films are incoherent (112) twin boundaries that has reduced the overall conductivity, but are not accounted for in the model. Nevertheless at all twin sizes, epitaxial nt Cu films show better σ/ρ ratios than that of nc Cu and OFHC Cu. Such analysis indicates that nanotwins could offer a more effective approach in enhancing the strength-to-resistivity ration in high strength conductors in general.

V.4.6. Superlattice in epitaxial nanotwinned Cu

An intriguing feature of these epitaxial nt Cu films is that a large number of these twins are continuous across domain boundaries. Domain boundaries where twins and matrices meet are typically vertical steps throughout the films. HRTEM are performed to investigate a large number of these step-like domain boundaries, and a typical example is shown in Figure 66. Given the volume fraction of twin and matrix is similar, the label of twin (T) and matrix (M) in Figure 66a is arbitrary. A square box at the domain boundary is magnified, and details are shown in Figure 66b. To clarify atomic arrangement, atomic planes are labeled as A, B and C in twin and matrix along domain boundary. Such study reveals that among every three atomic plane, there is a common atomic plane B extending continuously across domain boundary. Presumably strain is likely to be lower along this atomic plane (B), and higher in neighboring atomic planes (A and C). The

strain contrast along domain boundary is clearly observed in a periodic way (every three atomic plane). A rectangular box in Figure 66b indicates this new superlattice structure. Fast Fourier transform (FFT) of the image in 66b confirms that there is a set of superlattice diffraction spot as shown in Figure 66c. SAD pattern of specimens from a larger area clearly demonstrates the superlattice structure coexisting with typical twin pattern in these epitaxial Cu films, as provided in Figure 66d. This type of superlattice structure was not observed in the authors' nc nt Cu films, as shown in Figure 66e, because {111} type planes in adjacent grains are tilted either out-of-plane or in-plane. Such superlattice type structure is thus a result of the successful synthesis of epitaxial Cu films with nanotwins. Other unique feature observed includes stacking fault (Frank partial dislocation) adjacent to twin interfaces, as shown in Figure 67. Again superlattice structure (indicated by B-B) is observed along domain boundary. The vertical domain boundary observed in epitaxial nt Cu is a result of island growth mechanisms typically observed during sputtering. Domain boundary could potentially be eliminated if a two-dimensional growth mechanism operates (during molecular beam epitaxial growth). Domain boundaries demarcate two perfectly aligned single crystals, twin and matrix. Such alignment however cause constrains along vertical domain boundaries, and lead to the observation of superlattice structure: one out of every three {111} atomic planes is continuous across domain boundaries. Thus the formation of superlattice structure is likely to be a result of strain relief along domain boundary.
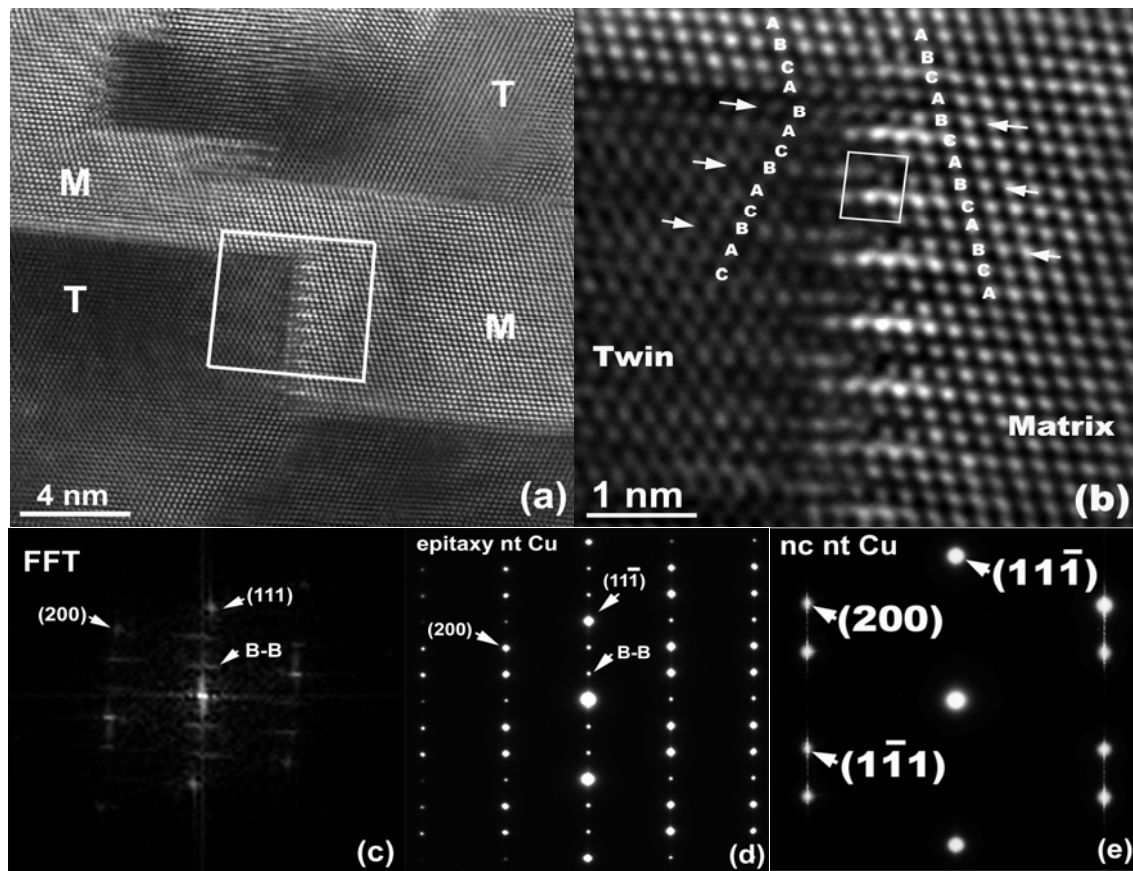
Fig. 66 (a) XTEM of domain boundaries of epitaxial Cu film deposited at 40 Å /sec. Matrix and twins are mutually continuous across domain boundary. **(b)** Magnified box of vertical segment of grain boundaries in **a**. ABC stacking is highlighted in both twin and matrix. Every 3 atomic plane there is a common atomic plane, A, extending continuously across grain boundary, indicating single crystal type twin-matrix correlation. Such periodic structure, indicated by a box in **b**, is reflected by extra diffraction dots, B-B, as shown in **c**, the fast Fourier transform (FFT), and **d,** the selected area diffraction pattern of a much larger area. **(e)** In comparison, typical SAD pattern of twins in nanocrystalline, nanotwinned Cu is also shown.
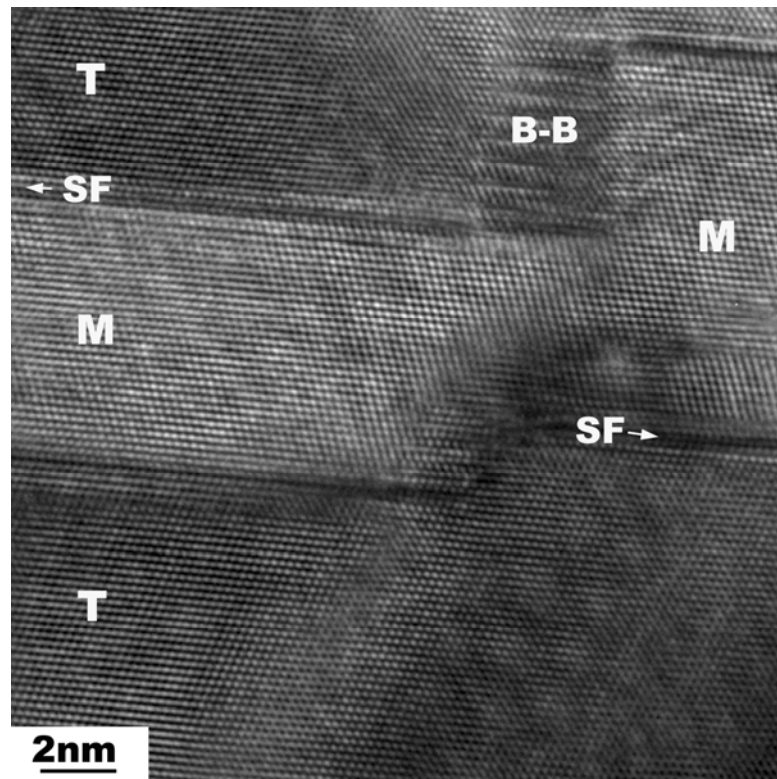
Fig. 67 HRTEM micrograph of twinned domains for Cu films deposited at 40Å/sec shows stacking fault (Frank partial dislocations), at twin boundaries. Again B-B stacking across domain boundary is seen, and twins or matrix are continuous in a zig-zag pattern across domain boundary.

Detailed molecular dynamics simulations are helpful in validating this hypothesis. A recent study based on first principle calculations predicts that highly strained Cu could undergo recrystallization and grain growth to relax stress and form strain–relieved nanotwins [38].

V.5. Summary

We have fabricated epitaxial Cu films with a high density of nanoscale growth twins. The twin spacing can be tailored by changing deposition rates, consistent with the

prediction of a thermodynamics model. The films show an order of magnitude higher hardness than bulk Cu with electrical resistivities comparable to that of OFHC Cu. The resistivity of twin boundaries is calculated to be an order of magnitude lower than that of high angle grain boundaries. Material design using twin boundaries has clear advantages in achieving a better combination of high strength and high electrical conductivity over high angle grain boundaries.

CHAPTER VI

SUMMARY

The goal of this thesis was to produce high strength high conductivity copper films and study thermal stability and deformability. Two kinds of nanotwinned copper films were produced: polycrystalline and epitaxial. Polycrystalline and epitaxial nanotwinned copper films were sputtered on Si substrate with a native oxide layer and HF etched Si (110) substrates respectively.

Polycrystalline nanotwinned copper films were annealed at high vacuum and temperature to study the thermal stability of twins and to eliminate grain boundaries. As a result of annealing at 200, 400, 600 and 800 °C, twins show insignificant growth from ~4 nm to < 20 nm, whereas grains grow from ~50 nm up to half micron size. This was attributed to low energy stored in twins compared to grains. The grain growth significantly improves the resistivity, while hardness of the film show slight decrease due to twin coarsening but still an order of magnitude higher than that of bulk copper. The study successfully showed that contrary to most nanocrystalline metals, nanotwins show remarkable thermal stability at elevated temperatures and that annealing could be a method to produce high strength copper with reasonable conductivity.

Epitaxial nanotwinned copper films were sputtered as a second method of high strength high conductivity copper production. The other purpose of this study was to vary average twin spacing by adjusting deposition parameters. Epitaxial nanotwinned copper films with hardness reaching 2.8 GPa and resistivity comparable to oxygen free

high conductivity copper were successfully produced. Growth of copper with nanotwins which strengthen copper by blocking discloation motion and without grain boundaries which are significant electron scattering sources resulted in a high strength high conductivity copper. An analytical model was developed to estimate strength-to-resistivity ratio. The analyses indicated that the strength-to-resistivity ratio can be enhanced by grain refinement or introduction of nanotwins. However, the advantage of grain refinement quickly vanishes when the average grain size is comparable to the mean-free path of electrons due to significant scattering of electrons at the grain boundaries. On the other hand, coherent twin interfaces possess an order of magnitude lower electron scattering coefficient than grain boundaries, and can increase the strength-to-resistivity ratio further to a much greater value by reducing the average twin spacing. Electrical resistivity coefficient of coherent twin interface was determined to be $1.5–5\times10^{-7}\mu\Omega$ cm^2 in Cu, an order of magnitude lower than that of high-angle grain boundaries. Our analytical studies together with experimental evidence show that nanotwins can significantly improve the strength-to-resistivity ratio in Cu, and the study could have important implications in designing high strength conductors.

Deformation mechanisms of polycrystalline nanotwinned copper films were studied by room temperature rolling. Although high strength usually comes with reduced ductility, polycrystalline nanotwinned copper exhibited stable plastic flow with no shear localization or fracture even at 69% true strain. X-ray pole figure measurements were performed before and after deformation to study the texture. Insignificant out-of-plane texture was observed which was attributed to symmetric slip. Average grain size triples

but average twin thickness almost stayed constant after rolling due to annihilation of thin twins (< 3nm). A high density of dislocations was observed at twin interface (2.4×10^{16} cm^{-2}). The observed work hardening after rolling is interpreted in terms of stored dislocations at interfaces.

REFERENCES

1- M. Stanczak, M. *A Brief History of Copper*. Available from: http://www.csa.com/discoveryguides/copper/overview.php, accessed 2/12/2009.

2- R.B. Gordon, M. Bertram, and T.E. Graedel, Proc. Natl. Acad. Sci. **103**, 1209 (2006).

3- W. H. Dresher, *Copper and Nanotechnology*. Available from: http://www.copper.org/publications/newsletters/innovations/2006/01/copper_nanotechnology.html, accessed 2/12/2009.

4- K. Seshan, *Handbook of Thin-film Deposition Processes and Techniques* (Noyes Publications/William Andrew, Norwich, NY 2002)

5- M. Ohring, *Materials Science of Thin Films* (Academic Press, San Diego, CA 2002)

6- L.B. Freund and S. Suresh, *Thin Film Materials* (Cambridge University Press, Cambridge, UK 2003).

7- Y. Xiang, PhD Thesis, Harvard University, 2005.

8- R. Rosenberg, D. C. Edelstein, C. K. Hu, and K. P. Rodbell, Annu. Rev. Mater. Sci. **30**, 229 (2000).

9- J. A. Venables, G. D. T. Spiller, and M. Hanbucken, Rep. Prog. Phys. **47**, 399 (1984).

10- C. V. Thompson, Annu. Rev. Mater. Sci. **30**, 159 (2000).

11- M. Meyers and K. Chawla, *Mechanical Behavior of Materials* (Cambridge Uni. Press, Cambridge, UK 1998).

12- D. P. Tracy and D. B. Knorr, J. of Elect. Mater. **22**, 611 (1993).

13- D. B. Knorr and D. P. Tracy, Mater. Chem. and Phys. **41**, 206 (1995)

14- X. Huang, Q.H. Lu, M.L. Sui, D.X. Li and N. Hansen, Mater. Sci. Forum, **539**, 5013 (2007).

15- X. Zhang, H. Wang, X.H. Chen, L. Lu, K. Lu, R.G. Hoagland and A. Misra, App. Phys. Lett. **88**, 173116 (2006)

16- G.W. Zhou, Acta Mat. **57**, 4432 (2009).

17- *ASM Handbooks Online*. Available from: http://products.asminternational.org/hbk/index.jsp, accessed 12/01/2009.

18- J.M.Purswani, T.Spila, and D. Gall, Thin Solid Films, **515**, 1166 (2006).

19- L.O. Brockway and R. B. Marcus, J. Appl. Phys. **34**, 921 (1961).

20- J. W. Matthews and J. L. Crawford, Thin Solid Films, **5**, 187 (1970).

21- C.S. Liu, S.R. Chen, W.J. Chen and L.J. Chen, Mater. Chem. Phys. **36**, 170 (1993)

22- H.Jiang, T.J Klemmer, J.A. Barnard, W.D Doyle and E.A Payzant, Thin Solid Films, **315**, 13 (1997).

23- K. S. Kumar, H. Van Swygenhoven, and S. Suresh, Acta Mater. **51**, 5743 (2003).

24- I. Karaman, M. Haouaoui, and H. J. Maier, J. Mater. Sci. **42**, 1561 (2006).

25- Y. Wang, M. Chen, F. Zhou, and E. Ma, Nature, **419**, 912 (2002).

26- W. D. Callister, *Materials Science and Engineering*, 4th ed. (John Wiley & Sons, New York 1997).

27- J. Chen, L. Lu, and K. Lu, Scr. Mater. **54**, 1913 (2006).

28- J. Schiotz and K. W. Jacobsen, Science **301**, 1357 (2003).

29- J. Schiøtz, F. D. Di Tolla, and K. W. Jacobsen, Nature **391**, 561 (1998).

30- P. G. Sanders, J. A. Eastman, and J. R. Weertman, Acta Mater. **45**, 4019 (1997).

31- H. Gleiter, Prog Mater. Sci. **33**, 223 (1989).

32- S. Suresh, T. G. Nieh, and B. W. Choi, Scrip. Mater. **41**, 951 (1999).

33- T.H. Fang and W.J. Chang, Microelec. Eng. **65**, 231 (2003).

34- R. P. Vinci and J. J. Vlassak, Annu. Rev. Mater. Sci. **26**, 431 (1996).

35- H.B. Huang and F. Spaepen, Acta Mater. **48**, 12 (2000).

36- D. T. Read, Int. J Fatigue, **20**, 203 (1998).

37- D.T. Read, Y.W. Cheng, and R. Geiss, Microelec. Eng. **75**, 63 (2004).

38- R. R. Keller, J. M. Phelps, and D. T. Read, Mater. Sci. Eng. A **214**, 42 (1996).

39- W.D. Nix. Metall. Trans. A **20**, 2217 (1989).

40- R. Keller, S.P. Baker and E. Arzt. J.Mater. Res. **13**, 1307 (1998).

41- R. Spolenak, C.A. Volkert, K. Takahashi, S. Fiorillo, J. Miner and W.L. Brown. Mater. Res. Soc. Symp.Proc. **594**, 63 (2000).

42- D.Y.W. Yu and F. Spaepen. J.Appl. Phys. **95**, 2991 (2004).

43- Y. Xiang, T. Y. Tsui, and J. J. Vlassak, J. Mater. Res. **21**, 1607, (2006).

44- L. Fuchs, Proc. Cambridge Phil. Soc. **34**, 100 (1938).

45- E.H. Sondheimer, Adv. Phys. **1**, 1 (1952).

46- S. M. Rossnagel and T. S. Kuan. J. Vac. Sci. Tech. B **22**, 240 (2004).

47- F. Mayadas and M. Shatzkes, Phys. Rev. B **1**, 1382 (1970).

48- Y. Ke, F. Zahid, V. Timoshevskii, K. Xia, D. Gall, and H. Guo, Phys. Rev. B **79**, 155406 (2009).

49- O. Anderoglu, A. Misra, F. Ronning, H. Wang, and X. Zhang, J. Appl. Phys. **106**, 024313 (2009).

50- R.W. Cahn, Proc. Phys. Soc. A **63**, 323 (1950).

51- J. A. Venables, J. Phys. Chem. Sol. **25**, 685 (1963).

52- R.W. Cahn and P. Haansen, *Physical Metallurgy*, Volume I (Elsevier, Amsterdam, Netherlands 1996).

53- A. Liversidge, R. Soc. N.S.W.J. Proc. **27,** 303 (1893).

54- R. L. Fullman and J .C. Fisher, J. Appl. Phys. **22**, 1350 (1951).

55- H. Gleiter, Acta Metall. **17**, 1421 (1969).

56- S. Dash and N. Brown, Acta Metall. **11**, 1067 (1963).

57- M. A. Meyers and L. E. Murr, Acta Metall. **26**, 951 (1978).

58- B. B. Rath, M. A. Imam, and C. S. Pande, Mater. Phys. Mech.**1**, 61 (2000).

59- D. E. Farkas, E. Bringa, and A. Caro, Phys. Rev. B, **75** 184111 (2007).

60- H. Hu and C.S. Smith, Acta Metall. **4**, 638 (1956).

61- S. Mahajan, Acta Mater. **45**, 2633 (1997).

62- R. Viswanathanand and C. Bauer, Metall. Mater. Trans. B, **4**, 2645 (1973).

63- Available from: http://www.msm.cam.ac.uk/phase-trans/images, accessed 2/2/2009

64- J. W. Christian and S. Mahajan, Prog. Mater. Sci. **39**, 1 (1995).

65- M. Chen, E. Ma, K. J. Hemker, H. Sheng, Y. Wang, and X. Cheng, Science, **300**, 1275 (2003).

66- V. Yamakov, D. Wolf, S. R. Phillpot, A. K. Mukherjee, and H. Gleiter, Nat. Mater. **1**, 45 (2002).

67- X. Zhang, A. Misra, H. Wang, T. D. Shen, M. Nastasi, J. D. Embury, T. E. Mitchell, R. G. Hoagland, and J. P. Hirth, Appl. Phys. Lett. **84**, 1096 (2004).

68- L. Xu, P. Dixit, J. Miao, and J. L. Pang, Appl. Phys. Lett. **90**, 033111 (2007).

69- L. Lu, Y. Shen, X. Chen, L. Qian, and K. Lu. Science, **304**, 422 (2004).

70- B. Cui, K. Han, Y. Xin, D. Waryoba, and A. Mbaruku, Acta Mater. **55**, 4429 (2007).

71- B. Wu, C. Schuh, and P. Ferreira, Metall. Mater. Trans. A, **36**, 1927 (2005).

72- G. Lucadamo, D. L. Medlin, N. Y. C. Yang, J. J. Kelly, and A. A. Talin. Phil. Mag. **85**, 2560 (2005).

73- A. M. Hodge, Y.M. Wang, and J.T.W. Barbee, Mater. Sci. Eng. A, **429**, 272 (2006).

74- X. Zhang, A. Misra, H. Wang, M. Nastasi, J. D. Embury, T. E. Mitchell, R. G. Hoagland, and J. P. Hirth, Acta Mater. **52**, 995 (2004).

75- X. W. Zhou and H.N.G. Wadley, Acta Mater. **47**, 1063 (1999).

76- D. Xu, K. W. Lek, C. Kai, X. Zhang, and K. N. Tu, Appl. Phys. Lett. **91**, 254105 (2007).

77- Available from: http://www.angstromsciences.com/technology/angstrom-advantage/index.html, accessed 2/14/2009

78- L. J. van der Pauw, Philips Res. Rep. **13**, 1 (1958).

79- S. P. Baker and N. Burnham, *Measuring Mechanical Properties in the Nanometer Regime*, 2000 MRS Fall Meeting Tutorial Program, Boston, MA.

80- Available from: http://www.xray.cz/xray/csca/kol2005/abst/ctvrtlik_files/image008.gif, accessed 2/14/2009.

81- ASTM E 18, E10, E 92 and E 384, Standard test method for Rockwell hardness, Brinell hardness, Vickers hardness and Microhardness of Metallic Materials.

82- ISO 14577: 2002, Metallic Materials-Instrumented indentation test for hardness and materials parameters.

83- S.I. Bulychev, V.P. Alekhin, Zavodskaya Laboratoriya, **53**, 76 (1987).

84- M.F. Doerner and W.D. Nix, J. Mater. Res. **1**, 601 (1986).

85- W.C. Oliver and G.M. Pharr, J. Mater. Res. **7**, 1564 (1992).

86- J.B. Pethica and W.C. Oliver, Physica Scripta T **19**, 61 (1987).

87- T.J. Bell and M.V. Swain, Thin Solid Films, **220**, 289 (1992).

88- J.S. Field and M.V Swain, J Mater Res, **8**, 297 (1993).

89- Available from: http://www.azonano.com/details.asp?ArticleID=1994, accessed 2/14/2009.

90- G. Shafirstein, MRS Symp. Proc. **356**, 717 (1995).

91- S.P. Baker, T.W. Barbee Jr, and W. D. Nix, MRS Symp. Proc. **239**, 319 (1992).

92- W.D. Nix and H. Gao, J Mech. Phys. Solids, **46**, 411 (1998).

93- Y. Huang, Z. Xue, H. Gao, W.D. Nix, and Z.C. Xia, J Mater Res, **15**, 1786 (2000).

94- N. Panich and Y. Sun, Surf. Coat. Tech. **182**, 34 (2004).

95- G.W. Nieman, J.R. Weertman, and R.W. Siegel, J. Mater. Res. **6**, 1012 (1991).

96- L. Lu, L.B. Wang, B.Z. Ding, and K. Lu. Mater. Sci. Eng. A **286**, 125 (2000).

97- J.R. Weertman, D Farkas, K. Hemker, H. Kung, M. Mayo, R. Mitra, and H. Van Swygenhoven, MRS Bull. **24**, 4 (1999).

98- X. Zhang, A. Misra, H. Wang, T.D. Shen, J.G. Swadener, J.D. Embury, H. Kung, R.G. Hoagland, and M. Nastasi, J. Mater. Res. **18**, 1600 (2003).

99- A. Misra, M. Verdier, Y. C. Lu, H. Kung, T. E. Mitchell, M. Nastasi, and J. D. Embury. Scrip. Mater. **39**, 555 (1998).

100- B.M. Clemens, H. Kung, and S.A. Barnett. MRS Bull. **24**, 20 (1999).

101- A. Misra, J.P. Hirth, and R.G. Hoagland, Acta Mat. **53**, 4817 (2005).

102- L. Lu, Y. Shen, X. Chen, L. Qian, and K. Lu, Science **304**, 422 (2004).

103- Y.F. Shen, L. Lu, Q.H. Lu, Z.H. Jin, and K. Lu, Scrip. Mat **52**, 989 (2005).

104- W.J. Babyak and F.N. Rhines, Metall. Petr. Eng. Trans. **218**, 21 (1960).

105- X. Zhang, A. Misra, H. Wang, A. L. Lima, M. F. Hundley, and R. G. Hoagland, J. Appl. Phys. **97**, 094302 (2005).

106- X. Zhang, O. Anderoglu, A. Misra and H. Wang, Appl. Phys. Lett. **90**, 153101 (2007).

107- V. Y. Gertsman and R. Birringer, Scrip. Metall. **30**, 577 (1994).

108- M. Kobiyama, T. Inami and S. Okuda, Scrip. Mat. **44**, 1547 (2001).

109- C. F. Gu, F. Dalla Torre, J. Sandlin, E. V. Pereloma, and C. H. J. Davies. Mater. Forum, **29**, 551 (2005).

110- K. Oh-ishi, Z. Horita, D. J. Smith, R. Z. Valiev, M. Nemoto, and T. G. Langdon, J. Mat. Res. **14**, 4200 (1999).

111- R. K. Islamgaliev, F. Chmelik, and R. Kuzel, Mat. Sci. Eng. A**234**, 335 (1997).

112- O. Anderoglu, A. Misra, H. Wang, and X. Zhang, J. Appl. Phys. **103**, 094322 (2008).

113- S. Okuda, M. Kobiyama, T. Inami, and S. Takamura, Scrip. Mat. **44**, 2009 (2001).

114- X. Zhang, A. Misra, H. Wang, A. L. Lima, M. F. Hundley, and R. G. Hoagland, Appl. Phys. Lett. **87**, 233116 (2005).

115- N. Hansen and B. Ralph, Acta Metall. **30**, 441 (1982).

116- H. Jiang, T. Zhu, D. P. Butt, I. V. Alexsandrov, and T. C. Lowe, Mater. Sci. Eng. A**290**, 128 (2000).

117- I. M. Ghauri, M. Z. Butt, and S. M. Raza, J. Mater. Sci. **25**, 4782 (1990).

118- L. Lu, N. R. Tao, L. B. Wang, B. Z. Ding, and K. Lu. J. Appl. Phys. **89**, 6408 (2000).

119- S. K. Ganapathi, D. M. Owen, and A. H. Chokshi, Scrip. Metall. **25**, 2699 (1991).

120- H. V. Atkinson, Acta Metall. **36**, 469 (1998).

121- C. V. Thomson, Annu. Rev. Mater. Sci. **20**, 245 (1990).

122- K. Barmak, A. Gungor, A.D. Rollett, C. Cabral Jr., and J. M. E. Harper, Mat. Sci. Sem. Cond. Proc. **6**, 175 (2003).

123- L. A. Zepeda-Ruiz, G. H. Gilmer, B. Sadigh, A. Caro, T. Oppelstrup, and A. V. Hamza, Appl. Phys. Lett. **87**, 231904 (2005).

124- R. W. Cahn and P. Haasen, *Physical Metallurgy,* Volume III (Elsevier, Amsterdam, Netherlands 1996).

125- Y. K. Huang, A. A. Menovsky, and F. R. de Boer. Nanostruc. Mat. **2**, 587 (1993).

126- L. E. Murr, *Interfacial Phenomena in Metals and Alloys* (Addison-Wesley, Reading, MA 1975).

127- J.P. Hirth and J. Lothe. *Theory of Dislocations*. 2nd ed. (Krieger, Melbourne 1992).

128- T.G. Nieh and J. Wadsworth, Scrip. Metall. **25**, 955 (1991).

129- S.I. Rao and P.M. Hazzledine, Phil. Mag. A**80**, 2011 (2000).

130- A. Misra, J.P. Hirth, and H. Kung, Phil. Mag. A**82**, 2935 (2002).

131- R. G. Hoagland, T.E. Mitchell, J. P. Hirth, and H. Kung. Phil. Mag. A**82**, 643 (2002).

132- J. Wang and H. Huang, Appl. Phys. Lett. **88**, 203112 (2006).

133- T. Zhu, J. Li, A. Samanta, H.G. Kim, and S. Suresh, PNAS, **104**, 3031 (2007).

134- L. Lu, R. Schwaiger, Z.W. Shan, M. Dao, K. Lu and S. Suresh, Acta Mater. **53**, 2169 (2005).

135- O. Anderoglu, A. Misra, H. Wang, F. Ronning, M. F. Hundley and X. Zhang, Appl. Phys. Lett. **93**, 083108 (2008).

136- M. D. Merz and S. D. Dahlgren, J. Appl. Phys. **46**, 3235 (1975).

137- K. A. Afanasyev and F. Sansoz, Nano Lett. **7**, 2056 (2007).

138- A. J. Cao, Y. G. Wei, and S. X. Mao, Appl. Phys. Lett. **90**, 151909 (2007).

139- A. G. Froseth, P. M. Derlet, and H. Van Swygenhoven, Appl. Phys. Lett. **85** 5863 (2004).

140- A. G. Froseth, P. M. Derlet, and H. Van Swygenhoven, Acta Mater. **52**, 5863 (2004).

141- J. Wang and H. Huang, Appl. Phys. Lett. **88**, 203112 (2006).

142- Z. H. Jin, P. Gumbsch, E. Ma, K. Albe, K. Lu, H. Hahn, and H. Gleiter, Scrip. Mater. **54**, 1163 (2006).

143- Z. H. Jin, P. Gumbsch, K. Albe, E. Ma, K. Lu, H. Gleiter, and H. Hahn, Acta Mater. **56**, 1126 (2008).

144- A. J. Cao and Y. G. Wei, J. Appl. Phys. **102**, 083511 (2007).

145- Y. G. Zheng, Scrip. Mater. **60**, 508 (2009).

146- A. Jerusalem, M. Dao, S. Suresh and R. Radovitzky, Acta Mater. **56**, 4647 (2008).

147- J. E. Flinn, D. P. Field, G. E. Korth, T. M. Lillo, and J. Macheret, Acta Mater. **49**, 2065 (2001).

148- D. P. Field, B. W. True, T. M. Lillo, and J. E. Flinn, Mater. Sci. Eng. A **372**, 173 (2004).

149- L. Lu, R. Schwaiger, Z. W. Shan, M. Dao, K. Lu, and S. Suresh, Acta Mater. **53**, 2169 (2005).

150- Y. B. Wang, M. L. Sui, and E. Ma, Phil. Mag. Lett. **87**, 935 (2007).

151- Y. B. Wang, B. Wu, and M. L. Sui, Appl. Phys. Lett. **93**, 041906 (2008).

152- J. P. Hirth and R.W. Balluffi, Acta Metall. **21**, 929 (1973).

153- A. Misra, J. P. Hirth, and R. G. Hoagland, Acta Mater. **53**, 221 (2005).

154- H. Paul, J. H. Driver, C. Maurice, and Z. Jasienski, Mater. Sci. Eng. A**359**, 1 (2003).

155- K. Sekine and J. Wang, Mater. Trans. **40**, 1 (1999).

156- X. Huang, Q. H. Lu, M. L. Sui, X. D. Li, and N. Hansen, Mater. Sci. Forum, **539**, 5013 (2007).

157- D. Mitlin, A. Misra, T. E. Mitchell, R. G. Hoagland, and J. P. Hirth, Appl. Phys. Lett. **85**, 1686 (2004).

158- H. Kimura, A. Inoue, N. Muramatsu, K. Shin, and T. Yamamoto, Mat. Trans. **47**, 1595 (2006).

159- Y. Sakai and H. J. Schneider-Muntau, Acta Mat. **45**, 1017 (1997).

160- D. P. Lu, J. Wang, W. J. Zheng, Y. Liu, L. Lu, and B. D. Sun, Mater Sci. Eng A, **421**, 254 (2006).

161- V.I. Pantsyrny, A.K. Shikov, V.E. Vorobieva, N.E. Khlebova, N. I.Kozlenkova, V. A. Drobishev, I. I. Potapenko, N. A. Beliakov, and M. V. Polikarpova, IEEE Trans. Appl. Supercond. **18**, 616 (2008).

162- J. A. Juarez-Islas, R. Perez, L. A. Albarran, V. Rivera, and L. Martinez, J. Mater. Sci. Lett. **11**, 1104 (1992).

163- K. R. Anderson and J. R. Groza, Metall. Metals Trans. A, **32**, 1211 (2001).

164- M. Murayama, A. Belyakov, T. Hara, Y. Sakai, K. Tsuzaki, and T. Kimura, J. Electr. Mater. **35**, 1787 (2006).

165- M. Dao, L. Lu, Y.F. Shen, and S. Suresh, Acta Mater. **54**, 5421 (2006).

166- L. Lu, X. Chen, X. Huang, and K. Lu, Science, **323**, 607, (2009).

167- S.D. Dahlgren, W.L. Nickholson, M.D. Merz, W. Bollmann, J.F. Devlin, and R. Wang, Thin Solid Films, **40**, 345 (1977).

168- O. Anderoglu, A. Misra, M. F. Hundley, and X. Zhang, unpublished (2006).

169- C. E. Schuster, M. G. Vangel, and H. A. Schafft, Microelect. Reliab. **41**, 239 (2001).

170- P. K. Moussouros and J. F. Kos, Can. J. Phys. **55**, 2071 (1977).

171- X. H. Chen, L. Lu, and, K. Lu, J. Appl. Phys. **102,** 083708 (2007).

172- X. W. Zhou and H. N. G. Wadley, Acta Mater. **47**, 1063 (1999).

173- P. V. Andrews, Phys. Lett. **19**, 558 (1965).

174- L. H. Qian, Q. H. Lu, W. J. Kong, and K. Lu, Scrip. Mater. **50**, 1407 (2004).

175- H. Yoshinaga, Phys. Status Solidi **18**, 625 (1966).

176- Y. K. Huang, A. A. Menovsky, and F. R. de Boer. Nanostructured Mater. **2**, 505 (1993).

177- S. Cheng, E. Ma, Y.M. Wang, L.J. Kecskes, K.M. Youssef, C.C. Koch, U.P. Trociewitz, and K. Han, Acta Mat. **53**, 1521 (2005).

178- E.A. Brandes and G. B. Brook, *Smithells Metals Reference Book*, 5th edition, (Butterworth-Heinemann, Oxford, UK 1976).

179- J. M. E. Harper, J. C. Cabral, P. C. Andricacos, L. Gignac, I. C. Noyan, K.P. Rodbell, and C. K. Hu. J. Appl. Phys. **86**, 2516 (1999).

VITA

Osman Anderoglu received his Bachelor of Science degree in mechanical engineering from Bogazici University, Istanbul, Turkey in 2001. He received his Master of Science degree in mechanical engineering in 2004 from Texas A&M University in College Station. In August 2005, he started the Ph.D. program in Materials Science and Engineering at Texas A&M University. He received his Ph.D. degree in May 2010.

During his doctoral studies, he held positions as research assistant and teaching assistant. He also worked as a graduate research assistant at Los Alamos National Laboratory during his internship. His research interests are in growth, microstructure, mechanical and electrical properties of thin films and nanostructured materials for extreme environments.

Permanent address:

Cinar Mh.

10/1 Sk. No: 17/2

Bagcilar/Istanbul 34200

TURKEY